Addis Ababa University

College of Technology and Built Environment

African Railway Center of Excellence

Research on Semiconductor Losses of Three-Phase Inverter for Traction Drive Considering Different Pulse Width Modulation Strategies

Prepared by: Woldie Kassie Ferede

Advisor: Abebe Teklu (PhD)

Co-Advisor: Mr. Alula Mebratu

October 10, 2025

Addis Ababa, Ethiopia

Addis Ababa University

College of Technology and Built Environment

African Railway Center of Excellence

Research on Semiconductor Losses of Three-Phase Inverter for Traction Drive Considering Different Pulse Width Modulation Strategies

Woldie Kassie Ferede

A Thesis Submitted to the Addis Ababa University School of Graduate Studies in Partial Fulfillment of the Requirements for the Degree of Master of Science in Railway Engineering (Traction and Train Control)

Advisor: Abebe Teklu (PhD)

Co-Advisor: Mr. Alula Mebratu

October 8, 2025

Addis Ababa, Ethiopia

Approval Page

As members of the board of examiners for the final Master's degree thesis presentation, we certify that we have read and evaluated the thesis paper prepared by Woldie Kassie, titled - **Research on Semiconductor Losses of Three-Phase Inverter for Traction Drive Considering Different Pulse Width Modulation Strategies** and that it fulfills the requirements for the Master of Science in Traction and Train Control Engineering.

Board of Examiners

Abebe Teklu (PhD)	_____	_____
(Main Advisor)	*Signature*	*Date*
Alula Mebratu	_____	_____
(Co-Advisor)	*Signature*	*Date*
_____	_____	_____
External Examiner	*Signature*	*Date*
_____	_____	_____
Internal Examiner	*Signature*	*Date*
_____	_____	_____
Chairperson	*Signature*	*Date*

Declaration

I declare that this thesis is entirely my own work and does not include any content from other educational institutions without proper acknowledgment. To the best of my knowledge, it does not contain previously published material by another person without recognition.

Mr. Woldie Kassie	*Date*
(Candidate)	

This is to certify that the above declaration made by the candidate is correct to the best of our knowledge.

Dr. Abebe Teklu	*Date*
(Thesis Main Advisor)	

Mr. Alula Mebratu	*Date*
(Thesis Co-Advisor)	

Abstract

Electric traction systems are essential to the global move toward sustainable and energy-efficient transportation, especially in the railway sector. At the center of these systems are three-phase inverters, which convert direct current (DC) into alternating current (AC) to power traction motors. The performance of these inverters largely depends on the semiconductor devices used. Si-IGBTs are commonly used due to their affordability and robust performance. However, they suffer from high conduction and switching losses, particularly at higher switching frequencies, which limits efficiency and increases thermal stress.

Therefore, it is important to develop a realistic loss estimation model for power semiconductors to overcome the limitations of device-specific commercial tools. Accurately modeling and estimating these losses is critical to understanding their impact on thermal behavior, efficiency, and the lifespan of the inverter.

In this thesis, conduction and switching losses in Si-IGBTs, free-wheeling diodes (FWDs), and SiC-MOSFETs are modeled using a common analytical model applicable to both Space Vector PWM (SVPWM) and Sinusoidal PWM (SPWM). The model combines a piecewise linear approximation for switching losses with a conduction loss model based on an equivalent third-order harmonic approximation of the duty cycle. Unlike commercial tools that are typically limited to specific device types, the developed model supports a broad range of semiconductor devices, enabling consistent and comparative loss evaluation.

Validation of the proposed model is conducted using MATLAB/Simulink and PLECS, and compared with commercial tools i.e. Semikron's SemiSel-V5 and Infineon's CIPM. The model is closely matches, and in some cases surpasses, commercial tools in accuracy. SiC-MOSFET-based inverters achieve 98.22% system efficiency, compared to 91.76% for Si-IGBT-based inverters, reflecting significant reductions in conduction and switching losses. Comparison with commercial tools shows minimal deviations: for the Infineon module, conduction and switching losses differ by less than 0.5%.

In conclusion,this research developed a versatile loss estimation model that outperforms commercial tools in accuracy and flexibility. As results confirm that SiC-MOSFETs deliver significantly higher efficiency than Si-IGBTs, making them the preferred solution for high-power traction applications.

Keywords: Semiconductor losses, Si-IGBT, SiC-MOSFET, freewheeling diode (FWD), Space Vector PWM (SVPWM), Sinusoidal PWM (SPWM), traction inverters, electric drives, permanent magnet synchronous motor (PMSM), thermal management

Acknowledgments

I would like to express my gratitude to those who supported me throughout my research.Special thanks to my advisor, **Dr.Abebe Teklu**, and my co-advisor, **Mr.Alula Mebratu**, for their invaluable guidance, encouragement, and support.I also extend my appreciation to my committee members for their insightful feedback and constructive suggestions.

Furthermore, I am deeply grateful to my family and friends for their support and assistance throughout this journey.Their belief in me has been a source of strength and motivation.

List of Abbreviations

Abbreviation	Description	Value/Unit
3LI	Three-Level Inverter	
AC	Alternating Current	
BEMF	Back Electromotive Force	
BLDC	Brushless Direct Current	
DC	Direct Current	
DTC	Direct Torque Control	
dq	Direct-Quadrature Reference Frame	
EMF	Electromotive Force	
Eoff	Turn-Off Energy Loss	mJ
Eon	Turn-On Energy Loss	mJ
EV	Electric Vehicle	
FET	Field-Effect Transistor	
FOC	Field-Oriented Control	
FW	Field Weakening	
FWD	Free-Wheeling Diode	
GaN	Gallium Nitride	
IGBT	Insulated Gate Bipolar Transistor	
IPM	Interior Permanent Magnet	
IPMSM	Interior Permanent Magnet Synchronous Motor	
MI	Modulation Index	-
MOSFET	Metal-Oxide-Semiconductor Field-Effect Transistor	

MTPA	Maximum Torque per Ampere	
PLECS	Piecewise Linear Electrical Circuit Simulation	
PI	Proportional-Integral	
PLL	Phase-Locked Loop	
PMSM	Permanent Magnet Synchronous Motor	
PWM	Pulse Width Modulation	
qd-axes	Quadrature and Direct Axes	
RBSOA	Reverse Bias Safe Operating Area	
Rth	Thermal Resistance	°C/W
SiC	Silicon Carbide	
SOA	Safe Operating Area	
SPWM	Sinusoidal Pulse Width Modulation	
SVPWM	Space Vector Pulse Width Modulation	
THD	Total Harmonic Distortion	%
VCES	Collector-Emitter Voltage	V
VDC	Voltage Direct Current	V
VGE	Gate-Emitter Voltage	V
VSI	Voltage Source Inverter	
ZDC	Zero d-Current	
Zth	Thermal Impedance	°C/W
$f_{\alpha\beta}$-axes	Alpha and Beta Axes (Stationary Reference Frame)	

List of Symbols

Symbol	Description	Unit
D	Duty cycle	-
f_{sw}	Switching frequency	kHz
I_{ref}	Datasheet test current	A
I_{rms}	Inverter output RMS current	A
I_{rmsI}, I_{aveI}	IGBT RMS and average current	A
I_{rmsM}, I_{aveM}	MOSFET RMS and average current	A
I_{rr}	Diode reverse recovery current	A
i_a, i_b, i_c	Inverter three-phase output current	A
i_{cap}	DC-link capacitor current	A
i_{ds}	MOSFET drain-source current	A
i_{in}, i_s	Inverter input and DC source current	A
i_o	Inverter output current	A
i_c, i_f	IGBT collector and diode forward current	A
M	Modulation index	-
P_{loss}	Switch total power loss	W
R_{thcs}, R_{thsa}	Case-heatsink and heatsink-ambient thermal resistance	°C/W
R_{thja}, R_{thjc}	Junction-ambient and junction-case thermal resistance	°C/W
T_a	Ambient temperature	°C
T_j	Junction temperature	°C
T_{ja}, T_{jc}	Junction-ambient and case temperature rise	°C
T_s	Switching period	ms
V_{dc}	Inverter DC-link voltage	V

V_{ref}	Datasheet off-state test voltage	V
V_{rms}	Inverter RMS output voltage	V
$V_{th}, V_{plateau}$	Gate threshold and plateau voltage	V
v_a, v_b, v_c	Inverter three-phase output voltage	V
v_{ce}	IGBT collector-emitter voltage	V
v_{ds}, v_{gs}	MOSFET drain-source and gate-source voltage	V
v_o	Inverter output voltage	V
E_{on}, E_{off}	Turn-on and turn-off energy losses	mJ

Table of Contents

List of Figures

List of Tables

Chapter 1

Introduction

1.1 Background

In recent decades, growing environmental concerns have led to a global transition from conventional energy generation based on fossil fuels to renewable energy sources [1]. This change has amplified the importance of electrical devices in railway systems. Power semiconductor devices are integral to the electrical conversion process, such as the transformation of direct current (DC) into alternate current (AC), a necessary step to drive traction motors [2]. Among these, the Interior Permanent Magnet Synchronous Motor (IPMSM) has gained prominence due to its superior efficiency and dynamic performance characteristics which are commonly used in modern electric rail systems.

Figure 1.1 illustrates the basic operation of a traction inverter, controlled by a microprocessor to adjust the frequency and voltage of the AC output to meet the speed and torque requirements of the traction motor [17]. Among the various inverter designs, the silicon (Si) Insulated Gate Bipolar Transistor (IGBT) is the most widely used technology . However, as the demand for high-performance and energy-efficient systems continues to increase, understanding and minimizing semiconductor losses within three-phase inverters has become a critical area of research [18].

In railway traction systems, two-level (2L) three-phase voltage source inverters (VSIs) are the most commonly used due to their reliability and efficiency [3]. These inverters typically rely on silicon (Si)–based IGBTs, valued for their affordability, maturity, and robust power handling capabilities. With blocking voltage ratings from 600 to 3300V, Si-IGBTs are well suited for railway traction and other high-power applications with variable DC-link voltage (1500 to 3600V) found in modern railways. They are also powerful and reliable for high-current applications with heat dissipation, slower switching speeds, and an efficiency challenge. New technologies such as SiC and GaN are emerging. Thus, this thesis thoroughly investigates loss modeling and identifies potential methods for improving drive efficiency [4, 5].

1.2 Motivation

Rapid progress in semiconductor technologies, such as SiC and GaN, is transforming power electronics by making systems more efficient, compact, and reliable, exactly what is needed for modern traction drive systems. Therefore, this research aims to tackle the challenge of reducing energy losses in three-phase inverters, paving the way for better performance and

more sustainable electric transportation.

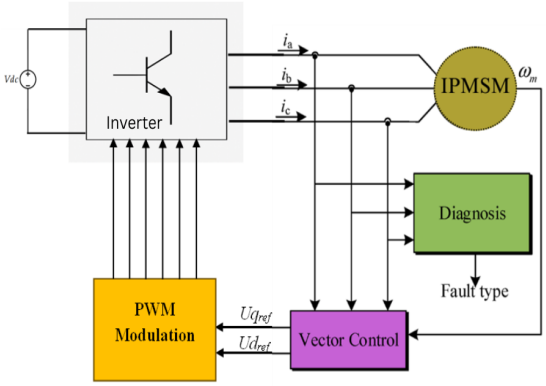

Figure 1.1: Basic Operation of a Traction Inverter for IGBT and SiC-MOSFETs [1].

1.2.1 Emerging Semiconductor Technologies

Recent advancements in semiconductor materials, particularly silicon carbide (SiC) and gallium nitride (GaN), offer pathways to overcome the limitations of traditional Si-IGBTs. Wide-band-gap materials exhibit superior properties, including higher breakdown voltages, faster switching speeds, and enhanced thermal conductivity. These attributes enable higher switching frequencies, reduced energy losses, and compact inverter designs with improved power quality. Figure 1.2 highlights how Si, SiC, and GaN technologies serve different purposes.Silicon is great for applications with lower power and frequency, SiC shines in high-power systems, and GaN is perfect for compact high-frequency designs [4]. Therefore, SiC MOSFETs might be the optimal choice for high-power, high-voltage applications such as railway traction systems, where thermal management and efficiency are critical. In contrast, GaN devices are better suited for smaller components with lower power, providing advantages in efficiency and compactness for secondary systems [7].

The three-phase inverter, a critical component of the traction drive, manages the flow of power between the energy source and the motor. However, the efficiency of these inverters is significantly influenced by the semiconductor losses that occur during the switching and conduction processes. These losses not only impact the system's energy efficiency, but also affect thermal management and long-term reliability [3, 6]. Optimizing inverter operation is essential to address these challenges, and Pulse Width Modulation (PWM) strategies play a crucial role in this context. Different PWM techniques, such as sinusoidal PWM (SPWM) and space vector PWM (SVPWM), offer varying trade-offs between switching frequency, harmonic distortion, and overall efficiency. A comprehensive evaluation of these strategies is necessary to identify the most effective approach to minimize semiconductor losses in traction drive applications [8, 14].

In the context of electric vehicles, including trains and trams, three-phase Voltage Source Inverters (VSIs) are used to convert the DC power from the vehicle battery into AC .These VSIs are integral to the drive train, influencing the overall vehicle performance and efficiency . Despite their importance, significant energy losses occur in the semiconductor switches used within these inverters.These losses can substantially impact inverter performance and drive

train efficiency [12, 19].The modulation technique used to control the inverter plays a vital role in its performance .The two common techniques are SPWM and SVPWM [4, 8].

These modulation strategies affect the efficiency of the inverter and the losses associated with semiconductor devices . SiC MOSFETs, with superior characteristics over traditional IGBTs, offer improved performance in terms of efficiency and thermal dissipation[20, 7] . Traction inverters are typically used in conjunction with a DC link, which is a capacitor bank that stores energy and helps to smooth out the DC input voltage .The inverter then converts the DC voltage from the DC link into AC voltage, which is then used to drive the traction motors, in this case IPMSM .

Consequently, this research aims to analyze semiconductor losses in three-phase inverters for traction drives under different PWM strategies. Exploring the relationship between modulation techniques, loss mechanisms, and system performance, the study aims to provide valuable information to optimize inverter design and advance the efficiency of electric transportation systems[11] .

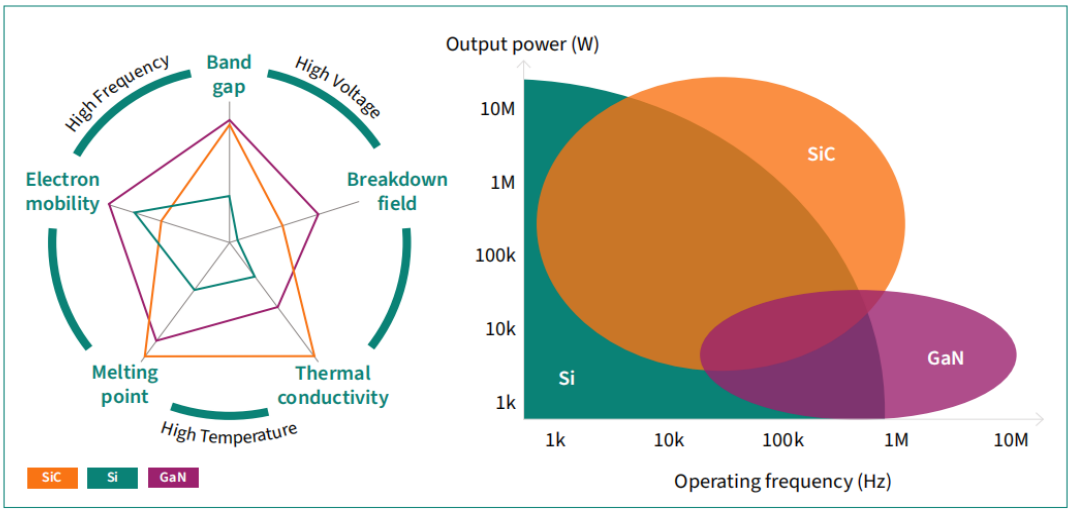

Figure 1.2: Showcasing Si, SiC, and GaN technologies in terms of operating frequency and output power for various applications [2].

1.2.2 Manufacturer Simulation Tools

There are several simulation tools provided by power semiconductor manufacturers that enable the estimation of power losses and junction temperatures of devices used in various inverter topologies . Typically, the user begins by selecting a specific inverter topology and entering relevant application parameters, such as switching frequency, load profile, Dc Voltage and ambient temperature .

Among the most widely used manufacturer tools are SemiSel-V5^{TM} from Semikron Danfoss [21], CIPOS IPM^{TM} (CIPM) [22] from Infineon Technologies, and DriveSize from ABB [23]. These platforms allow users to input design parameters such as DC-link voltage, switching frequency, load profile, and cooling method [24]. Based on the parameters provided, suitable power modules can be selected, and finally the power losses can be calculated. Based on these inputs, the tools recommend suitable power modules and calculate:

✓ Conduction and switching losses

✓ Power dissipation and efficiency

✓ Junction and case temperatures

These tools are highly regarded in industry because of their accurate, manufacturer-validated models and intuitive interfaces. Despite their usefulness, manufacturer simulation tools exhibit several limitations, particularly when applied to academic research and system-level innovation.

1. Limited Flexibility: The software often supports only predefined topologies and standard modulation techniques, restricting exploration of custom inverter designs or control strategies.

2. Closed Architecture: These tools typically operate as closed systems, limiting export functionality and integration with external platforms such as MATLAB or PLECS for co-simulation or data analysis.

3. Lack of Control System Integration: Manufacturer tools usually do not support integration with controller design environments or hardware-in-the-loop (HIL) systems, which are crucial for complete system validation .

To overcome these constraints, this study adopts a flexible simulation framework based on MATLAB/Simulink, and PLECS , through analytical modeling techniques. This approach enables the investigation of semiconductor losses of Si-IGBTs and SiC MOSFETs under SPWM and SVPWM modulation strategies [25] . The flexibility of this platform allows for customized control strategies and topology configurations, offering a better inverter performance. Furthermore, results from various manufacturer tools are presented in Chapter 5 for benchmarking and validation purposes,improving the reliability of the findings .

These tools are used for comparison between analytical calculations and values obtained from MATLAB and PLECS simulations .

1.3 Statement of the Problem

As of today, most electric powered traction systems widely use IGBT. In medium power drives, the switching frequency of IGBTs is limited to between 500-30kHz due to the considerable amount of switching losses [26] .This restriction creates many problems,low-order harmonics may appear due to low switching frequencies,increased electromagnetic interference (EMI), higher acoustic noise, reduced power quality, and elevated thermal stress on the power components .This situation decreases power quality and overall energy conversion efficiency and creates torque ripple at integer multiples of the fundamental frequency [9, 27] .

The research aims to investigate and address critical issues in traction inverter systems by focusing on the following key questions .

1. What are the primary sources of semiconductor losses in traction inverters, specifically for Si-IGBTs, diodes, and SiC-MOSFETs ?
2. How can a comprehensive model be developed to predict semiconductor losses in real-time for traction inverter systems ?
3. What are the unique loss characteristics of SiC-MOSFETs compared to Si-IGBTs in traction drive applications ?
4. What potential improvements can be identified to enhance the efficiency of traction drive?

1.4 Objectives

1.4.1 General Objective

The general objective of this thesis is to investigate and develop a realistic model of semiconductor losses for traction inverters, focusing on Si-IGBTs, and SiC MOSFETs .

1.4.2 Specific Objectives

The specific objectivesof the thesis are:

- ✓ To comprehensively analyze the various sources of Si-IGBT loss in the traction inverter.
- ✓ To investigate the loss aspect of SiC-MOSFET in traction drive application .
- ✓ To develop loss estimation MATLAB/PLECS model and conduct a comprehensive comparison with commercially available loss simulation toolbox.
- ✓ To address drive efficiency improvement from inverter loss perspective .

1.5 Literature Review

Study of semiconductor losses in three-phase inverters is important for optimizing traction drive systems. Over the years, many investigations have focused on the analysis of switching and conduction losses of power semiconductor devices to drive efficiency at both the energy and system reliability levels. Several studies examined the performance of IGBT- and SiC-based inverters, effects of different PWM techniques on loss reduction, and high-level control techniques for optimal energy dissipation minimization. This section reviews significant contributions in this area, highlighting key findings and their impact on the performance of modern traction inverters .

A notable approach proposed [28] provides a comprehensive analysis of power losses in PWM inverters using IGBT devices. The authors develop analytical models to quantify conduction losses, switching losses, and other loss components in IGBT-based inverters, considering factors such as modulation index, power factor, and IGBT parameters. However, the study does not fully address the impact of thermal effects on IGBT performance under varying operational

conditions . The insights from this work can guide the design and optimization of high-efficiency IGBT inverters for various industrial and power conversion applications .

Another study by [29] focused on real-time estimation of the IGBT junction temperature in automotive applications. Accurate monitoring of the junction temperature is crucial for monitoring the thermal state of IGBT devices and preventing overload in electric vehicle drivetrain systems. However, the study does not fully address variations in junction temperature under dynamic driving conditions, which could be further explored for more accurate temperature monitoring.The study likely explores techniques such as the use of NTC sensors to indirectly infer the junction temperature, while also considering the calculation of power losses in the IGBT and free-wheeling diode as an integral part of the temperature estimation approach.

The study in [30] conducted a comprehensive mode, simulation, and analysis of losses and current/voltage ripple in traction inverters.However, the study does not fully address the impact of system-level integration and external factors like load variations and environmental conditions on the inverter's performance.As a prominent researcher in power electronics, Kolar's expertise in loss modeling and analysis is reflected in this study, which aims to provide a thorough understanding of the various loss mechanisms in traction inverters to support the design of high-efficiency EV drivetrains.

In [15], the authors presented a model conduction and switching loss for IGBT and free-wheeling diode (FWD) devices in electric vehicle drive applications.The focus on SVPWM-based loss modeling is particularly relevant for electric vehicle(EV) traction inverters, which commonly employ this PWM technique. The insights from this work can contribute to the design and control optimization of high-efficiency electric drivetrain systems.

Finally,[11, 15] proposed more reliable models for the conduction and switching losses of IGBT and FWD devices in electric vehicle drive applications. The focus on SVPWM-based loss modeling is particularly relevant for EV traction inverters, which commonly employ this PWM technique.The insights from this work can contribute to the design and control optimization of high-efficiency electric drivetrain systems.

In summary, these studies highlight how crucial it is to reduce semiconductor losses in traction inverters in order to increase the efficiency of electric vehicles. The study helps to improve the efficiency and dependability of electric drive-trains by improving models for conduction, switching losses, and temperature estimation. Furthermore, the emphasis on SVPWM-based loss modeling contributes to the development of more energy-efficient systems, which advances the creation of better and more environmentally friendly electric vehicles.

1.6 Methodology

This section presents the methodology employed in this research to analyze semiconductor losses in three-phase traction inverters under different PWM strategies. The process followed a structured approach involving problem identification, analytical modeling, simulation implementation, performance evaluation, and validation. The overall methodology is depicted in Figure 1.3. The methodology includes the following sequential steps:

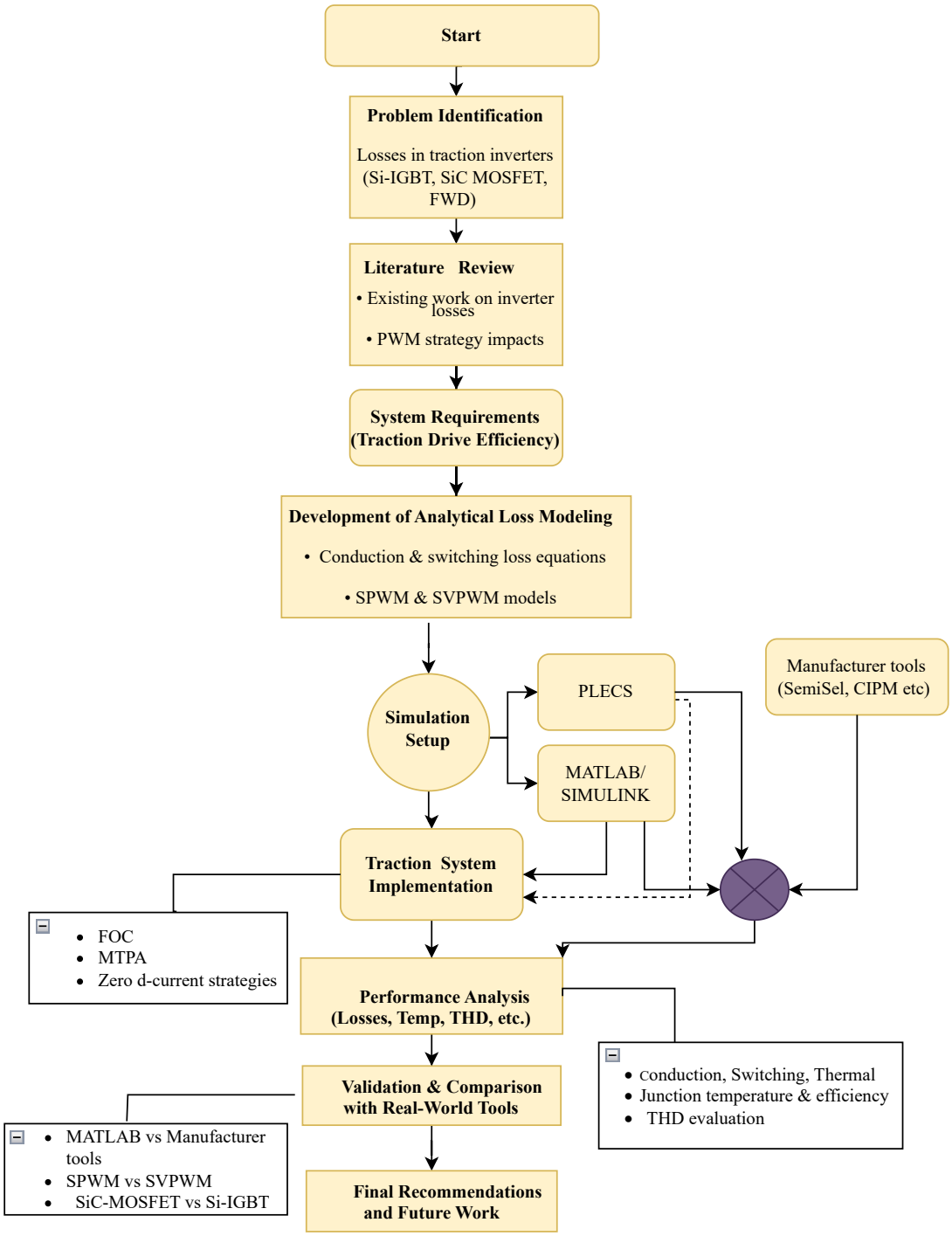

Figure 1.3: Overall research methodology adopted for analyzing inverter losses in traction drives.

✓ Problem Identification: The study begins by identifying energy losses in traction inverters caused by semiconductor devices such as Si-IGBTs, SiC-MOSFETs, and free-wheeling diodes (FWDs). The inefficiencies related to conduction and switching losses, especially at high switching frequencies, were outlined as critical challenges.

- ✓ Literature Review: The review of previous works was conducted to understand existing inverter loss models, PWM strategies (SPWM and SVPWM), and the impact of semiconductor technologies on system efficiency. The gaps in simulation flexibility and real-time loss prediction were also highlighted.

- ✓ Development of Analytical Models: The research developed analytical models to evaluate conduction and switching losses for Si-IGBTs and SiC-MOSFETs. The models worked with both SPWM and SVPWM strategies to calculate losses through device characteristics and modulation indices.

- ✓ Simulation Setup: MATLAB/Simulink and PLECS environments were used to simulate inverter performance and validate the analytical models. Furthermore, simulation tools from device manufacturers, such as SemiSel-V5 and Infineon's CIPM, were used for benchmarking and comparison.

- ✓ Traction Drive System Implementation: The inverter models were integrated into a complete traction drive system, employing an Interior Permanent Magnet Synchronous Motor (IPMSM). Field-Oriented Control (FOC), Maximum Torque Per Ampere (MTPA), and Zero d-axis current control were applied for realistic dynamic response analysis.

- ✓ Performance Evaluation: The evaluation included total power loss, switching and conduction losses, thermal behavior, junction temperature, and Total Harmonic Distortion (THD). The evaluation of both SPWM and SVPWM modulation strategies was also performed on different inverter modules (ABB, Infineon, Semikron).

- ✓ Validation and Comparison: The analytical and simulated results were validated by using data from commercial online tools. Comparative studies were conducted to determine the relative performance of SPWM vs SVPWM and Si-IGBT vs SiC-MOSFET in terms of loss reduction and efficiency improvement.

1.7 Contributions

The main contributions of this thesis are the novel insights into the analysis and optimization of semiconductor losses in three-phase inverters for traction drives. This research investigates various Pulse Width Modulation (PWM) strategies and their impact on system efficiency. The following are the key contributions:

- ✓ Analysis of Semiconductor Losses: A comprehensive analysis of semiconductor losses in three-phase inverters used for traction drives, with a focus on different semiconductor devices such as Si-IGBTs, SiC MOSFETs, and diodes.

- ✓ Investigation of PWM Strategies: A detailed investigation of various Pulse Width Modulation (PWM) strategies, including Sinusoidal PWM, Space Vector PWM, and others, to assess their impact on semiconductor losses in the inverter system.

- ✓ Efficiency Comparison: A comparative study that evaluates the performance and efficiency of three-phase inverters under different PWM strategies, with a focus on energy loss reduction and optimization of system performance.
- ✓ Simulation and Validation: The development of simulation models in MATLAB and PLECS to predict and validate semiconductor losses under varying operating conditions, demonstrating the effects of different PWM strategies on inverter performance.
- ✓ Guidance for Optimizing Inverter Design: Providing practical insights and recommendations on the optimal selection of PWM strategies to minimize semiconductor losses, thereby enhancing the efficiency of traction inverters in electric drive systems.

1.8 Thesis Scope

This thesis focuses on the modeling and analysis of semiconductor losses in traction inverters, with an emphasis on Si-IGBTs, diodes, and SiC MOSFETs. The research involves developing a comprehensive loss estimation model and performing simulations to validate the results. The scope includes:

1. Model Development for Loss Estimation:
   - ✓ Utilizing MATLAB for the development of comprehensive models, simulation, and data analysis to estimate and predict semiconductor losses in traction inverters.
   - ✓ Analysis of both conduction and switching losses for each type of semiconductor devices.
2. Simulation and Dynamic Analysis of Traction Inverters :
   - ✓ Study of the dynamic responses of Si-IGBTs, diodes, and SiC MOSFETs, with a focus on their impact on the efficiency of the overall inverter system.
3. Comparison and Validation with Commercial Simulation Tools:
   - ✓ Utilizing online simulators and commercially available simulation tools to validate the accuracy and performance of the proposed loss estimation model.
   - ✓ Benchmarking the performance of Si-IGBTs, diodes, and SiC MOSFETs, comparing their efficiency and reliability under diverse operational scenarios.

1.9 Thesis Outline

The contents of this thesis are organized as follows:

Chapter 1: provides the background of this thesis work and an overview of how this thesis research is organized.

Chapter 2: This chapter explores advanced control strategies for three-phase traction inverters. It details the inverter topologies investigated in this study and their associated modulation techniques.

Chapter 3: This chapter presents the theoretical framework and a step-by-step modeling process for the traction drive system. It emphasizes the inter-dependencies between the inverter, motor, and control strategy.

Chapter 4: This chapter develops analytical power loss models for the three-level inverters (3LIs) analyzed in this study. It describes methods for calculating semiconductor losses under various operating conditions in detail.

Chapter 5: This chapter provides simulation models and results based on the proposed methodology. It evaluates the power loss distributions of the three examined three-phase 3LIs using both analytical approaches and detailed circuit simulation models. Comparisons are made, and significant findings are discussed.

Chapter 6: The final chapter summarizes the key contributions and findings of this research. It also addresses the study's limitations and proposes potential directions for future work.

Chapter 2

Semiconductor Devices in Converters and Pulse Width Modulation Techniques

This section introduces high-performance inverters used in railway applications, the advantages of semiconductor devices, principles of device selection, and PWM technologies employed in three-phase inverters [20].

2.1 High-Performance Three-Phase Traction Inverter

The power inverter is the fundamental energy control unit of the Electric Vehicle (EV) traction line [15]. Its main function is to convert the available DC battery voltage into three (or more) sinusoidal phase voltages of adjustable frequency and amplitude to drive the traction motor. In railway applications, the traction inverter plays a crucial role in the propulsion of electric trains and locomotives [15, 31].

The basic structure of an inverter shown in Figure 2.1 consists of semiconductor devices such as IGBTs/ SiC-MOSFETs, the IPMSM and the DC-Link. The semiconductor components are used for efficient and reliable power switching [32], the DC-link capacitor for DC-voltage stabilization and minimization of voltage fluctuation [24] , and the gate signals are delivered by the gate driver circuits. The control signal are generated by the control units by receiving sensors data and adjusting the inverter output for effective control of the motor [33] . Meanwhile, the cooling system dissipate the substantial heat generated during operation, using methods such as liquid cooling or forced air cooling to maintain optimal operating temperatures [34] .

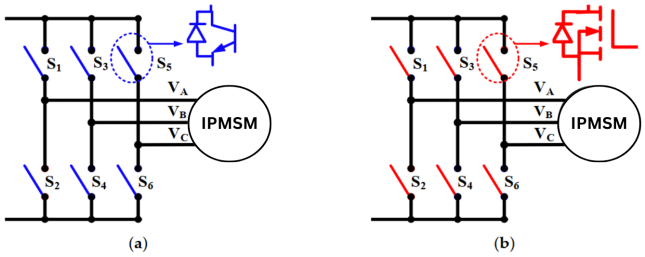

Figure 2.1: Basic inverter circuit diagram of (a) IGBT and (b) SiC MOSFET [3].

The major key components of railway traction converters can be categorized as follows.

a. Power semiconductor devices, such as IGBTs or SiC MOSFETs, are used for efficient and reliable power switching [35].

b. DC link capacitor, which stabilizes the DC voltage and minimizes voltage fluctuations in the DC circuit of the traction inverter [20].

c. Gate drive circuit, responsible for providing the necessary signals to control the switching of power semiconductor devices and to ensure accurate timing and control of power flow [26].

d. Control unit, which manages the overall operation of the system by receiving input from sensors such as speed, acceleration, and braking, and adjusts the inverter's output accordingly. It also monitors and protects the inverter from abnormal operating conditions [26].

e. Cooling system, which is used to dissipate the substantial heat generated during operation, using methods such as liquid cooling or forced air cooling to maintain optimal operating temperatures [36].

A railway traction inverter is an essential component of an electric or hybrid train system .These functionalities collectively enable the efficient and reliable operation of the IPMSM in railway traction applications as stated in [34, 37].

a. **DC-AC Conversion :** Converts DC power from the overhead catenary system or onboard storage into three-phase AC power.

b. **Motor Control :** Regulates the frequency, amplitude, and phase of AC output to control the traction motors.

c. **Regenerative Braking :** Recovers kinetic energy during braking and converts it into electrical energy; the inverter converts it back to DC.

d. **Safety and Protection :** Equipped with over-current, over-voltage, short-circuit protection, and temperature monitoring.

2.2 Semiconductor Devices in Converter Systems

In this section, the working principles of different power semiconductor devices, used in inverters, are explained . As in this thesis work, power loss comparison is made between Si-IGBT / SiC-MOSFET inverters ; it is necessary to have a glance at the working principles of IGBTs, SiC-MOSFETs and Diodes.

2.2.1 Types of Power Semiconductor Devices

Power semiconductor devices are essential components in industrial three-phase inverters. Among the most widely used are IGBTs, which are known for their high current-handling capability, high breakdown voltage, and adequate switching performance [38]. In recent years,

SiC-MOSFETs have gained significant attention for high-power applications due to their superior switching speed, higher efficiency, and stable performance at elevated temperatures up to 400°C.

While silicon carbide devices enable the design of smaller and more efficient power converters, they are generally more expensive per unit area compared to traditional silicon-based devices. Their cost-effectiveness depends on the specific application. Additionally, their resistance tends to increase at higher temperatures, which may lead to higher conduction losses. On the other hand, silicon devices offer more predictable loss characteristics, making them a favorable choice for cost-sensitive applications that also demand reliable thermal performance [39, 40, 41].

Although silicon carbide devices offer advantages like smaller size and higher efficiency, they tend to be more expensive than silicon-based devices. Their cost-effectiveness depends on the application. Additionally, silicon carbide devices can experience higher resistance at elevated temperatures, leading to increased conduction losses, whereas silicon devices generally maintain more stable performance [39, 40, 41].

Table 2.1 summarizes the main differences between silicon and silicon carbide devices. Device characteristics can vary depending on simulation models such as MATLAB and manufacturer specifications.

Table 2.1: Advantages of SiC MOSFETs Compared to IGBTs.

Advantages of SiC MOSFETs	**Advantages of IGBTs**
Higher switching frequencies	Lower cost per unit area
Lower switching losses	Established and mature technology
Higher temperature operation	Lower gate drive requirements
Higher power density	Wide availability and industry support
Reduced cooling requirements	Better performance at lower voltages
Potential for smaller system size and weight	Lower risk of short-circuit failures
Enhanced system efficiency	Better performance in certain voltage and current ranges

2.3 Selection Criteria of Semiconductor Devices

Like any other drive application, a traction drive system has its own requirements that need to be met in order to achieve favorable performance . Proper selection of control and modulation techniques, along with semiconductor devices, is vital for optimizing the performance of a two-level, three-phase inverter motor drive used in traction applications . Each technique possesses different characteristics that significantly influence the overall efficiency, reliability, and functionality of the drive system .

Furthermore ,the selection of semiconductor devices particularly IGBTs and SiC MOSFETs is a fundamental aspect of inverter design, as it directly affects system efficiency, thermal performance, and reliability we focus on the selection criteria besed on this . The selection of semiconductor devices for this thesis, which focuses on loss modeling of IGBTs and SiC-MOSFETs, is guided by several important factors as Figure 2.2.

a. Maximum phase current to the machine and V_{CE} : The selected device must withstand the peak phase current without exceeding its collector-emitter voltage limit to ensure safe and reliable operation.

b. Maximum DC-link voltage : The device's voltage rating must be higher than the maximum expected DC-link voltage to avoid electrical breakdown and ensure long-term stability.

c. Maximum switching frequency : Devices must support the inverter's required switching frequency with minimal switching losses to maintain efficiency and thermal limits.

d. Maximum junction temperature : This parameter determines the thermal limits of the device. Operating too close to the maximum temperature can reduce lifespan and reliability.

e. Maximum ambient or boundary temperature : The environmental temperature around the device affects its cooling and thermal management . Adequate thermal design is necessary to prevent overheating.

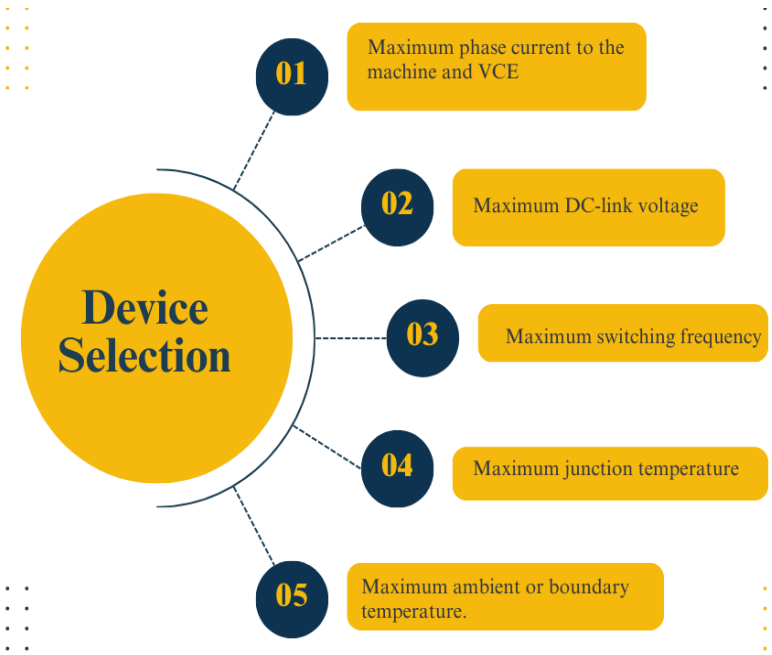

Figure 2.2: Selection Criterion's for Semiconductor Device [4].

An investigation of the most key criteria for selecting the best control and modulation methods in traction applications is presented in Figure 2.3 .The key factors include:

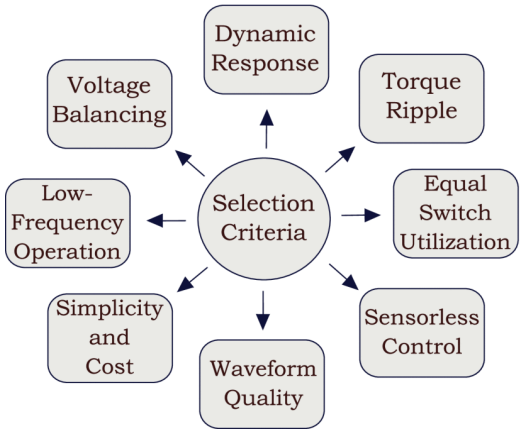

Figure 2.3: Selection Criteria for Control and Modulation Techniques [4].

✓ Switching Frequency: This parameter defines the frequency at which the inverter switches, influencing thermal performance and efficiency. Higher switching frequencies can be used to minimize passive component sizes but will tend to increase switching activity-generated losses.

✓ Dynamic Response: The inverter's ability to respond quickly to changes in load or commands is crucial. A fast dynamic response is necessary for maintaining optimal motor performance during acceleration, deceleration, and load variations.

✓ Torque Ripple: Minimizing variations in torque output is essential for ensuring smooth operation, reducing vibrations, and enhancing comfort in traction applications.

✓ Equal Switch Utilization: Ensuring balanced use of all switches prevents excessive wear and thermal stress, enhancing reliability and longevity of the inverter system.

✓ Sensorless Control: Techniques that eliminate the need for physical sensors simplify system design and reduce costs while still providing accurate control.

✓ Waveform Quality: Maintaining high-quality output waveforms is vital for minimizing harmonic distortion, leading to improved motor efficiency and reduced heating.

✓ Simplicity and Cost: The complexity of the control strategy impacts development time and costs. Simpler methods are often more cost-effective and easier to implement.

✓ Low-Frequency Operation: The ability to operate effectively at low frequencies is important for delivering high torque at low speeds, suitable for applications like electric vehicles.

✓ Voltage Balancing: Ensuring equal voltage levels across all motor phases improves efficiency and system stability, preventing overheating and enhancing performance.

2.4 PWM Technologies

There are several switching techniques employed in power electronic converters to control the switching of power devices such as transistors (IGBTs, MOSFETs) or diodes .In this section two of the PWM technilogies are presented [42].

2.4.1 Sinusoidal Pulse Width Modulation Technique

SPWM controls the inverter's output by comparing three 120°-shifted sinusoidal reference waves with a triangular carrier wave [37, 9]. Based on amplitude comparisons, switches (S1, S2) are turned on/off to manage current flow, as shown in Figure 2.4 for the upper switches of Figure 2.1.

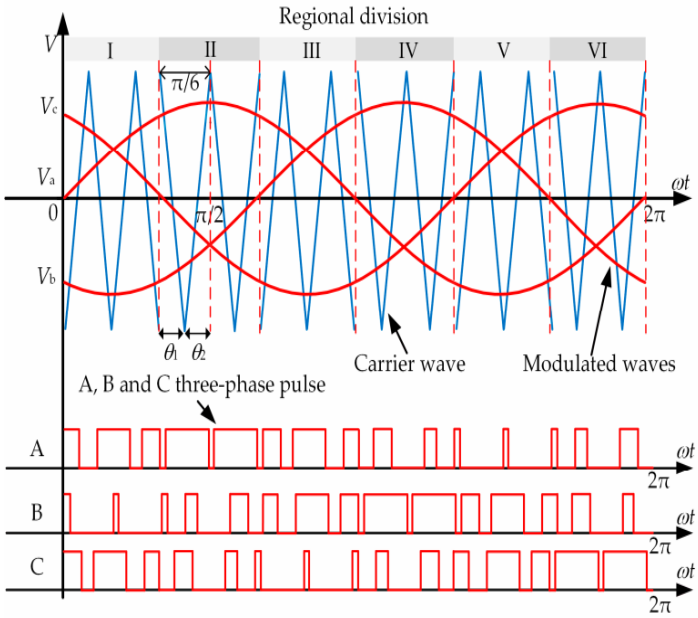

Figure 2.4: Three-phase modulation wave region division and output pulse.

A high-frequency triangular carrier wave Ac is compared with a sinusoidal control signal Ar at the desired frequency. The modulation index (ma) in 2.1 controls the fundamental frequency, while the frequency modulation index (mf) in 2.2 governs the reference and fundamental frequencies . The modulation index m_a is defined by the formula :

$$m_a = \frac{A_c}{A_r} \tag{2.1}$$

Where m_a is the modulation index, A_c is the amplitude of the control signal, and A_r is the amplitude of the reference signal [43]. The frequency modulation index, m_f, is defined by the formula :

$$m_f = \frac{f_r}{f_1} \tag{2.2}$$

where m_f is the frequency modulation index, f_r is the reference frequency, and f_1 is the fundamental frequency.

The number of pulses in each output signal cycle is determined by the carrier frequency. It is worth mentioning that no two switches in the same bridge arm conduct at the same time [7]. To illustrate this , Figure 2.4 depicts a typical output voltage waveform in SPWM [44] .

2.4.2 Space Vector Pulse Width Modulation (SVPWM)

SVPWM is a commonly used modulation scheme for the field-oriented control of the PMSM [45, 46, 47]. The main goal of SVPWM is to minimize the switching losses, reduce the harmonic distortion, and properly utilize DC bus voltage [48, 14]. In addition, the SVPWM scheme effectively reduces total harmonic distortion, as well as current and torque ripples.

This is achieved through the use of eight distinct switching states, with the lower switches being the opposite of the upper ones [47]. The resulting phase voltages are converted into the $\alpha\beta$ reference frame [46], creating six active voltage vectors and two zero vectors. These vectors define six sectors: $V_1, V_2, \ldots, V_6$. Unlike other PWM methods, SVPWM uses a vector reference, making it easier to understand the system [49] . The relationship between the switching vector $[a, b, c]^T$ and the line-to-line voltage vector $[V_{ab}, V_{bc}, V_{ca}]^T$ is established through equations (2.3), (2.4), and (2.5).

$$V_{ab} = V_{dc}(V_a - V_b) \tag{2.3}$$

$$V_{bc} = V_{dc}(V_b - V_c) \tag{2.4}$$

$$V_{ca} = V_{dc}(V_c - V_a) \tag{2.5}$$

Also, the relationship between the switching variable vector can be written as :

$$\begin{bmatrix} V_{an} \\ V_{bn} \\ V_{cn} \end{bmatrix} = \frac{V_{dc}}{3} \begin{bmatrix} 2 & -1 & -1 \\ -1 & 2 & 1 \\ -1 & -1 & 2 \end{bmatrix} \begin{bmatrix} a \\ b \\ c \end{bmatrix} \text{ [50]} \tag{2.6}$$

According to 2.3, 2.4,and 2.5, the eight switching vectors, phase voltages, and line-to-line voltages in terms of DC-link voltage are shown in Table 2.2. The table lists the eight inverter voltage vectors (V_0 to V_7), including six active vectors and two zero vectors [45].
In the stationary reference frame, the three-phase sinusoidal voltage components are as follows:

$$V_a = V_m \sin(\omega t) \tag{2.7}$$

$$V_b = V_m \sin\left(\omega t + \frac{2\pi}{3}\right) \tag{2.8}$$

$$V_c = V_m \sin\left(\omega t - \frac{2\pi}{3}\right) \tag{2.9}$$

When this three-phase voltage is applied to the three-phase machines it produces a rotating flux, and this rotating resultant flux can be represented as a single rotating voltage vector [51].

The objective of the PWM technique of the space vector is to approximate the reference voltage vector V_{ref} using the eight switching patterns. Reference voltage over one PWM period is given by 2.10:

$$V_{\text{ref}} \cdot T_s = \vec{V}_1 \cdot T_1 + \vec{V}_2 \cdot T_2 + \vec{V}_0 \cdot T_0 \tag{2.10}$$

Based on figure 2.6 the reference voltage is described as 2.11 , Since $\vec{V}_0 = 0$, this reduces to:

$$\vec{V}_{\text{ref}} = \frac{T_1}{T_s}\vec{V}_1 + \frac{T_2}{T_s}\vec{V}_2 \tag{2.11}$$

This method maximizes the utilization of the DC bus voltage by producing a higher fundamental output voltage compared to traditional sinusoidal PWM, reduces harmonic distortion in the output waveform, and improves the dynamic response and efficiency of the motor drive system. Figure 2.6 illustrates how the inverter determines the sector containing the reference voltage vector, from which the adjacent active vectors $\vec{V}_1$ and $\vec{V}_2$ are derived for the space vector PWM implementation.

Table 2.2: Switching states and corresponding line-to-neutral and line-to-line voltages [12].

Voltage	**Switching Vectors**			**Line to Neutral Voltage**			**Line to Line Voltage**			**Switches**
Vectors	**a**	**b**	**c**	V_{an}	V_{bn}	V_{cn}	V_{ab}	V_{bc}	V_{ca}	**Active, Null**
V_0	0	0	0	0	0	0	0	0	0	S_4, S_2, S_6
V_1	1	0	0	$\frac{2}{3}$	$-\frac{1}{3}$	$-\frac{1}{3}$	1	0	-1	S_6, S_2, S_1
V_2	1	1	0	$\frac{1}{3}$	$\frac{1}{3}$	$-\frac{2}{3}$	0	1	-1	S_1, S_3, S_2
V_3	0	1	0	$-\frac{1}{3}$	$\frac{2}{3}$	$-\frac{1}{3}$	-1	1	0	S_4, S_3, S_2
V_4	0	1	1	$-\frac{2}{3}$	$\frac{1}{3}$	$\frac{1}{3}$	-1	0	1	S_4, S_3, S_5
V_5	0	0	1	$-\frac{1}{3}$	$-\frac{1}{3}$	$\frac{2}{3}$	0	-1	1	S_4, S_6, S_5
V_6	1	0	1	$\frac{1}{3}$	$\frac{2}{3}$	$\frac{1}{3}$	1	-1	0	S_1, S_6, S_5
V_7	1	1	1	0	0	0	0	0	0	S_1, S_3, S_5

The vector V is given by:

$$\vec{V}_1 = \frac{2}{3}(V_a + aV_b + a^2V_c)$$

$$\vec{V}_1 = \frac{2}{3}\left(\frac{2}{3} - \frac{1}{3}a + \frac{1}{3}a^2\right)$$

where a is defined as: $a = e^{j\frac{2\pi}{3}}$

$$\vec{V}_1 = \frac{2}{3} + 0j = \frac{2}{3}\angle 0°. \tag{2.12}$$

$$\vec{V}_2 = \frac{2}{3}\left(\frac{1}{3} + \frac{1}{3}a - \frac{2}{3}a^2\right)$$

$$\vec{V}_2 = \frac{1}{3} + \frac{1}{\sqrt{3}}j = \frac{2}{3}\angle 60° \tag{2.13}$$

The block diagram in Figure 2.6 demonstrates the calculation of sector and adjacent switching states of a two-level voltage source inverter for all sectors.

To implement the space vector PWM, the voltage equations in the abc reference frame can

be transformed into the stationary dq reference frame that consists of the horizontal (d) and vertical (q) axes, as depicted in Figure 2.5.

From Figure 2.5, the relationship between these two reference frames is as follows:

$$f_{dqo} = k_s \cdot f_{abc} \tag{2.14}$$

As described in Figure 2.5 , this transformation is equivalent to an orthogonal projection of onto the two-dimensional perpendicular to the vector (the equivalent d-q plane) in a three-dimensional co-ordinate system (Clarke transformation).

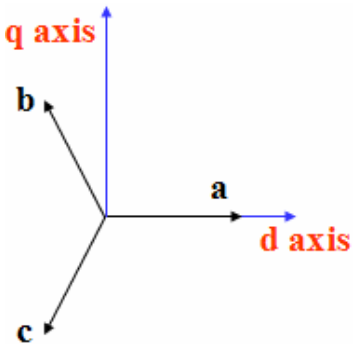

Figure 2.5: The relationship of *abc* reference frame and stationary *dq* reference frame

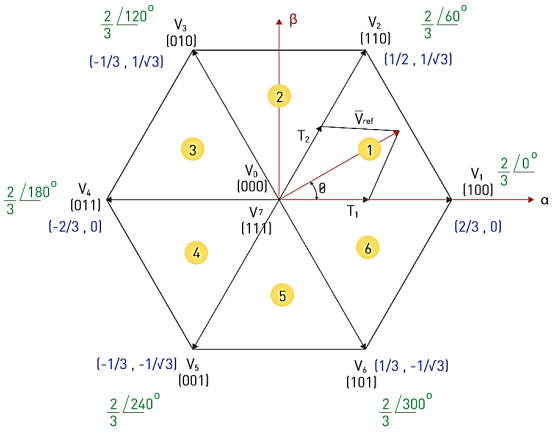

Figure 2.6: Calculation of Sector and Adjacent Switching States.

Chapter 3

Theory and Modeling of the Traction Drive System

In this chapter, the mathematical model of the IPMSM is presented as the foundation for analyzing the traction drive system. Based on this model, key components such as the inverter topology, switching strategies, and load characteristics are modeled to reflect their influence on overall system performance. Additionally, Field-Oriented Control (FOC), Maximum Torque Per Ampere (MTPA), and Zero d-axis current control are introduced to enhance efficiency, torque performance,and system simplicity in traction applications.

3.1 Frame Transformation

To simplify the analysis and control of AC machines, it is common to transform the three-phase quantities into a rotating reference frame using Clarke and Park transformations .This allows the decoupling of torque and flux components, making control more efficient and intuitive [52, 31] .

The two primary transformations employed are the Clarke transformation and the Park transformation. The Clarke transformation was first developed by Edith Clarke. It is standard procedure to convert system state variables from the three-phase system (a, b, and c) to an orthogonal (α and β) reference frame, as illustrated in Figure 3.1, for modeling the FOC drive system [37].

Figure 3.1: Clarke Transform [5].

$$V_{\alpha\beta0} = T_{\alpha\beta0}(\theta)V_{abc}$$

$$V_{\alpha\beta0} = \frac{2}{3}\begin{bmatrix} \cos(\theta) & \cos\left(\theta - \frac{2\pi}{3}\right) & \cos\left(\theta + \frac{2\pi}{3}\right) \\ \sin(\theta) & \sin\left(\theta - \frac{2\pi}{3}\right) & \sin\left(\theta + \frac{2\pi}{3}\right) \\ \frac{1}{2} & \frac{1}{2} & \frac{1}{2} \end{bmatrix} \text{ [53]} \tag{3.1}$$

In three-dimensional space, the vectors α and β are said to be orthogonal to the (abc) frames

[54]. This implies that the angle θ between them is 90°, as indicated by the condition $\alpha \cdot \beta = 0$. Consequently, this orthogonality simplifies the analysis of their interactions [55].

$$\begin{bmatrix} V_\alpha \\ V_\beta \\ 0 \end{bmatrix} = \begin{bmatrix} 1 & \frac{1}{2} & -\frac{1}{2} \\ 0 & \frac{\sqrt{3}}{2} & -\frac{\sqrt{3}}{2} \\ \frac{1}{2} & \frac{1}{2} & \frac{1}{2} \end{bmatrix} \begin{bmatrix} V_a \\ V_b \\ V_c \end{bmatrix} \text{ [56]} \tag{3.2}$$

In the context of a balanced system, as shown in 3.4, the zero sequence component is equal to zero [57, 58]. The inverse Clarke transformation from V_{abc} to $V_{\alpha\beta 0}$ is given by:

$$V_{abc} = T^{-1}_{\alpha\beta 0}(\theta) \cdot V_{\alpha\beta 0} \tag{3.3}$$

$$\begin{bmatrix} V_a \\ V_b \\ V_c \end{bmatrix} = \begin{bmatrix} \cos(\theta) & \sin(\theta) & 1 \\ \sin\left(\theta - \frac{2\pi}{3}\right) & \cos\left(\theta - \frac{2\pi}{3}\right) & 1 \\ \sin\left(\theta + \frac{2\pi}{3}\right) & \cos\left(\theta + \frac{2\pi}{3}\right) & 1 \end{bmatrix} \begin{bmatrix} V_\alpha \\ V_\beta \\ 0 \end{bmatrix} \text{ [35]} \tag{3.4}$$

Another frame of transformation is the Park transformation, which converts the stationary (α, β) frame into a rotating (d, q) frame aligned with the rotor flux or stator voltage . This transformation simplifies control by converting sinusoidal signals into steady-state DC values, making PI controller design more straightforward . Introduced by Robert H. Park in the 1920s, it transforms three-phase abc signals into $dq0$ components while preserving both active and reactive power [6, 54].

The transformation from three-phase voltages V_{abc} to the direct-quadrature-zero components V_{dq0} is given by :

$$V_{dq0} = T_{dq0}(\theta) \cdot V_{abc} \text{[50]} \tag{3.5}$$

✓ For Un-balanced system

$$[V_d, V_q, V_0] = \frac{2}{3} \begin{pmatrix} \sin(\theta) & \sin\left(\theta - \frac{2\pi}{3}\right) & \sin\left(\theta + \frac{2\pi}{3}\right) \\ \cos(\theta) & \cos\left(\theta - \frac{2\pi}{3}\right) & \cos\left(\theta + \frac{2\pi}{3}\right) \\ \frac{1}{2} & \frac{1}{2} & \frac{1}{2} \end{pmatrix} [V_a, V_b, V_c] \text{ [52]} \tag{3.6}$$

The inverse Park transformation from V_{dq0} to V_{abc} can be expressed as:

$$V_{abc} = T^{-1}_{dq0}(\theta)\, V_{dq0} \tag{3.7}$$

$$\begin{bmatrix} V_a \\ V_b \\ V_c \end{bmatrix} = \begin{bmatrix} \sin(\theta) & \cos(\theta) & 1 \\ \sin\left(\theta - \frac{2\pi}{3}\right) & \cos\left(\theta - \frac{2\pi}{3}\right) & 1 \\ \sin\left(\theta + \frac{2\pi}{3}\right) & \cos\left(\theta + \frac{2\pi}{3}\right) & 1 \end{bmatrix} \begin{bmatrix} V_d \\ V_q \\ V_0 \end{bmatrix} \text{ [53]} \tag{3.8}$$

✓ For a balanced system, the zero component is equal to zero. The transformation from the three-phase voltages $[V_a, V_b, V_c]$ to the dq0 components $[V_d, V_q, V_0]$ can be expressed as:

$$\begin{bmatrix} V_d, V_q, V_0 \end{bmatrix} = \frac{2}{3} \begin{bmatrix} \sin(\theta) & \sin\left(\theta - \frac{2\pi}{3}\right) & \sin\left(\theta + \frac{2\pi}{3}\right) \\ \cos(\theta) & \cos\left(\theta - \frac{2\pi}{3}\right) & \cos\left(\theta + \frac{2\pi}{3}\right) \end{bmatrix} \begin{bmatrix} V_a, V_b, V_c \end{bmatrix} \text{ [50]} \tag{3.9}$$

We can also use park transformation when 2-axis quantities of an orthogonal reference frame are transformed into 2-axis quantities of a rotating frame quantities presented in 3.10 and 3.11 .

$$\begin{pmatrix} i_d \\ i_q \end{pmatrix} = \begin{pmatrix} \cos(\theta) \cdot i_\alpha + \sin(\theta) \cdot i_\beta \\ -\sin(\theta) \cdot i_\alpha + \cos(\theta) \cdot i_\beta \end{pmatrix} \tag{3.10}$$

To convert from the rotating dq frame back to the stationary $\alpha\beta$ frame [49]:

$$\begin{pmatrix} V_\alpha \\ V_\beta \end{pmatrix} = \begin{pmatrix} \cos(\theta) & -\sin(\theta) \\ \cos(\theta) & \sin(\theta) \end{pmatrix} \begin{pmatrix} V_d \\ V_q \end{pmatrix} \tag{3.11}$$

3.2 Dynamic Modelling of IPMSM

The IPMSM is considered highly suitable for automotive applications due to its excellent efficiency, high power density, favorable torque-per-current characteristics, and wide operational speed range [59, 60] . To accurately analyze and predict the motor's performance under varying conditions, it is essential to establish a mathematical model that describes both the electrical and mechanical dynamics of the IPMSM, as illustrated in Figure 3.3 . The IPMSM is a popular choice for applications that require high efficiency ,precise control and power density [8, 51, 44] .

In the context of modeling IPMSM Drives for railway inverter drives figure 3.2 illustrates the configuration of a three-phase, 2-pole IPMSM and represents the orientation of the motor windings and permanent magnets in the motor's internal structure . Key Points for the Model of the Three-Phase, Two-Pole IPMSM (d-q Axis Model) :

✓ Neglecting saturation effects

✓ Assuming the induced EMF is sinusoidal

✓ Ignoring hysteresis and eddy current losses

✓ No dynamics in the field current

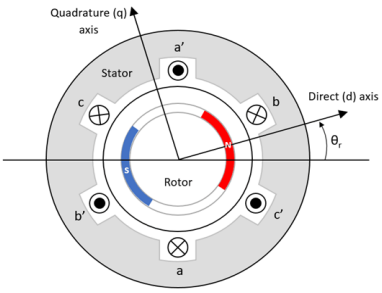

Figure 3.2: Three-phase 2-pole IPMSM d-q-axis [6]

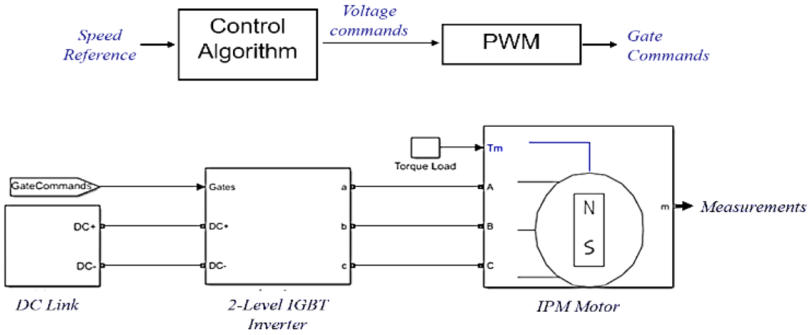

Figure 3.3: Block diagram of the system [7, 8]

3.2.1 Electrical Model

For a PMSM, the electrical model can be described in terms of Park's equations, which are commonly used to represent the motor's behavior in a coordinate system rotating synchronously with the rotor [60].

The equivalent circuit model of an embedded permanent magnet synchronous machine in the rotor d-q reference frame is shown in figure 3.4 [9, 7] .

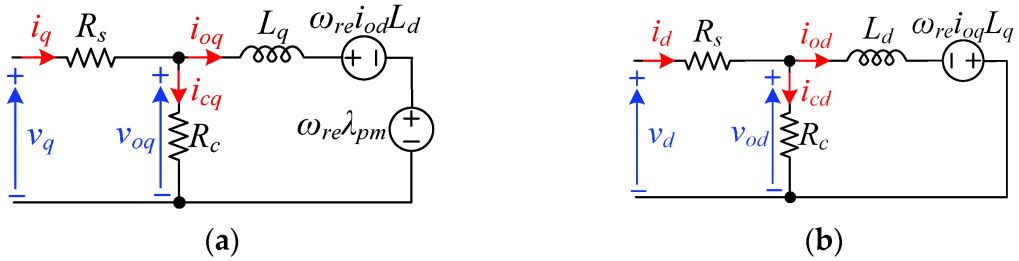

Figure 3.4: Dynamic equivalent circuit of the IPMSM machine: (a) q-axis and (b) d-axis [9].

a. Voltage equations are given by:

$$\begin{cases} V_d = i_d R_s + \frac{d\lambda_d}{dt} - \omega_e \lambda_q \\ V_q = i_q R_s + \frac{d\lambda_q}{dt} + \omega_e \lambda_d \end{cases} \quad [7] \tag{3.12}$$

b. Flux linkage equations are given by:

$$\begin{cases} \lambda_d = L_d i_d + \lambda_m \\ \lambda_q = L_q i_q \end{cases} \quad [61] \tag{3.13}$$

By substituting Equations 3.13 into 3.12, we get:

$$\begin{bmatrix} v_d \\ v_q \end{bmatrix} = \begin{bmatrix} r_s & -\omega_e L_q \\ \omega_e L_d & r_s \end{bmatrix} \begin{bmatrix} i_d \\ i_q \end{bmatrix} + \begin{bmatrix} L_d & 0 \\ 0 & L_q \end{bmatrix} \begin{bmatrix} \frac{di_d}{dt} \\ \frac{di_q}{dt} \end{bmatrix} + \begin{bmatrix} 0 \\ \omega_e \lambda_m \end{bmatrix} [23] \tag{3.14}$$

c. Current equations are obtained by integrating 3.14 after rearrange :

$$i_{sd} = \int \frac{1}{L_d} \left(V_d - i_d r_s + \omega_e L_q i_q \right) \, dt \tag{3.15}$$

$$i_{sq} = \int \frac{1}{L_q} \left(V_q - \omega_e L_d i_d - \omega_e \lambda_m \right) \, dt \tag{3.16}$$

where:

- ✓ V_d, V_q : d-axis and q-axis voltages [V],
- ✓ i_d, i_q : d-axis and q-axis currents [A],
- ✓ R_s : stator resistance (Ω),
- ✓ L_d, L_q : d-axis and q-axis inductances [H],
- ✓ λ_d, λ_q: d-axis and q-axis flux linkages [Wb],
- ✓ λ_m : permanent magnet flux linkage [Wb],
- ✓ ω_e : electrical angular velocity [rad/s].

3.2.2 Mechanical Model

Equations representing the mechanical aspects of the IPMSM, such as torque, speed, and inertia. The rotational dynamic equation of a IPMSM is obtained from the equations of rotational motion. The electromagnetic torque developed by an IPMSM expressed in 3.19 is given by the sum of magnetic torque and reluctance torque components [61, 20] :

$$T_e = \underbrace{\frac{3}{2} n_p \lambda_m i_q}_{\text{Magnetic Torque}} + \underbrace{\frac{3}{2} n_p (L_d - L_q) i_d i_q}_{\text{Reluctance Torque}} [62] \tag{3.17}$$

a. For a non-salient rotor (in surface-mounted Permanent Magnet Synchronous Motors, or

PMSMs), the direct and quadrature axis inductance are the same, i.e., $L_d = L_q$, meaning the rotor has the same reluctance in both axes, the produced torque T_e is given by [62]:

$$T_e = \frac{3}{2} n_p \lambda_m i_q \tag{3.18}$$

b. For salient Rotor (in IPMSM due to the asymmetry in flux path inductances are different. i.e.). The presence of reluctance torque increases the power density of the motor. $L_d \neq L_q$, with the different reluctance and the produced torque is given by

$$T_e = \frac{3}{2} n_p \left(\lambda_m i_q + (L_d - L_q) i_d i_q\right) \tag{3.19}$$

The mechanical torque equation is given by:

$$T_e = T_l + k_f \omega_r + J_d \frac{d\omega_r}{dt} \tag{3.20}$$

Solving for the rotor mechanical speed from 3.20 and 3.19 ω_r can be expressed as the integral of torque over time [63]:

$$\omega_r = \int \left(\frac{T_e - T_l - k_f \omega_r}{J_d} \right) dt$$

The electrical frequency ω_e is given by:

$$\omega_e = \frac{n_p}{2} \omega_r \tag{3.21}$$

The electrical angle θ_e is given by:

$$\theta_e = \frac{n_p}{2} \int \omega_r \, dt \tag{3.22}$$

Where:

- ✓ L_d and L_q: Direct and quadrature inductances [H]
- ✓ T_l: Load torque [Nm]
- ✓ T_e: Electrical torque [Nm]
- ✓ J: Moment of inertia of the motor and load [kg·m²]
- ✓ k_f: Friction coefficient of the motor [N·m·s/rad]
- ✓ ω_r: Rotor angular speed [rad/s]
- ✓ n_p: Number of pole pairs of the motor
- ✓ $\omega_e : n_p \cdot \omega_r$: Electric angular speed [rad/s]

3.3 Control Strategies of IPMSM Drive System

To operate at varying speeds, synchronous motors require a Variable Frequency Drive (VFD) for effective control [39]. Traction Electric motor control methods can be divided into two main

categories depending of what quantities they control. Over time, numerous control techniques have been devised to govern the operation of PMSMs [64].

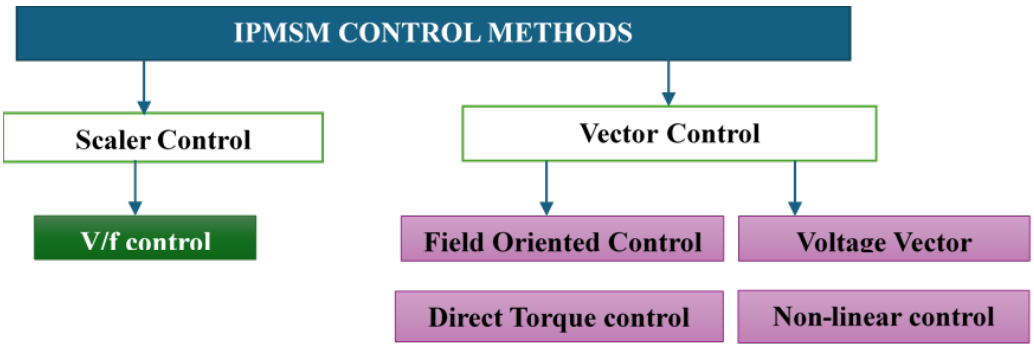

Figure 3.5: A block diagram illustrating the key control methods implemented for IPMSMs.

3.3.1 Speed Control of IPMSM

The purpose of a motor speed controller is to receive a signal representing the desired speed and regulate the motor to operate at that speed. Closed-loop speed control systems offer fast response but are generally more expensive due to the requirement for feedback components, such as speed sensors. With a speed control system, a motor's speed can be accurately controlled and adjusted. Such a system typically consists of the motor, an inverter, a controller, a speed-setting device, and a speed feedback mechanism.

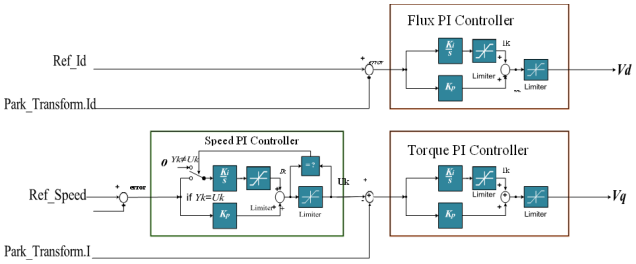

Figure 3.6: PI Controller [10].

The PI regulator as shown figure 3.6 keeps the output following the expected output by comparing the error between the expected output and the real output, and the I-value is used to decrease the steady-state output error. Its transfer function can be expressed as follows [65]:

$$G(s) = K_p + \frac{K_i}{s}$$

$$f(t) = K_p e(t) + K_i \int_0^t e(\tau)\, d\tau \tag{3.23}$$

where K_p is the proportional gain and K_i is the integral gain.The PI regulator causes a fluctuating output, with the amplitude of the fluctuations decreasing over time.

3.3.2 Field-oriented Control (FOC) or Vector Control (VC)

Field-oriented control, also known as vector control, is a method of controlling the speed and torque of a permanent magnet synchronous motor (PMSM) by using a mathematical model of the motor to calculate the appropriate control signals [66].

The goal of FOC is to control the direct-axis current (i_d) and quadrature-axis current (i_q) to achieve the required torque [67, 20]. By controlling i_d and i_q independently, the MTPA strategy can be implemented to minimize the current required for a given torque, thereby improving motor efficiency. For a non-salient machine (SPMSM), this control method is straightforward because $L_d = L_q$ and the motor produces only electromechanical torque. In contrast, for a salient-pole machine (IPMSM), where $L_d \neq L_q$, the control is more complex since the motor generates both electromechanical and reluctance torque [68].

The core principle of the vector control algorithm is to separate the stator current into a magnetic field-producing component and a torque-producing component, allowing each to be controlled independently. The system consists of (i.e., Figure 3.9) speed, d and q axes current PI regulators, Park and Clarke transformations, inverse Park transformation, space vector generation, speed calculation , current and encoder signal conditioning and PWM generator modules [8, 20] . Figure 3.9, illustrates how the control system receives the desired speed of the motor as input. The speed measurement is used to feed a speed regulator with the discrepancy between the motor's real speed and reference speed. Te a torque command, is the regulator's output . Drawing from this torque command, one of the control techniques shows the reference currents, i^*_{sd} and i^*_{sq} [54, 68].

In the control of an IPMSM, both torque and flux are indirectly regulated through d-q axis current control. The control strategy is based on the FOC framework, enhanced by the Maximum Torque Per Ampere (MTPA) algorithm . The error between the reference dq currents, chosen by the MTPA algorithm and the measured dq currents fed to the current regulators . The output of the current regulators are the corresponding dq reference stator voltages . Based on these stator voltages SVPWM and SPWM are used to control the switches of the inverter.

There are different ways to relate the torque references to the d-q currents on basis of the secondary requirements explained in the beginning of this chapter [69].

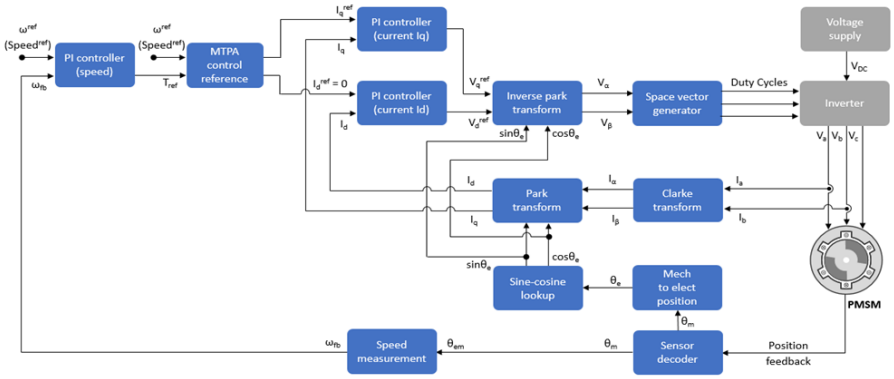

Figure 3.7: Field-Oriented Vector Control Scheme with Sensor Information [11].

3.3.2.1 Zero d-Current Control

Figure 3.9 illustrates a straight forward approach to controlling a PMSM by setting the d-current to zero .This simplifies torque control depend solely on the q-current, making the system easier to manage .The current components in the d-q-frame are shown 3.24 .

$$\begin{cases} I_d = \frac{2}{3}\left(I_a\cos(\theta) + I_b\cos\left(\theta - \frac{2\pi}{3}\right) + I_c\cos\left(\theta + \frac{2\pi}{3}\right)\right) \\ I_q = \frac{2}{3}\left(I_a\sin(\theta) + I_b\sin\left(\theta - \frac{2\pi}{3}\right) + I_c\sin\left(\theta + \frac{2\pi}{3}\right)\right) \end{cases} \quad [70] \tag{3.24}$$

Where θ is the rotor angle and I_a, I_b, I_c are the phase currents . By enforcing $I_d = 0$, Zero d-current control will:

- ✓ Maximizes torque production by fully utilizing the q-axis current.
- ✓ Reduces torque ripple and improves motor smoothness.
- ✓ Enhances efficiency by minimizing losses in the d-axis.

This strategy is particularly effective in IPMSM, where the rotor's permanent magnet flux requires careful management of the d- and q-axis currents for optimal performance .

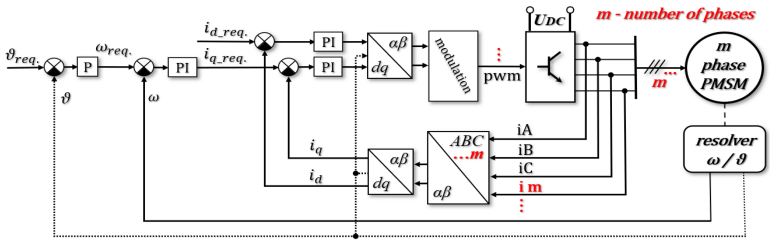

Figure 3.8: Zero d-current control strategy for number of phases [6].

When we simplify the torque (3.19) from subsection 3.2.2 and set the d-current to zero, according to [70], this simplification transforms the torque equation into :

$$T_e = \frac{3}{2} n_p \lambda_m i_q \tag{3.25}$$

So the current references will written as :

$$i_d^{ref} = 0 \tag{3.26}$$

$$i_q^{ref} = \frac{2}{3}\frac{T_e}{n_p \lambda_m} \tag{3.27}$$

3.3.2.2 Maximum Torque per Ampere Control (MTPA)

A technique for managing IPMSMs with high efficiency . It involves adjusting the current vector to maximize the torque produced in relation to the current ampere . This minimizes

current-dependent losses like copper loss and allows for high-efficiency operation [69] .

$$i_{d\_MTPA} = \frac{-\lambda_m + \sqrt{\lambda_m^2 + (4L_1 i_q)^2}}{4L_1} \tag{3.28}$$

Where , the permanent magnet flux linkage and differential inductance are :

$$\phi_{pm} = \lambda_m \tag{3.29}$$

$$L_1 = \frac{L_q - L_d}{2} \tag{3.30}$$

Alternatively, the starting point for obtaining the MTPA curve of the IPMSM is the electromagnetic torque equation of the machine [**?**].

$$T_e = \frac{3}{2} n_p \left(\lambda_m i_q + (L_d - L_q) i_d i_q\right) \tag{3.31}$$

In addition to this equation, another constraint must be added the stator current limitation resulting from the inverter's physical current limitation .

$$I_{s_{max}}^2 = I_{s_d}^2 + I_{s_q}^2 \tag{3.32}$$

$I_{s_{max}}^2$ is the maximum amplitude of the current which is supported by the inverter If is depicted from 3.31 and substituted into the torque equation the following expression is obtained from 3.33, the minimum I_{s_d} current that satisfies the torque equation is found as [20] .

$$i_{ds} = \frac{-\lambda_m + \sqrt{\lambda_m^2 + 8(L_d - L_q)^2 (I_{s_{max}})^2}}{4(L_d - L_q)} \tag{3.33}$$

$$T_e = \frac{3}{2} n_p \left[\lambda_m \sqrt{I_{s_{max}}^2 - Is_d^2} + (L_d - L_q) I_d \sqrt{I_{s_{max}}^2 - Is_d^2}\right] \tag{3.34}$$

MTPA operation is required to control the IPMSM . Lots of papers have suggested control methods for the MTPA operation [71, 72, 73] .The control block diagram is shown in Figure 3.9 .

The d-axis current $I_{d,\text{ref}}$ and q-axis current $I_{q,\text{ref}}$ are determined based on the MTPA tables according to the reference flux λ_{ref} and reference torque T_{ref}, respectively . D-axis current compensation ($I_{d,\text{comp}}$) is used to remove the flux error . The rationale behind this simplification is that switching frequency fluctuations (f_{sw}) mostly impact the low-speed range, where MTPA operation is crucial .

In the context of an IPMSM, coordinate transformation is used in Field-Oriented Control (FOC) to simplify the control of the motor by decoupling the control variables . The two commonly used coordinate transformations in IPMSM control are the Clarke transformation and the Park transformation .

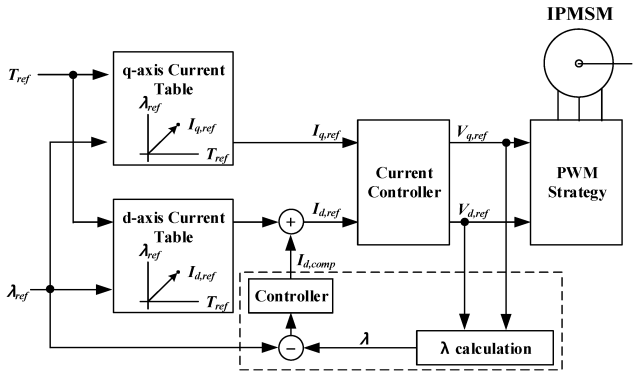

Figure 3.9: Control block diagram for driving the IPMSM [6].

3.3.2.3 Decoupling Approaches

In the vector control of IPMSM, the d and q axis voltages are interdependent due to cross-coupling terms such as $\omega_r L_q i_q$ and $\omega_r(L_d i_d + \lambda_m)$. These couplings decrease controller performance and dynamic response if not compensated.

Decoupling techniques are employed in FOC to separate the control of torque and flux in IPMS motors . This is crucial for achieving precise and efficient control of the motor . There are two commonly used decoupling methods indirect decoupling and direct decoupling in which Figure 3.10 illustrate the direct decoupling method of FOC techniques . By applying this transformation, the control system can independently control the torque and flux without affecting each other . In this thesis, the direct decoupling method is used [74].

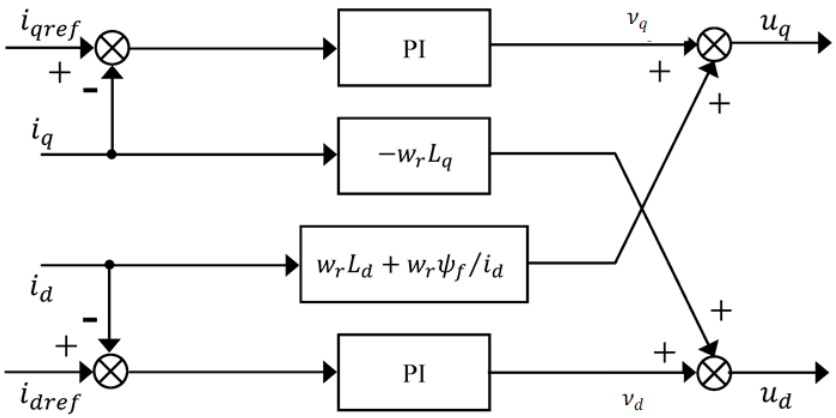

Figure 3.10: Structure of direct decoupled current regulator design of FOC techniques .

Chapter 4

Loss Calculations for Semiconductor Devices in Three-Phase Inverters

This chapter delves into power loss modeling for SiC-MOSFETs, IGBTs, and diodes, as well as their relevance to railway traction systems . Analytical models for conduction and switching losses with SPWM and SVPWM . Additionally, thermal design considerations are presented to ensure reliable operation under varying load and environmental conditions.

4.1 Introduction

Semiconductor losses , conduction and switching losses significantly affect the efficiency and performance of three-phase inverters. As the demand for higher efficiency and power density increases, particularly in electric vehicles industrial systems and railway systems, minimizing these losses becomes essential [75, 7] . Therefore, this section analyzes the impact of two widely used PWM strategies, SPWM and SVPWM, on semiconductor losses in three-phase inverters [56]. By evaluating devices such as SiC-MOSFETs, IGBTs, and diodes, the goal is to identify the most effective approach for reducing losses, improving efficiency, and enhancing the reliability of traction drive systems [46].

4.2 The Significance of Power Loss Calculation

To maximize the efficiency, dependability, and performance of traction inverters in railway vehicles, precise power loss estimation is essential for semiconductor devices .Thus, selecting the thermal management strategy and the prediction of inverter efficiency is greatly aided by estimating the device loss [76] . The power loss of the inverter and the thermal management system can be computed when a certain semiconductor device is selected using information from the device data-sheets and the inverter's operating conditions. It is necessary to include both switching power losses and conduction power losses [41] . This computation technique is applicable to widely used semiconductor devices, such as diodes, IGBTs, and SiC-MOSFETs . The conduction and switching power losses can be calculated by using datasheet information on on-state resistance and switching energy losses .

In railway traction systems, the losses incurred within the inverter system have a significant impact on overall efficiency and performance . The entire efficiency and performance of railway traction systems, whether they are powered by induction motors, IPMSM, SPMSM, or other

forms of electric propulsion, are greatly impacted by power losses . Here's how these losses affect different aspects of railway traction systems [77] .

a. **Cost-Effectiveness** : Due to higher energy consumption and increased maintenance needs, inverter power losses increase operating expenses. Costs associated with inefficient systems may increase due to the necessity for larger cooling systems and more capable thermal management techniques. Moreover, increased losses could necessitate the use of larger, more costly components, affecting overall cost-effectiveness [43].

b. **Efficiency** : Inverter power losses lead to energy dissipation, which reduces the overall efficiency of energy conversion and increases energy consumption. This is critical as higher losses directly correlate with lower system efficiency [20].

c. **Performance** : Excessive inverter power losses can adversely affect the performance characteristics of the traction system . Lower efficiency due to these losses may limit torque production and power output, impacting the system's ability to accelerate, decelerate, and maintain desired speeds . Additionally, power losses can affect the dynamic response and speed regulation, potentially compromising overall performance .

d. **Reliability** : High inverter power losses generate heat, leading to thermal challenges and potential component degradation . Components such as semiconductor devices may experience elevated temperatures, which can reduce their reliability and lifespan. Effective thermal management strategies are crucial to mitigate these reliability concerns [78].

Therefore, a study of inverter loss and identification of causes of inverter loss is essential for improved performance . It also gives insight towards a means of loss minimization strategy .

4.3 Conduction Loss Modeling in SPWM

For the railway traction drive system, the field-oriented control algorithm (FOC) is widely adopted due to the high efficiency and torque control accuracy, and the voltage and current signals in the two-phase synchronous rotating coordinate need to be filtered [62]. This section focuses on the modeling of conduction losses under SPWM, which is one of the most commonly used modulation techniques in railway traction inverters. With an emphasis on SiC-MOSFETs, IGBTs, and Diodes used in railway traction inverters, we examine how accurate the developed model is [79] . Therefore, power losses are made up of various discrete loss components. The projected power dissipation in the switching component is primarily determined by the switching losses (turn-on, turn-off, and reverse recovery losses) and static on-state (conduction) losses; while components like driving and blocking losses are typically ignored [80]. A full numerical simulation of the circuit is one option. This makes it possible to get comprehensive data regarding efficiency as well as, for instance, researching the impact of parasitic elements [81].

In the following subsections, we first review the analytical calculation of conduction losses . Subsequently, the approach to assessing switching losses is described . Afterward, the developed

model is evaluated by calculating the power loss and efficiency of the drive system . Finally, the result is compared to an online simulation tool [82].

In SPWM-based three-phase inverters, a sinusoidal control voltage is compared with a triangular carrier wave to create a PWM signal to generate phase voltages (V_m) [83] . Specifically, the three-phase sinusoidal voltage signals from the current controller are compared to a higher frequency triangular wave . When the sinusoidal signal exceeds the triangular wave,V_m is ($\frac{V_{dc}}{2}$), otherwise it is ($-\frac{V_{dc}}{2}$) . This technique results in phase voltage and phase current waveforms, illustrated in Chapter two and Chapter three .

Time intervals in the switching period are related to the control algorithm, thus they are acquired depending on different PWM techniques . This image makes it evident that a sinusoidal period consists of six operational modes . Based on various PWM approaches and operating modes, the analysis and derivation of the time intervals in the switching period are presented .

Figure 4.1 illustrates the relationship between the modulation and carrier signals, and shows how the phase A modulation signal and the carrier signal are moved up by (V_C) for ease of calculation . By interpreting the peak value of the modulation signal in the form of ($M \cdot V_C$), where (V_C) denotes the peak value of the carrier signal and M is modulation index . The phase voltages in SPWM can be expressed as :

$$V_a = M \cdot V_C \left(\sin(\omega t) + V_0\right) \tag{4.1}$$

$$V_b = M \cdot V_C \left(\sin\left(\omega t - \frac{2\pi}{3}\right) + V_0\right) \tag{4.2}$$

$$V_c = M \cdot V_C \left(\sin\left(\omega t + \frac{2\pi}{3}\right) + V_0\right) \tag{4.3}$$

$$V_0 = \begin{cases} 0, & \text{for SPWM} \\ \dfrac{1}{6}\sin(3\omega t), & \text{for THIPWM} \\ -\dfrac{1}{2}(V_{\max} + V_{\min}), & \text{for SVPWM} \end{cases} \tag{4.4}$$

where:

- ✓ v_0 is the zero-sequence voltage component.
- ✓ $\omega = 2\pi f$ is the angular frequency of the fundamental waveform, with f being the frequency in hertz (Hz).
- ✓ $\sin(3\omega t)$ is the third harmonic component injected in THIPWM.
- ✓ $V_{\max}$ and $V_{\min}$ are the maximum and minimum instantaneous 3-phase reference voltages, respectively .
- ✓ THIPWM, Third Harmonic Injection PWM .

Figure 4.1 shows the inverter modulation signals, including the carrier waveform, the phase A modulation signal for SPWM, and the corresponding zero-sequence component v_0.

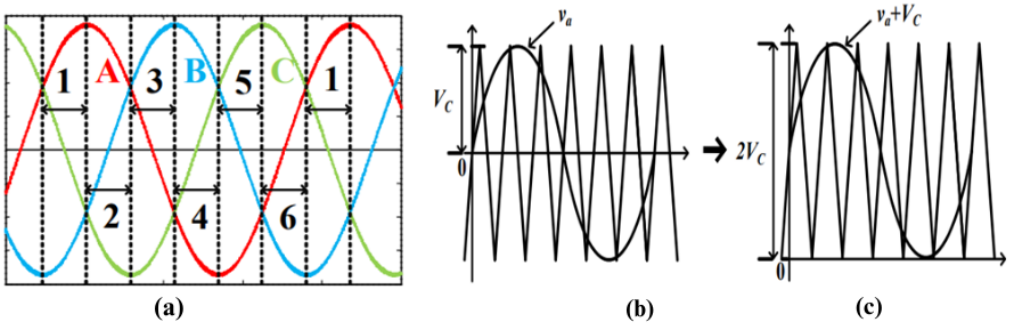

Figure 4.1: Modulation signal processing in three-phase systems (a) Three-phase sinusoidal reference signals with 60° phase shifts and corresponding sector identification, (b) Phase A modulation signal v_a compared with triangular carrier V_C, and (c) waveform after zero-sequence voltage injection showing $v_a + V_C$ [12].

The SPWM works in a principle that when the value of the modulation signal is higher than that of the carrier signal, the upper switch in the corresponding phase is on ; in contrast, if the value of the carrier signal is higher, the lower switch is on instead. The modulation and carrier signals within the switching period T_{sw} are shown in figure 4.2, and the duty cycle of each switch is defined by T_0, T_1, T_2, and T_3 . By solving the geometric problems presented in Figure 4.2a, the correlation between T_1, T_2, T_3, and T_{sw} can be interpreted by 4.5 to 4.6 and after a simple analysis one can easily get then we will get 4.46 [84].

$$\frac{2T_3}{T_{sw}} = \frac{V_b + V_c}{2V_c}$$
$$\frac{2T_2 + 2T_3}{T_{sw}} = \frac{V_b + V_c}{2V_c}$$

$$2T_0 = T_{sw} - (2T_1 + 2T_2 + 2T_3) \tag{4.5}$$

where:

- ✓ T_0 is the time duration for the zero state,
- ✓ T_1, T_2, and T_3 are the time durations for the respective active states,
- ✓ T_s or T_{sw} is the total switching period.

The duty ratio of the switch can be obtained by comparing the modulation signal with the carrier signal; and the current flowing through the switch can be represented by the duty ratio and the output current. According to figure 4.4, the upper phase switch is turned on when the value of the modulation signal from phase A is higher than the value of the carrier signal, and the duty cycle D of the upper phase A switch is derived in [14].

$$D(t) = \frac{T_{sw}}{T_a} = \frac{v_a + V_c}{2V_c} = \frac{MV_c \sin(\omega t) + V_c}{2V_c} = \frac{1}{2}\left(1 + M\sin(\omega t + \phi)\right) \tag{4.6}$$

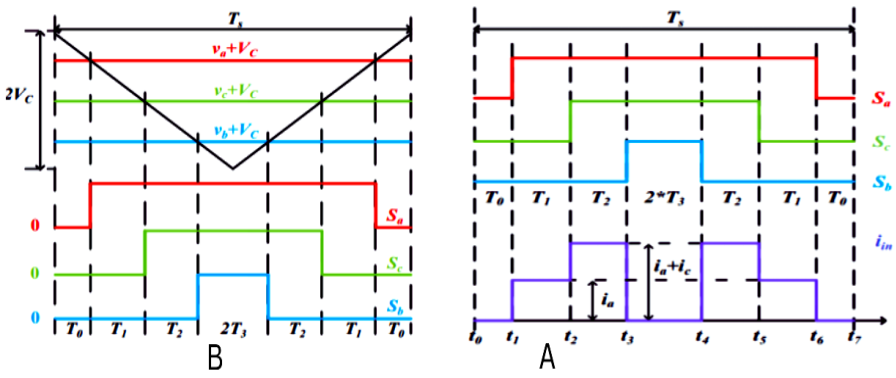

Figure 4.2: (A).Switching Functions with Modulation and Carrier Signals (B). Ideal Inverter Input Current.

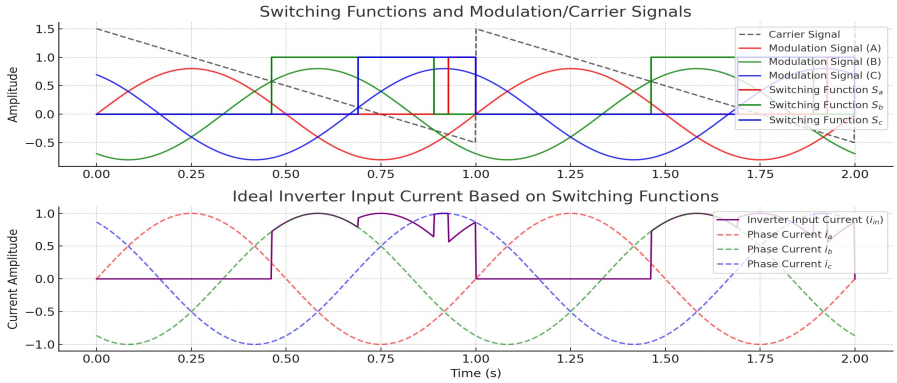

Figure 4.3: Switching Functions with Modulation and Carrier Signals, and Ideal Inverter Input Current in PLECS.

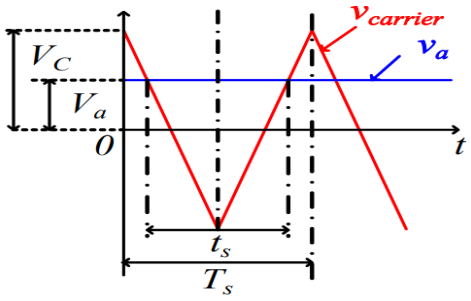

Figure 4.4: Curves of the carrier and phase A modulation signal in T_{sw}.

During the period T_{sw}, when the current i_a is positive and switch T_1 is on, the current flows through T_1 [85].

4.3.1 IGBT Conduction Loss

The conduction loss of an IGBT occur when it is conducting. The average power dissipation during conduction can be obtained by integrating the product of voltage drop over the device and current flowing through it for half of the fundamental period T_0 , because of the symmetry

of sinusoidal. As stated in [66], the conduction power loss $P_{\text{IGBT cond}}$ can be expressed as

$$P_{\text{IGBT,cond}} = \frac{1}{NT_{sw}} \sum_{n=1}^{N} \int_{(n-1)T_{sw}}^{(n-1+D_n)T_{sw}} V_{CE} \times i(t)\, dt \tag{4.7}$$

In 4.7, N is the number of switching periods, T_{sw} is the switching period, D_n is the duty cycle in the n-th switching period, V_{CE} is the collector-emitter voltage, and $i(t)$ is the instantaneous current flowing through the IGBT during its conduction interval. where the collector-emitter voltage V_{CE} is modeled by

$$V_{CE} = V_{CE0} + R_{ce} \times i(t) \tag{4.8}$$

By substituting 4.8 into the instantaneous power expressed in 4.7 , the conduction power loss over N switching periods is computed as:

$$P_{\text{IGBT cond}} = \frac{1}{NT_{sw}} \sum_{n=1}^{N} \int_{(n-1)T_{sw}}^{(n-1+D_n)T_{sw}} (V_{ce0} + R_{ce} i(nT_{sw}))\, D_n T_{sw}\, dt \tag{4.9}$$

The parameter V_{CE0} corresponds to the forward voltage drop of the IGBT, while R_{ce} is the device's on-state resistance. The instantaneous current through the device is represented by $i(t)$, and $i(nT_{sw})$ is the current sampled at the beginning of the n-th switching period.
The phase-current period is assumed to be much longer than the switching period, which allows the number of switching cycles N in 4.9 as infinity.

In this case, the phase current in the nth switching period, denoted $(i(nT_{sw}))$, can be represented using the time derivative with respect to the switching time (T_{sw}) With a series connection of a DC voltage source V_{ce0} that reflects the voltage of the collector-emitter transistor in the state zero current and the resistance of the collector-emitter in the state R_{ce}, the transistor conduction voltage $V_{ce}(t)$ in figure 4.5 can be expressed as 4.8.
Equation 4.9 introduces the duty cycle (D (t)), which is a key parameter for calculating conduction loss. The duty cycle is influenced by the modulation mode and is a variable parameter that needs to be solved. By substituting 4.8 in 4.9 the conduction losses can be re-written as

$$P_{\text{IGBT cond}} = \frac{1}{2\pi} \int_{0}^{2\pi} (V_{ce0} + R_{ce} i(t))\, i(t) \times \frac{1}{2} (1 + M \sin(\omega t + \phi))\, dt \tag{4.10}$$

Since the parameters (V_{ce0}, R_{ce}, V_f, and R_f) of IGBTs and FWDs are temperature-dependent, they are measured based on the device datasheet at different temperatures.According to the FOC algorithm, the phase-current has a sinusoidal structure. The current can be stated as 4.11 , assuming that the phase angle of the phase current is θ:

$$i(\theta) = i_\alpha = I_p \cos(\theta) \tag{4.11}$$

where I_p is the amplitude of the phase current.

Since the PMSM is an inductive load, there is a phase angle difference between the voltage

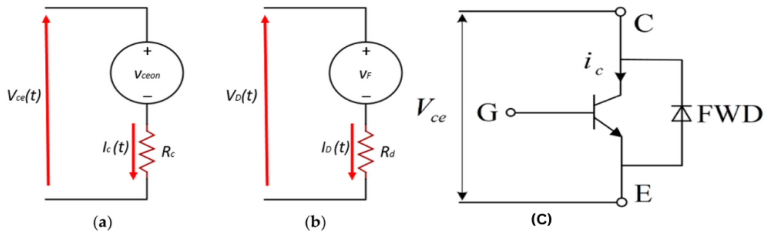

Figure 4.5: Equivalent circuits of IGBT and freewheeling diode for conduction loss analysis (a) IGBT model with V_{ceon} and R_ce, (b) Diode model with V_F and R_d, (c) IGBT with anti-parallel diode showing terminals and current path [13].

vector and the current vector. This angle is referred to as the power factor angle and can be expressed as:

$$\alpha = \theta + \phi \tag{4.12}$$

Inserting 4.11 and 4.12 in to 4.10 will give as

$$P_{\text{IGBT cond}} = \frac{1}{2\pi}\int_0^{2\pi} (V_{ce0} + R_{ce} i(t) I_p \cos(\theta)) \cdot \frac{1}{2}(1 + M\sin(\omega t + \phi))\, dt \tag{4.13}$$

Therefore, the integration of the steady-state representation of the IGBT conduction loss becomes 4.14.

$$P_{\text{cond\_IGBT}} = \frac{1}{2\pi} V_{CE0}(T) I_p + \left(\frac{1}{8} + \frac{1}{3\pi}\right) R_{CE}(T) I_p^2 - \frac{1}{8} M\cos(\phi) V_{CE0}(T) I_p \tag{4.14}$$

The parameters $V_{ce0}(T)$ and $R_{ce}(T)$ represent the temperature-dependent collector-emitter voltage drop at zero current and the on-state resistance of the IGBT, respectively. For accurate loss modeling, the values at the operating junction temperature T are obtained by linear interpolation between these reference points as figure 4.6 :

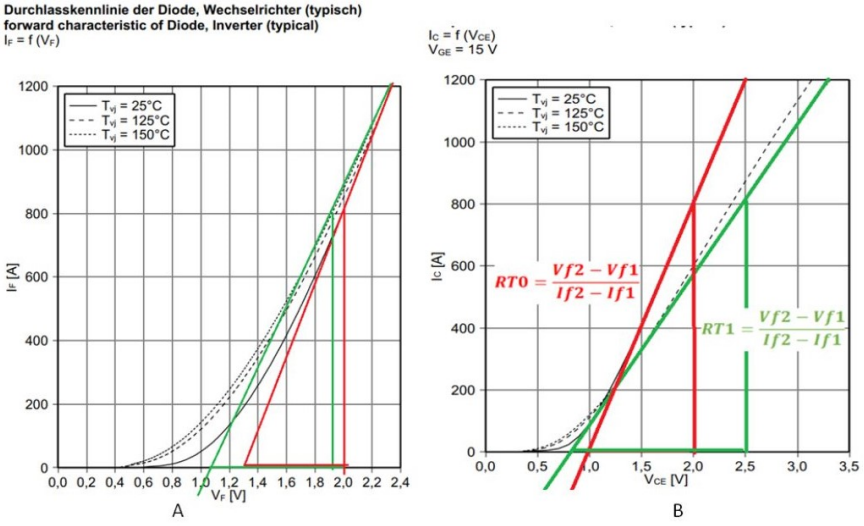

Figure 4.6: Linear interpolation of IGBT and diode parameters.

$$Vce0(T) = \frac{Vceo(2) * T_{max} - Vceo(1) * T_{min}}{T_{max} - T_{min}} + \frac{Vceo(2) - Vceo(1)}{T_{max} - T_{min}} * T_j \tag{4.15}$$

$$Rce0(T) = \frac{Rce(2) \cdot T_{max} - Rce(1) \cdot T_{min}}{T_{max} - T_{min}} + \frac{Rce(2) - Rce(1)}{T_{max} - T_{min}} * T_j \tag{4.16}$$

Where $V_{ce0}(1)$ and $R_{ce}(1)$ are the collector-emitter voltage drop and on-state resistance of the IGBT at the minimum junction temperature $T_{\min}$, and $V_{ce0}(2)$ and $R_{ce}(2)$ are the corresponding values at the maximum junction temperature $T_{\max}$ [15].

The linear functions of the junction temperature are obtained based on the reference values at temperatures T_{min} (℃) and T_{max} (℃), shown in 4.15 and 4.16, and the parameters can be calculated according to the real-time junction temperature [13].

4.3.2 Diode Conduction Loss

A diode can be modeled as a resistor in series with a voltage source. Consequently, the conduction loss equation of the diode is similar to that of the IGBT and can be expressed using 4.17 and 4.10, resulting in 4.18.

The conduction voltage across the diode can be calculated using the same approach, based on the equivalent circuit shown in Figure 4.5, leading to the following expression:

$$V_D(t) = V_f + R_d \cdot i_D(t) \tag{4.17}$$

$$P_{\text{Diode\_cond}} = \frac{1}{2\pi} V_f(T) I_p + \frac{1}{8} R_f(T) I_p^2 + \frac{1}{8} M \cos(\phi) V_f(T) I_p + \frac{1}{3\pi} R_f(T) I_p^2 \tag{4.18}$$

The values V_f and R_f can be obtained from the forward characteristics of the diode as specified in its datasheet [67] . The total inverter power losses can be calculated accordingly, as shown in 4.10 to 4.18 as stated in [66].

$$V_{f0}(T) = \frac{V_f(2) \cdot T_{\max} - V_f(1) \cdot T_{\min}}{T_{\max} - T_{\min}} + \frac{V_f(2) - V_f(1)}{T_{\max} - T_{\min}} * T_j \tag{4.19}$$

$$R_f(T) = \frac{R_f(2) \cdot T_{\max} - R_f(1) \cdot T_{\min}}{T_{\max} - T_{\min}} + \frac{R_f(2) - R_f(1)}{T_{\max} - T_{\min}} * T_j \tag{4.20}$$

The values of V_{f0} and R_f are calculated for two forward current levels I_{f1} and I_{f2} at a given junction temperature . Thus, we can write :

$$R_f(\text{Tj}) = \frac{\Delta V_f}{\Delta I_f} = \frac{V_f(2) - V_f(1)}{I_f(2) - I_f(1)} \tag{4.21}$$

Finally, the total power loss over a phase-current period can be expressed as:

$$P_{\text{cur,loss}} = 6 \times (P_{\text{IGBT,cur,cond}} + P_{\text{IGBT,cur,sw}}) + (P_{\text{FWD,cur,cond}} + P_{\text{FWD,cur,sw}}) \tag{4.22}$$

4.3.3 SiC-MOSFET Conduction Losses

Conduction losses in SiC power modules come from the resistance of the SiC MOSFETs and the voltage drop across SiC Schottky diodes. These losses are much lower than in traditional silicon devices, making SiC modules more efficient, especially in high-temperature environments. The methodology applied is an analytical approach for estimating conduction losses in SiC-MOSFETs, as explained in [86, 3]. This approach enables the calculation of the average conduction losses of SiC-MOSFETs over one fundamental phase current period.

The 2-Level SiC-MOSFET inverter topology is commonly used in power electronics for driving loads like PMSMs [87]. This configuration offers multiple benefits, such as high efficiency and better thermal management, owing to the advantageous properties of SiC devices.
Based on the gating signals and dead-time, there can be six distinct cases of device conduction for a single-phase leg of a 2L inverter as tabulated in Table 4.1 and illustrated in figure 4.7 (The current flowing out of the inverter leg is considered positive) [87, 64].

Table 4.1: Conducting devices in a phase leg of a 2L inverter [3]

Case	Gating Signal	Current	Devices
1	S1 = 1, S2 = 0	Conducting	S1
2	S1 = 1, S2 = 0	-	S1 (Reverse Conduction)
3	S1 = 0, S2 = 1	-	Negative S2
4	S1 = 0, S2 = 1	+	S2 (Reverse Conduction)
5	S1 = 0, S2 = 0	+	Body diode of S2
6	S1 = 0, S2 = 0	-	Body diode of S1

Cases 5 and 6 represent the period during which both S1 and S2 are off due to dead-time. During this time, the direction of the current determines which device will conduct and thus the output voltage . One current period consists of many switching periods supposing that there are N switching periods in one phase-current period as stated [77].

Calculating conduction losses precisely is not too difficult . One by one, the current in each phase passes through each of the two parts of a switching leg, primarily determined by the load impedance and the enforced output voltage [40].This switching leg's total conduction losses are easily computed as 4.23 .

$$P_{\text{con, SiC}}(t) = R_{\text{DS(on)}}(T_{\text{j}}, V_{\text{GS}}, I_{\text{DS}}) \cdot I_{\text{DS}}^2(t) \tag{4.23}$$

In order to calculate the instantaneous conduction losses as in for each calculation point one must firstly find the value of R_{dson} . Since V_{gs} is usually fixed when the transistor is on, and since the junction temperature does not significantly vary during a fundamental period as

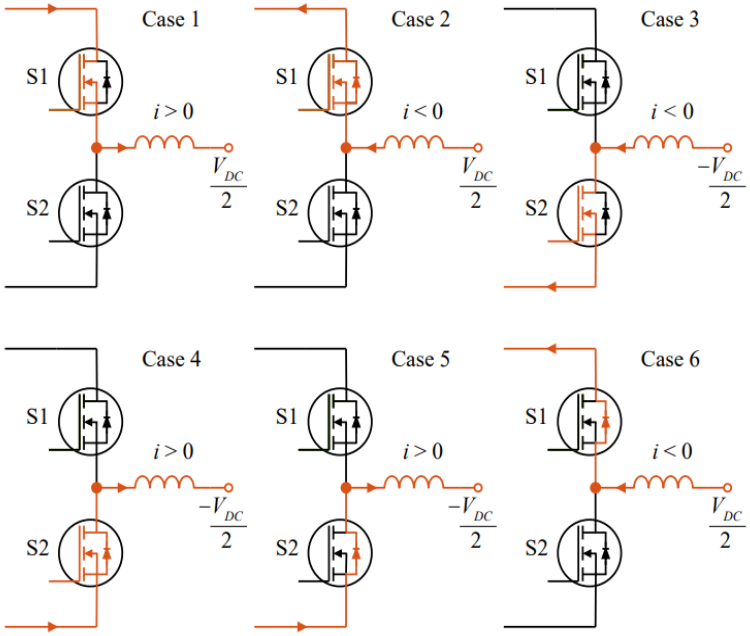

Figure 4.7: Current paths in two-level inverter [3].

described in [40] R_{dson} must be calculated for each current I_{ds} .

$$P_{\text{con, SiC}} = \frac{1}{2\pi} \int_0^{2\pi} R_{\text{DS(on)}}(I_m^2(\alpha)) \cdot D(\alpha)\, d\alpha \tag{4.24}$$

Where $\alpha = \frac{2\pi}{T}$ (where T is the period), I_m represents the MOSFET current, and $D(\alpha)$ is the duty cycle or pulse pattern function, given by :

$$D(\alpha) = \frac{1}{2}\left(1 + m\sin(\alpha)\right) \tag{4.25}$$

To find $R_{\text{DS(on)}}$ we applied a linear interpolation for a given current I_{ds} as shown 4.26 describes how the on-resistance changes with temperature 4.10. Here, T_{min} and T_{max} represent the minimum and maximum junction temperatures used for interpolation, respectively.

$$R_{\text{DS(on)}}(T_{\text{j}}) = \left(\frac{R_{\text{DS(on)}}(T_{\text{max}}) - R_{\text{DS(on)}}(T_{\text{min}})}{T_{\text{max}} - T_{\text{min}}}\right) * (T_{\text{j}} - T_{\text{max}}) + R_{\text{DS(on)}}(T_{\text{max}}) \tag{4.26}$$

During reverse conduction, the MOSFET and diode's current can be obtained as :

$$I_m = \frac{R_d I_p \sin(\alpha - \phi) - V_d}{R_d + R_{\text{dson}}} \tag{4.27a}$$

$$I_d = \frac{R_{\text{on}} I_p \sin(\alpha - \phi) + V_d}{R_d + R_{\text{dson}}} \tag{4.27b}$$

The angle of the displacement power factor is indicated by ϕ, and I_p represents the peak phase current [88]. The MOSFET conduction losses in integral form can be expressed as follows 4.8

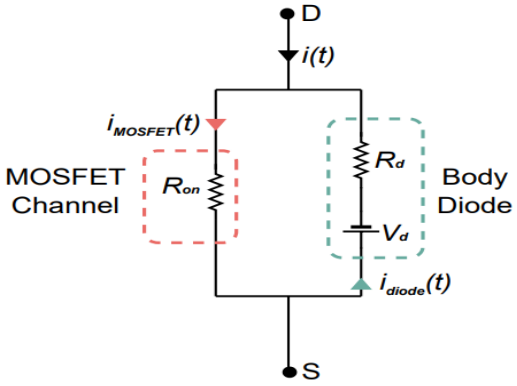

Figure 4.8: Equivalent circuit of MOSFET during reverse Conduction [14].

$$P_{\text{con(SiC)}} = \frac{R_{\text{ds(on)}}}{4\pi}\left(\int_{-\beta}^{\beta+\pi}\left(1+m\sin(v+\phi)\right)I_p^2\sin^2(v)\,dv + \int_{-\beta}^{\beta+\pi}\left(1+m\sin(v+\phi)+\left(\frac{R_dI_p\sin(v)-V_d}{R_{\text{ds(on)}}+R_d}\right)^2\right)dv\right) \tag{4.28}$$

$$\begin{aligned} P_{\text{con\_sic\_mosfet}} = {} & \frac{R_{\text{ds(on)}}}{4\pi}I_p^2\left(\frac{\pi}{2}+\beta-\frac{\sin(2\beta)}{2}+2m\cos(\phi)\left(\cos(\beta)-\frac{\cos^3(\beta)}{3}\right)\right) \\ & + \frac{R_{\text{ds(on)}}}{4\pi(R_{\text{ds(on)}}+R_d)^2}\Bigg[R_d^2I_p^2\left(\frac{\pi}{2}-\beta+\frac{\sin(2\beta)}{2}\right) \\ & - sm\cos(\phi)\left(\cos(\beta)-\frac{\cos^3(\beta)}{3}\right) \\ & + V_d^2\left(\pi-2\beta+2m\cos(\phi)\cos(\beta)\right) \\ & + 2R_dI_pV_d\left(2\cos(\beta)-m\cos(\phi)\left(\frac{\pi}{2}-\beta+\frac{\sin(2\beta)}{2}\right)\right)\Bigg] \end{aligned} \tag{4.29}$$

When the MOSFET is conducting and its on-state voltage drop $I \cdot R_{\text{on}} > V_d$, the diode will also start conducting in parallel with the MOSFET. By substituting 4.27b and 4.25 into 4.29, the conduction loss of the diode in integral form can be expressed as:
As shown in 4.24, the conduction power loss depends on the on-resistance and the modulation function. Likewise, the diode conduction losses can be derived as.

$$p_{\text{con\_Diode}} = \frac{1}{2\pi}\int_0^{2\pi}\left(R_DI_D^2(\alpha)+V_dI_d(\alpha)D(\alpha)\right)d\alpha \tag{4.30}$$

$$P_{\text{con(diode)}} = \frac{R_d}{4\pi}\int_{-\beta}^{\beta+\pi}\left(\left(1+m\sin(v+\phi)\right)\frac{R_dI_p\sin(v)+V_d}{R_d+R_{\text{on}}} - V_d\left(\frac{R_dI_p\sin(v)+V_d}{R_d+R_{\text{on}}}\right)^2\right)dv \tag{4.31}$$

Solving the above equation yields the expression for the conduction power loss of the diode as :

$$
\begin{aligned}
p_{\text{cond\_diode}} = \frac{R_d}{4\pi(R_{on}+R_d)} \Bigg[& i_p^2 R_{on} \left(\frac{\pi}{2} - \beta + \frac{\sin\beta}{2} - 2m\cos\phi \left(\cos\phi - \frac{\cos^3\beta}{3} \right) \right) \\
& + V_d^2 \pi - (2\beta - 2m\cos\phi\cos\beta) \\
& - 2i_p^2 R_{on} V_d \left(2\cos\beta - m\cos\phi \left(\frac{\pi}{2} - \beta + \frac{\sin\beta}{2} \right) \right) \Bigg] \\
- \frac{V_d}{4\pi(R_{on}+R_d)} \Bigg[& mI_p R_{on} \cos\phi \left(\frac{\pi}{2} - \beta + \frac{\sin\beta}{2} \right) \\
& + 2i_p^2 R_{on}\cos\beta - V_d(\pi - 2\beta) + 2V_d m\cos\phi\cos\beta \Bigg]
\end{aligned} \tag{4.32}
$$

The total conduction power loss in a three-phase inverter leg consisting of SiC-MOSFETs and free-wheeling diodes as shown 4.33 can be expressed as :

$$
P_{\text{cond, total}} = 6 * (P_{\text{cond, SiC-MOSFET}} + P_{\text{cond, diode}}) \tag{4.33}
$$

4.4 Conduction Loss Modeling in SVPWM

SVPWM allows for precise power loss modeling in these systems, improving the reliability and efficiency of the inverter under variable operating conditions [15].

4.4.1 IGBT Conduction Loss

In SVPWM, duty cycles are computed from space vector calculations rather than waveform comparisons, as in SPWM .This method improves DC bus utilization and integrates seamlessly with FOC for precise torque and flux regulation [46].

$$
V_{\text{avg}} = D(t)\left(\frac{V_{\text{dc}}}{2}\right) - (1 - D(t))\left(\frac{V_{\text{dc}}}{2}\right) \tag{4.34}
$$

Furthermore, the volt-second equilibrium concept can be used to calculate the operating time of two basic vectors, given that the reference voltage vector V_{dc} is synthesized from the two basic vectors. This relationship can be expressed in terms of 4.34 . Let as take the first section as an example that voltage can be expressed:

$$
V_{\text{avg}} = \frac{T_{v4}}{T_{\text{sw}}}\left(\frac{V_L}{2}\right) + \frac{T_{v6}}{T_{\text{sw}}}\left(\frac{V_L}{2}\right) \tag{4.35}
$$

Then according to the equivalent principle of volt-second balance Figure 4.9, we have the following relationship .

$$
T_{sw} * V_{out} = T_{sw} V_{ref} = T_{4V_4} + T_6 V_6 + T_0 V_0 \tag{4.36}
$$

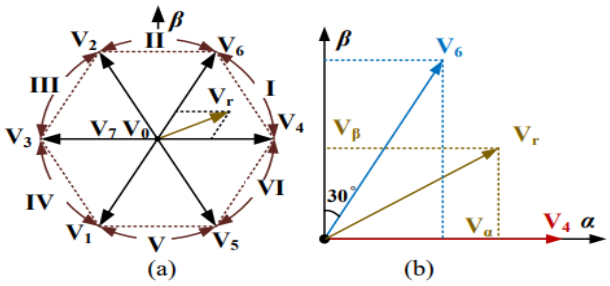

Figure 4.9: (a) Space vector representation of the PMSM drive. (b) Detailed vector composition within Sector I.

As shown in Figure 4.9, the voltage reference is established and the motor's sector is determined using the angle θ. Based on 4.36, the corresponding PWM signal duty cycles are calculated [**?**].

$$\begin{cases} da = t_4 + t_6 + \dfrac{t_7}{t_s}, \\ db = t_6 + \dfrac{t_7}{t_s}, \\ dc = \dfrac{t_7}{t_s} \end{cases} \tag{4.37}$$

The center-aligned PWM signal in sector I 4.10 a and the duty cycle 4.10 b in one period are shown in Figure 4.10 . The conventional SVPWM algorithm needs to identify the sector, calculate the dwell time of the vectors, and finally obtain the duty cycles. The conventional SVPWM algorithm has a high time consumption for the high-speed PMSM drive, which needs a high sampling frequency.

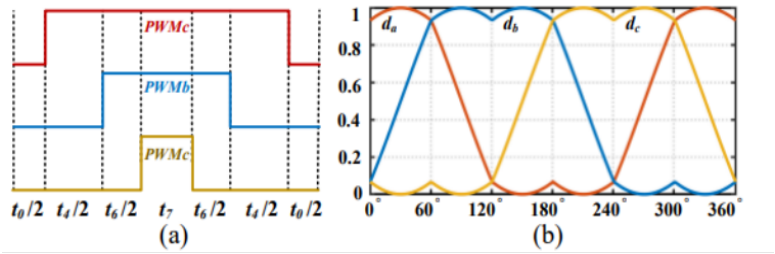

Figure 4.10: (a) The PWM signal in sector I. (b) The duty cycle in one period.

$$\frac{\frac{2}{3}V_{\text{dc}}\left(\frac{T_{v4}}{T_{sw}}\right)}{\sin\left(\frac{\pi}{3}-\alpha\right)} = \frac{V_{\text{ref}}}{\sin\left(\frac{\pi}{3}\right)} \tag{4.38}$$

$$\frac{\frac{2}{3}V_{\text{dc}}\left(\frac{T_{v6}}{T_{sw}}\right)}{\sin\left(\alpha\right)} = \frac{V_{\text{ref}}}{\sin\left(\frac{\pi}{3}\right)}[89] \tag{4.39}$$

Here, α represents the phase angle between the reference voltage vector and the X-axis. Accordingly, equation 4.39 can be written as:

$$\frac{V_{\text{ref}}}{\sin\left(\frac{\pi}{3}\right)} = \frac{\frac{2}{3}V_{\text{dc}}\left(\frac{T_{v4}}{T_{sw}}\right)}{\sin\left(\frac{\pi}{3}-\alpha\right)} = \frac{\sqrt{3}}{2}\left(V_{\text{ref}}\cdot\sin\left(\frac{\pi}{3}-\alpha\right)\right)\cdot\frac{1}{0.5V_{\text{dc}}} \tag{4.40}$$

$$V_{\text{avg}} = \frac{1}{2}\left(\frac{V_{\text{dc}}}{3}\right)\left(\frac{\sqrt{3}}{3} m \sin(\alpha)\right) + \left(\frac{1}{2}V_{\text{dc}}\right)\left(\frac{\sqrt{3}}{2} m \sin\left(\frac{\pi}{3} - \alpha\right)\right) \tag{4.41}$$

The voltage modulation ratio, V_m, is given by $V_m = \frac{2V_{\text{ref}}}{V_{\text{dc}}}$. Likewise, the A-phase voltage in other sectors can be determined. The PWM signals and their duty cycles within each period are crucial for the performance of PWM control in the motor drive phase leg A, as shown in Figure 4.11.

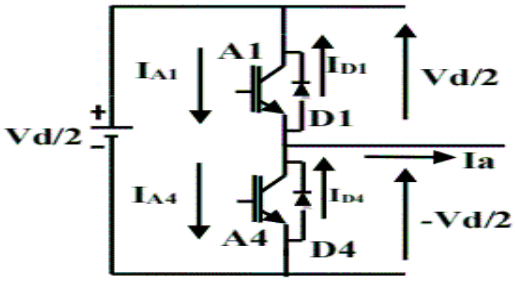

Figure 4.11: Leg A phase current flow and SVPWM modulation techniques [15].

With in the range $0 < \theta < 60°$, equations 4.40 and 4.41 are substituted into equation 4.35, resulting in equation 4.45. Equation 4.42 follows from applying sine-cosine rules further.

$$\begin{cases} \sin(\alpha + \phi) = \sin(\alpha)\cos(\phi) + \cos(\alpha)\sin(\phi), \\ \cos(\alpha + \phi) = \cos(\alpha)\cos(\phi) - \sin(\alpha)\sin(\phi) \end{cases} \quad [89] \tag{4.42}$$

According to the FOC algorithm, the phase current follows a sinusoidal waveform. Given that the phase angle of this current is θ, The current as a function of the phase angle θ can be expressed as:

$$i(\theta) = i_a = I_p \cos(\theta) \tag{4.43}$$

Where the peak current I_p can be calculated as the square root of the sum of the squared current components i^*_α and i^*_β illustrated on 4.44:

$$I_p = \sqrt{(i^*_\alpha)^2 + (i^*_\beta)^2} \ [6] \tag{4.44}$$

However, the average output voltage can be calculated in terms of the duty cycle $D(\alpha)$ as follows:

$$V_{\text{avg}} = \frac{V_{\text{dc}}}{2}(2D(\alpha) - 1) \tag{4.45}$$

Here, the duty cycle $D(\alpha)$ [41] can be calculated as:

$$d(\alpha) = \frac{2D(\alpha) - 1}{m} \tag{4.46}$$

Now, we need to determine the duty cycle for the proposed method. There are various methods available to calculate the duty cycle $D(t)$ as shown in 4.46 for a switch in a SVPWM inverter

[15], in addition to the one presented in this thesis.

$$d(\alpha) = \frac{2D\alpha - 1}{m} = \begin{cases} \frac{\sqrt{3}}{2}\cos\left(\alpha - \frac{\pi}{6}\right) & 0 \le \alpha < \frac{\pi}{3} \\ \frac{3}{2}\cos(\alpha) & \frac{\pi}{3} \le \alpha < \frac{2\pi}{3} \\ \frac{\sqrt{3}}{2}\cos\left(\alpha + \frac{\pi}{6}\right) & \frac{2\pi}{3} \le \alpha \le \pi \\ \frac{\sqrt{3}}{2}\cos\left(\alpha - \frac{\pi}{6}\right) & \pi < \alpha \le -\frac{2\pi}{3} \\ \frac{3}{2}\cos(\alpha) & -\frac{2\pi}{3} < \alpha \le -\frac{\pi}{3} \\ \frac{\sqrt{3}}{2}\cos\left(\alpha - \frac{\pi}{6}\right) & -\frac{\pi}{3} < \alpha < 0 \end{cases} \quad [89] \tag{4.47}$$

Similarly, it can be proved that $d(\alpha)$ can be expanded as a Fourier series.The expansion of the Fourier series for $d(\alpha)$ can be expressed as [15]:

$$\mathbf{d}(\alpha) = \frac{a_0}{2} + \sum_{n=1}^{\infty} \left(a_n \cos(n\alpha) + b_n \sin(n\alpha)\right)$$

where

$$b_n = 0, a_1 = 0$$

$$a_n = \frac{\sqrt{3}}{2\pi(1-n^2)}\left[2\sin^2\left(\frac{n\pi}{2}\right) - 4\sin^2\left(\frac{n\pi}{3}\right) + 4\sin^2\left(\frac{n\pi}{6}\right)\right]$$

The Fourier coefficient a_n can be explored in more detail for cases where n is expressed as $n = 3^k$. In this scenario, we have:

$$a_n = \begin{cases} \frac{3\sqrt{3}}{(1-3)^{2k}\pi} & \text{if } n = 3^k,\ k = 1, 2, 3, \ldots \\ 0 & \text{if } n \neq 3^k \text{ for } k = 1, 2, 3, \ldots \end{cases} \quad [15] \tag{4.48}$$

For $n = 1$:$a_1 = \frac{3\sqrt{3}}{\pi}$ and for $n = 3$:$a_3 = \frac{3\sqrt{3}}{4\pi}$ therefore , The expression for the third-order harmonic component $d_3(\alpha)$ is given by:

$$d_3(\alpha) = \cos(\alpha) + \frac{3\sqrt{3}}{8\pi}\cos(3\alpha) \tag{4.49}$$

From 4.46, we have d_α By inserting 4.45 into 4.41, we can simplify the duty cycle 4.50 as follows:

$$D(\alpha) = \frac{1}{2}\left(1 + m\left(\cos(\alpha) - \frac{3\sqrt{3}}{8\pi}\cos(\alpha)\right)\right) \quad [15] \tag{4.50}$$

Substitute 4.50 into 4.9 we get as follows 4.51

$$P_{\text{IGBT, SVPWM}}(\theta) = \frac{1}{2\pi}\int_{-\frac{\pi}{2}}^{\frac{\pi}{2}} \left(V_{CE0} + R_{CE} \cdot I_p \cos(\theta)\right) I_p \cos(\theta) \cdot \frac{1}{2}\left(1 + m\cos(\theta + \phi)\right.$$
$$\left. -\frac{3\sqrt{3}}{8\pi}\cos\left(3(\theta + \phi)\right)\right) d\theta \tag{4.51}$$

By evaluating the integral in 4.51, the IGBT conduction loss model under SVPWM, based on the instantaneous current over one cycle, can be derived and expressed in 4.52.

$$P_{\text{igbt,cond}}(T) = \frac{R_{ce}(T)I_p^2}{8}\left(1 + \frac{8m\cos(\phi)}{3\pi} - \frac{8\sqrt{3}m\cos(3\phi)}{40\pi^2}\right) + \frac{V_{ceo}(T)I_p}{2\pi}\left(1 + \frac{2I_p m\cos(\phi)}{8}\right) \tag{4.52}$$

The IGBT parameters $V_{CE0}(T)$ and $R_{CE}(T)$, representing the voltage drop and on-state resistance as functions of temperature, are usually taken from the device datasheet at various temperatures.

It is important to consult the specific datasheet for the IGBT device to understand how these parameters vary with temperature, as this variation can significantly affect the device's performance and efficiency in different operating conditions [77].

By applying linear interpolation to Figure 4.6, the temperature dependence of the IGBT parameters $V_{CE0}(T_j)$ and $R_{CE}(T_j)$ is derived using the reference temperature points $T_{\min}$ and $T_{\max}$. As demonstrated in 4.53 and 4.54, the values of $V_{CE0}(T_j)$ and $R_{CE}(T_j)$ can be calculated based on these reference temperatures.

$$V_{ce0}(T_j) = \frac{V_{ce0}(\max) - V_{ce0}(\min)}{T_{\max} - T_{\min}}(T_j - T_{\max}) + V_{ce0}(T_{\max}) \tag{4.53}$$

$$R_{ce}(T_j) = \frac{R_{ce}(\max) - R_{ce}(\min)}{T_{\max} - T_{\min}}(T_j - T_{\max}) + R_{ce}(T_{\max}) \tag{4.54}$$

The power factor angle ϕ in 4.55 can be derived from the voltage and current phase angles in the two phase stationary coordinate system. According to 4.12, the power factor angle can be expressed as [3] :

$$\phi = \alpha - \gamma \tag{4.55}$$

Where the voltage phase angle α and the current phase angle γ can be calculated as shown in 4.57 and 4.56.

$$\alpha = \arctan\left(\frac{V_{\beta\text{ref}}}{V_{\alpha\text{ref}}}\right), \tag{4.56}$$

$$\gamma = \arctan\left(\frac{i_\beta^*}{i_\alpha^*}\right) \tag{4.57}$$

4.4.2 Diode Conduction Loss

In power electronic converters, FWDs conduct during the off-state of the main switches. The modeling of conduction losses for the FWD follows a similar approach to that of the main switch, based on instantaneous current and voltage characteristics. However, the key difference is in the conduction period. When the main switch is off, the diode conducts, making its duty ratio the complement of the switch duty cycle $D(\alpha)$, as defined in 4.51. Thus, the diode duty

cycle is given by:

$$D_{\text{diode}}(\alpha) = 1 - D(\alpha) = \frac{1}{2}\left(1 - m\cos(\alpha) + \frac{3\sqrt{3}}{8\pi}\cos(\alpha)\right) \tag{4.58}$$

The diode conduction loss $P_{\text{cond,diode}}(T_j)$ is then given by:

$$\begin{aligned} P_{\text{cond,diode}}(T_j) = \frac{1}{2\pi}\int_{-\frac{\pi}{2}}^{\frac{\pi}{2}} \left(V_f(T_j) + R_f(T_j) I_p \cos\theta\right) I_p \cos\theta \\ * \frac{1}{2}\left[1 - m\cos(\theta+\phi) + \frac{3\sqrt{3}}{8\pi}\cos\big(3(\theta+\phi)\big)\right] d\theta \end{aligned} \tag{4.59}$$

$$\begin{aligned} P_{\text{cond,diode}}(T_j) = \frac{R_f(Tj) I_p^2}{8}\left(1 + \frac{8m\cos(\phi)}{3\pi} - \frac{8\sqrt{3}m\cos(3\phi)}{40\pi^2}\right) \\ + \frac{V_f(\text{j}) I_p}{2\pi}\left(1 + \frac{2I_p m\cos(\phi)}{8}\right) \end{aligned} \tag{4.60}$$

Where R_f and V_f are the temperature-dependent parameters of the FWD , calculated as in 4.61 and 4.62 , they are measured values based on the device datasheet under different temperatures [69, 40, 90], The linear functions of the diode junction temperature are obtained based on the reference values at temperatures T_{min} (℃) and T_{max} (℃) from the datasheet as shown Figure 4.6 .

$$V_f(T_j) = \frac{V_f(\max) - V_f(\min)}{T_{\max} - T_{\min}}(T_j - T_{\max}) + V_f(T_{\max}) \tag{4.61}$$

$$R_f(T_j) = \frac{R_f(\max) - R_f(\min)}{T_{\max} - T_{\min}}(T_j - T_{\max}) + R_f(T_{\max}) \tag{4.62}$$

Alternatively,these parameters can also be represented as shown in 4.63 and 4.64.

$$V_f(T_j) = \frac{V_{f2}\cdot T_{\min} - V_{f1}\cdot T_{\max}}{T_{\min} - T_{\max}} + \frac{V_{f2} - V_{f1}}{T_{\min} - T_{\max}} T_j \tag{4.63}$$

$$R_f = \frac{R_{f2}\cdot T_{\min} - R_{f1}\cdot T_{\max}}{T_{\min} - T_{\max}} + \frac{R_{f2} - R_{f1}}{T_{\min} - T_{\max}} T_j \tag{4.64}$$

4.4.3 SiC-MOSFET Conduction Loss

The conduction losses of a SiC MOSFET can be calculated analytically based on the MOSFET's on-state resistance $R_{\text{DS(on)}}$, the current through the device, and the duty cycle of operation [46, 47].
The average power conduction loss over a switching period T_0 can be expressed as:

$$P_{\text{cond,MOSFET}} = \frac{1}{T_0}\int_0^{T_0/2} R_{\text{on}} \left(I\sin(\omega t)\right)^2 D(t) dt \tag{4.65}$$

This equation calculates how much power is dissipated as heat in the SiC-MOSFET when it's conducting current.

After substituting pulse pattern function, that is 4.50 in 4.65, the conduction loss in SiC-MOSFET can be written as 4.66,

$$P_{\text{cond, SiC}} = \frac{1}{2\pi} \int_{-\beta}^{\beta+\pi} R_{DS(on)} I^2 m(\alpha) D(\alpha)\, d\alpha \tag{4.66}$$

The expressions for the SiC-MOSFET current I_m and the diode current I_d are defined in 4.27b. By substituting the duty cycle $D(\alpha)$, as defined in 4.50, into 4.66, the resulting expression is 4.67.

$$P_{\text{cond, SiC}} = \frac{R_{DS(on)}}{4\pi(R_d + R_{dson})^2} \int_{-\beta}^{\beta+\pi} (R_d I_p \sin(\alpha - \phi) - V_d)^2 \left(1 + \left(m - \frac{8}{3\pi}\right)\cos(\alpha)\right) d\alpha \tag{4.67}$$

After substituting everything and simplifying, we arrive at a closed-form equation as follow:

$$\begin{aligned} P_{\text{cond, SiC}} = & \frac{R_{DS(on)}}{4\pi(R_d + R_{dson})^2} \Bigg[R_d^2 I_p^2 \left(\beta + \frac{\pi}{2} + \frac{\sin(2(\beta-\phi))}{2} \right. \\ & \left. - \frac{\sin(2(\beta+\phi))}{2} + \left(m - \frac{8\sqrt{3}}{3\pi}\right) \frac{-\sin^3(\beta-\phi) + \sin^3(\beta+\phi)}{3} \right) \Bigg] \\ & - 2R_d I_p V_d \Bigg[\cos(\beta-\phi) + \cos(\beta+\phi) \\ & + \left(m - \frac{8\sqrt{3}}{3\pi}\right) \frac{1}{4} \left(\cos(2(\beta-\phi)) + \cos(2(\beta+\phi))\right) \Bigg] \\ & + V_d^2 \left[2\beta + \pi + \left(m - \frac{8\sqrt{3}}{3\pi}\right) \left(\sin(\beta+\phi) - \sin(\beta-\phi)\right) \right] \end{aligned} \tag{4.68}$$

The angle β defines the conduction interval of the SiC-MOSFET, that is, the period during which the device conducts current (is turned on), and is given by:

$$\beta = \sin^{-1}\left(\frac{V_d}{R_{on} I_p}\right) \tag{4.69}$$

4.5 Switching Loss Modeling

In power electronics, switching losses are the energy dissipated by a semiconductor device (such as a SiC-MOSFET or IGBT) during the dynamic transition between its conducting (ON) and non-conducting (OFF) states [38].

4.5.1 IGBT Switching Losses

Conduction losses are primarily influenced by the flowing current, whereas switching losses are proportionately dependent on the switching frequency (fsw) [14]. For this reason, fsw

multiplied by the switching energy loss Esw yields the switching losses. Likewise, diodes are taken into consideration for reverse recovery energy (Erec), rather than the turn-on (E_{on}) and (E_{off}) turn-off energy loss [14].

$$P_{sw\_IGBT} = E_{sw} * f_{sw} = (E_{on} + E_{off}) * f_{sw} \tag{4.70}$$

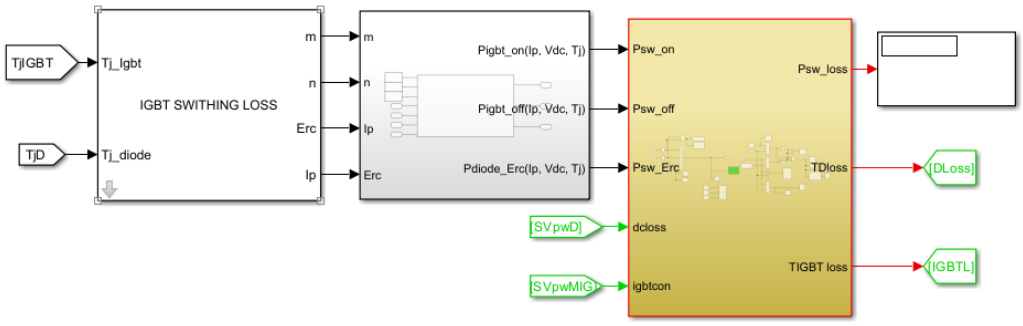

Figure 4.12: Switching loss MATLAB model.

The switching losses are stated in the datasheets provided by the manufacturers as a function of temperature, nominal current, and voltage [91]. As demonstrated in Figure 4.12 , the easiest method of adaptation to the actual application is to perform linear interpolation of the provided values [41].

In the two-level topology, the full DC link voltage is switched and thus used as V_{dc}. Consequently, the total power loss of a given transistor can be expressed as:

$$P_{\mathrm{sw}} = \frac{f_{\mathrm{sw}}}{2\pi} \int_{\theta_1}^{\theta_2} E_{\mathrm{sw}} \cdot \frac{I_p}{I_{\mathrm{nom}}} \cdot \frac{V_{\mathrm{dc}}}{V_{\mathrm{nom}}} \, d\theta \tag{4.71}$$

$$= \frac{f_{\mathrm{sw}}}{\pi} \int_{\phi}^{\phi+\pi} E_{\mathrm{sw}} \cdot \frac{\sin(\theta - \phi)}{I_{\mathrm{nom}}} \cdot \frac{V_{\mathrm{dc}}}{V_{\mathrm{nom}}} \, d\theta$$

$$P_{\mathrm{sw}} = \frac{f_{\mathrm{sw}}}{\pi} * \sum E_{\mathrm{sw}}(E_{\mathrm{on}}, E_{\mathrm{off}}) * \frac{I_p}{I_{\mathrm{nom}}} * \frac{V_{\mathrm{dc}}}{V_{\mathrm{nom}}} \tag{4.72}$$

Thus, 4.73 expresses the total switching power losses (P_{sw}) as the sum of the IGBT switching losses ($P_{sw,IGBT}$) and the freewheeling diode switching losses ($P_{sw,FWD}$) 4.77:

$$P_{Total,sw,IGBT} = 6 * (P_{sw,IGBT} + P_{sw,FWD}) \tag{4.73}$$

4.5.2 SiC-MOSFET Switching Losses

Switching losses arise during the turn-on and turn-off events of both the switch and its anti-parallel diode, and are modeled in MATLAB and PLECS, as shown in Figure 4.12. These losses are directly related to the switching energy, which, similar to other power devices, can be determined from the product of voltage and current [86].

$$E_{\text{sw}} = \int V_d(t) i(t)\, dt \Big|_{\text{Eon}} + \int V_d(t) i(t)\, dt \Big|_{\text{Eoff}} = (E_{\text{on}} + E_{\text{off}}) \tag{4.74}$$

According to [92], the off-state leakage current for a power MOSFET is very low and therefore the blocking losses can be neglected .The analytical equation for the switching losses is

$$P_{\text{sw}}(\text{Sic}) = f_{\text{sw}} * (E_{off,nom}(I_{nom}, V_{nom}) + E_{on,nom}(I_{nom}, V_{nom})) \left(\frac{1}{\pi} * \frac{I_p}{I_{\text{nom}}} * \frac{V_{\text{dc}}}{V_{\text{nom}}} \right) \tag{4.75}$$

4.5.3 Diode Reverse Recovery losses

Finally, the diode switching losses are calculated similarly by determining the switching energy losses. The diode switching losses can be expressed as:

$$P_{sw\_d} = E_{rec} * f_{sw} \tag{4.76}$$

$$P_{\text{sw}}(\text{D}) = f_{\text{sw}} * E_{rr,\text{nom}}(I_{\text{nom}}, V_{\text{nom}}) \left(\frac{1}{\pi} * \frac{I_p}{I_{\text{nom}}} * \frac{V_{\text{dc}}}{V_{\text{nom}}} \right) \tag{4.77}$$

Manufacturers' datasheet specify the switching energy losses in dependency on a certain (nominal) current and voltage, as well as a temperature [34]. Equation 4.73 and 4.73 expresses the power switching losses (P_{sw}) as the sum of the SiC-MOSFET power switching losses ($P_{sw,SiC}$) and the FWD switching losses ($P_{sw,D}$):

$$P_{Total,sw,SiC} = 6 * (P_{sw,SiC} + P_{sw,D}) \tag{4.78}$$

4.6 Thermal Modeling

In power electronic devices, the junction temperature (T_j) significantly affects how the device performs, especially in terms of key parameters on-state resistance (R_T , R_D), forward voltage drops (V_T , V_D), and switching and reverse recovery energies E_{on}, E_{off}, and E_{rec}. Because these parameters impact power loss, accurately accounting for T_j is essential for reliable device operation and efficiency [93].

In order to ensure a sufficient life time of power electronics application systems, proper thermal design is indispensable and one of the critical items to be considered. In a thermal model, a component equivalent to transient thermal resistance is replaced with an electrical circuit model, which helps to predict the transient thermal resistance characteristics using an electrical circuit.

4.6.1 Thermal Equivalent Network

The thermal resistance R_{th} and thermal capacitance C_{th} are commonly represented as cascaded RC networks. These networks effectively describe the dynamic thermal impedance and simulate the thermal behavior of materials, particularly in semiconductor devices [54]. Two methods can be employed to model such RC networks.

4.6.1.1 Foster Model

The Foster model is widely used, with parameters typically provided by manufacturers in their data-sheets. However, it is important to note that this model represents a mathematical fitting of the thermal impedance Z_{th} [76]. The analytical formula relating the thermal impedance to the thermal resistance is described as follows:

$$Z_{\text{th}}(j\omega)(t) = \sum_{i=1}^{n} \left(R_i \left(1 - e^{-\frac{t}{\tau_i}} \right) \right) \quad \text{where} \quad \tau_i = R_i C_i \text{ [76]} \tag{4.79}$$

4.6.1.2 Cauer Model

The Cauer model uses a sequence of resistor-capacitor (RC) networks to represent the thermal impedance [94]. The Cauer model typically takes the form of a sum of terms representing RC networks as shown 4.80:

$$Z_{th}(j\omega)(t) = \sum_{i=1}^{n} \left(\frac{R_i}{1 + j\omega\tau_i} \right), \ where \ \tau_i = R_i C_i. \tag{4.80}$$

In thermal modeling of a power semiconductor module, such as an IGBT or SiC MOSFET, thermal resistances and capacitances represent the heat transfer and storage characteristics. Each component plays a critical role in accurately capturing these dynamics:

I. Thermal Resistances (R_{th})

1. Junction-to-Case Resistance ($R_{\text{th(jc)}}$) : Represents the thermal resistance from the semiconductor junction, where heat is generated, to the outer surface of the module's case.This resistance quantifies the module's ability to conduct heat from the junction to the case, an essential factor in managing temperature.

2. Case-to-Heatsink Resistance ($R_{\text{th(cs)}}$) : Denotes the thermal resistance between the module case and the heatsink or cooling system attached to it.This resistance indicates the effectiveness of heat transfer from the case to the cooling system.

3. Heatsink-to-Ambient Resistance ($R_{\text{th(sa)}}$) : Represents the thermal resistance between the heatsink and the surrounding air or coolant. This parameter is critical in estimating how well the system dissipates heat to the ambient environment.

II. Thermal Capacitances (C_{th})

1. Junction Capacitance ($C_{\text{th(j)}}$) : Represents the thermal capacitance of the semiconductor junction, indicating its ability to store and release heat. A higher capacitance here implies a greater ability to store heat, which affects transient temperature responses.

2. Module Case Capacitance ($C_{\text{th(c)}}$) : Represents the thermal capacitance of the module case, affecting the time constant of heat transfer from the junction to the case. This

parameter is key in understanding temperature changes within the module case over time.

3. Heat-sink Capacitance ($C_{\text{th(s)}}$) : Represents the thermal capacitance of the heat-sink or cooling system. This capacitance impacts how quickly the heat-sink can absorb and release heat to the ambient, influencing steady-state and transient behavior.

4.6.2 Heat Spreading and Temperature Calculation

Heat spreading through different layers and the total dissipated power is influenced by transient thermal impedance Zth [95]. The steady-state temperatures are calculated as follows: The steady-state case temperature for a module with base plate is calculated for constant total power [96] dissipation as follows:

$$T_c = T_a + \left(R_{th(h-a)} + R_{th(c-h)}\right) \cdot P_{loss\_total} \tag{4.81}$$

Similarly, the steady-state heatsink temperature for a module without base plate is given by:

$$T_h = T_a + R_{th(h-a)} \cdot P_{loss\_total} \tag{4.82}$$

Moreover,as stated on [95] the steady-state inverter junction temperature for a module with base plate is obtained taking into consideration the power losses of the inverter as follows:

$$T_{j(inverter)} = T_h + R_{th(j-s)} \cdot P_{loss,Inverter} \tag{4.83}$$

The figure 4.13 and 4.14 illustrates the thermal management and temperature calculation MATLAB Simulink model for all given steady-state Temperature calculations.

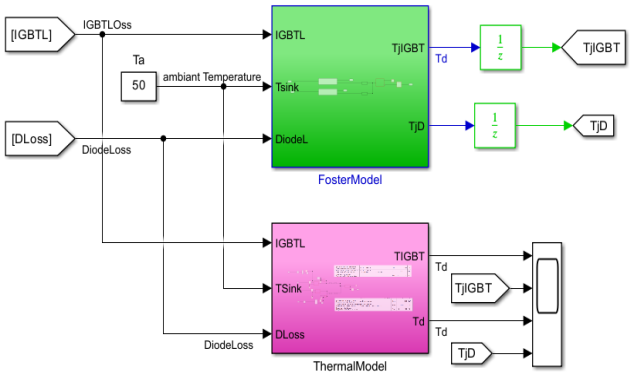

Figure 4.13: Heat Spreading and Temperature Calculation Simulink Model of SI-IGBT

4.6.3 Heat Sink Fundamentals

The heat-sink absorbs the switching and conduction losses of all devices in its boundary [97]. A heat sink simultaneously describes an isothermal atmosphere and distributes its temperature to the surrounding components [97]. The semiconductors mounted on the heat sink will have

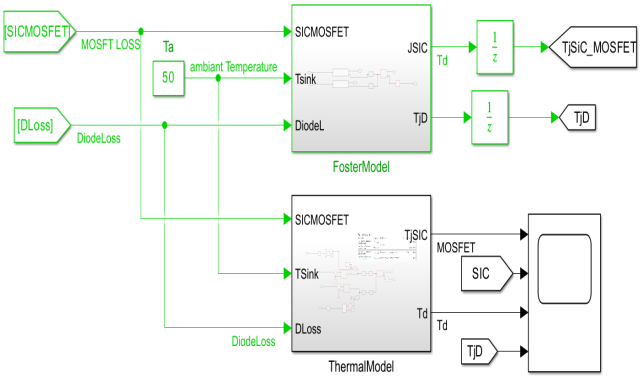

Figure 4.14: Heat Spreading and Temperature Calculation Simulink Model of SIC-MOSFET

the same case temperature. The electrical equivalent of the thermal circuit with heat sink in PLECS for MOSFET and IGBT is described in figure 4.15 a and b, respectively.

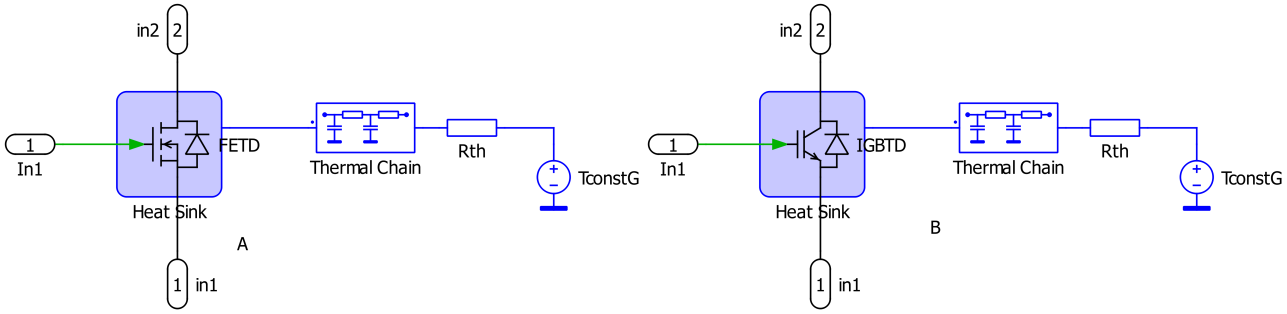

Figure 4.15: Electrical equivalent of thermal circuit (A) SiC-MOSFET (B) IGBT .

Figure 4.16 represents how power losses are calculated in an inverter system and how these losses are then used to determine the junction temperature of the system.

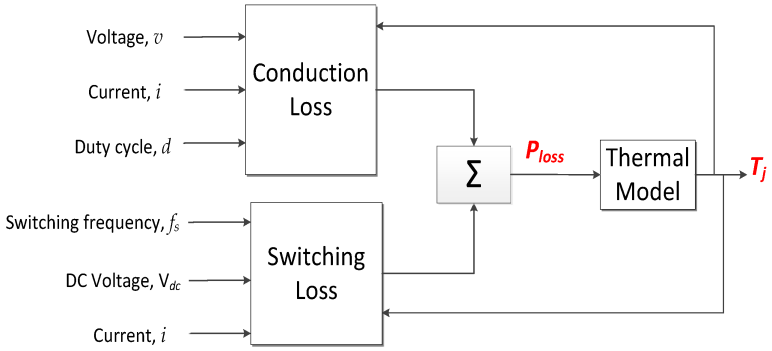

Figure 4.16: Total power loss analysis block diagram.

Chapter 5

Simulation Results and Discussion

This chapter presents the results of the drive system model developed in Chapter 4. Simulations were carried out using MATLAB/SIMULINK and PLECS to evaluate overall system performance. The key objectives include analyzing inverter behavior, examining voltage and current waveforms, investigating power loss models, and assessing the impact of semiconductor devices on system efficiency. A comparison between SPWM and SVPWM is also included to highlight their respective advantages and limitations under various conditions.

The online simulator is used to cross-validate the results [98]. We utilized parameters for both the IPMSM and a three-phase inverter throughout the system, as accurate characterization of these parameters is crucial for effective motor design and control. Tables 5.1 and 5.2 present the drive motor and inverter parameters for the IPMSM, respectively.

Table 5.1: Inverter Parameters

Parameter	**Symbol**	**Numerical Value**
DC-Link Voltage	V_{dc}	1500 V
Switching Frequency	f_{sw}	10 kHz
Modulation Techniques		SPWM, SVPWM
Semiconductor Modules		IGBT, SiC-MOSFET

5.1 Control Strategy Performance

This section evaluates the control strategy applied to the IPMSM drive system, focusing on the inverter's output waveforms, voltage, and current behavior in the rotating reference frame. The system's torque and speed response. The implemented control strategy combines Field-Oriented Control (FOC), Maximum Torque per Ampere (MTPA), and Zero d-axis current techniques to enhance torque production and dynamic performance [99]. The overall control strategy for the IPMSM drive system is illustrated in Figure 5.1, which shows the block diagram of the implemented control method.

Table 5.2: IPM Motor Parameters [16]

Parameter	Symbol	Numerical Value
Rated Current	I	138 A
Rated Voltage	V	926 V
Rated Power	P	190 kW
Rated Speed	ω	1800 rpm
Pole Pairs	n_p	4
Stator Resistance	R_s	0.0459 Ω
q-axis Inductance	L_q	3.96 μH
d-axis Inductance	L_d	1.58 μH
Permanent Magnet Flux	λ_{pm}	0.6838 Wb

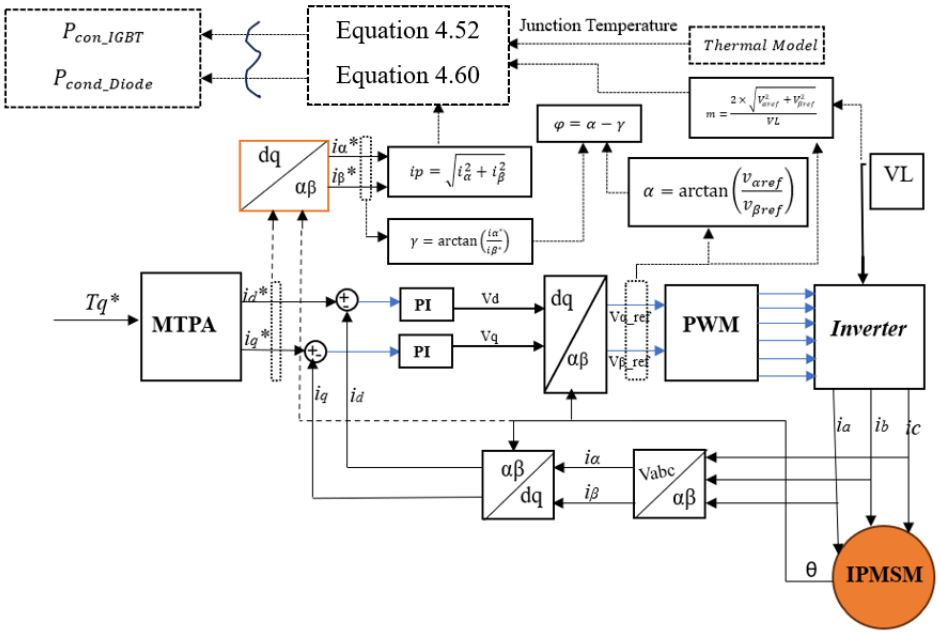

Figure 5.1: Overall control block diagram of an IPMSM drive system using SVPWM.

5.1.1 Analysis of Inverter Output Waveforms under SPWM and SVPWM

Three-phase stator current and output voltage waveforms for both modulation schemes are presented in Figures 5.2 and 5.3. From the simulation, it is evident that SVPWM offers better voltage utilization compared to SPWM, with the output voltages being up to 15% higher [46]. Current waveforms generated using SVPWM are significantly smoother with lesser harmonic content as well. The improvement in waveform quality is clearly reflected in the Fast Fourier Transform (FFT) analysis, which shows a noticeable reduction in Total Harmonic Distortion (THD) when SVPWM is applied [100].

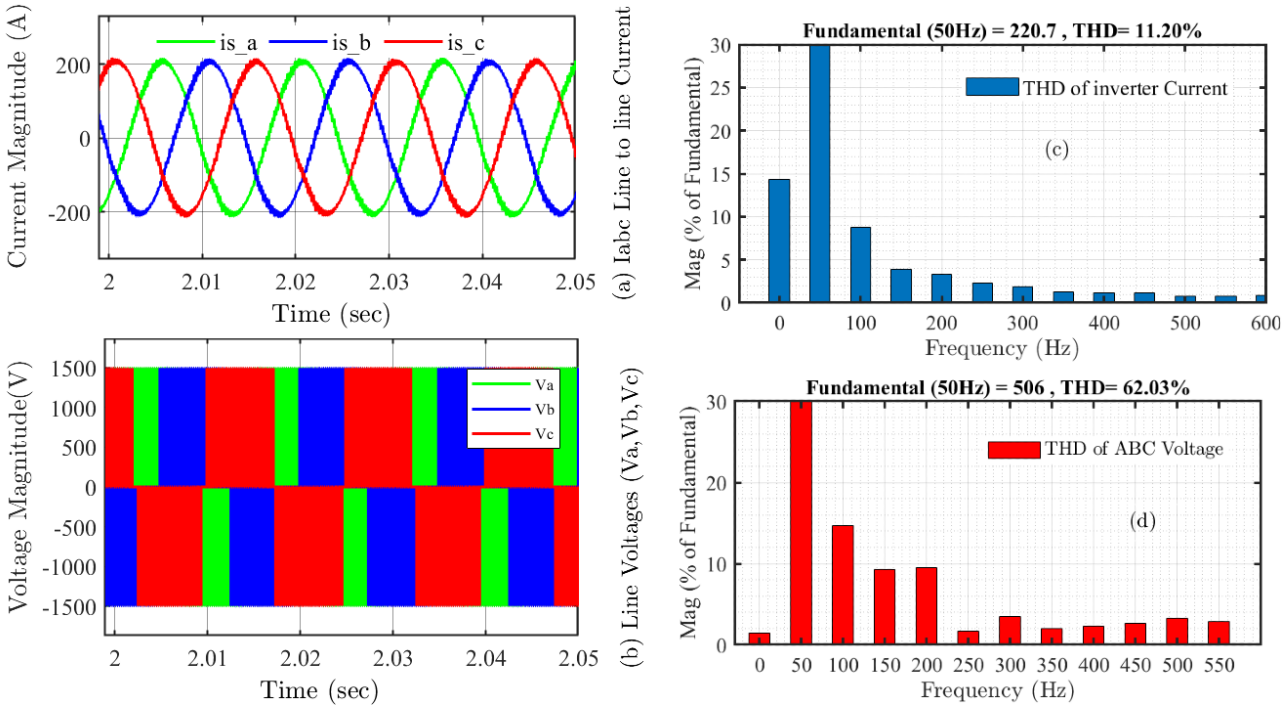

Figure 5.2: SPWM Waveforms of the system: (a) Line currents, (b) Line voltages, (c) THD of inverter current, (d) THD of ABC voltage.

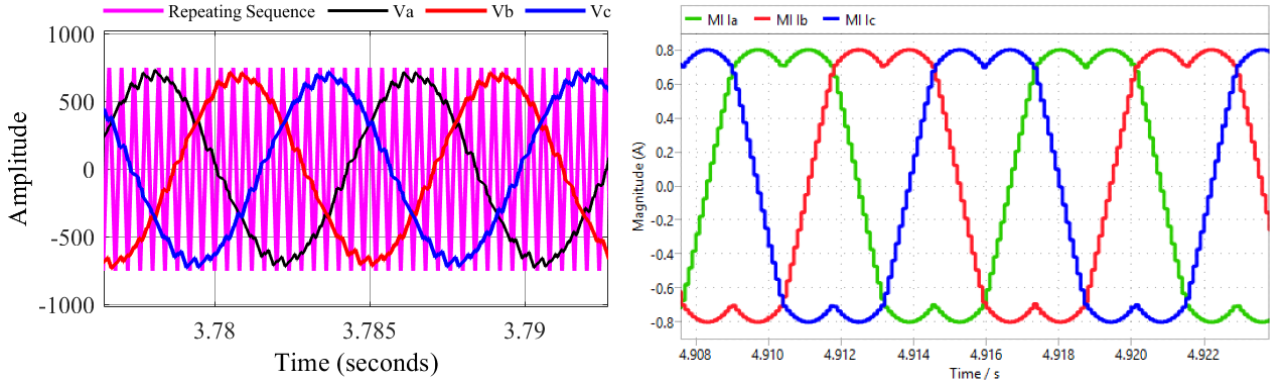

Figure 5.3: Comparison of SPWM and SVPWM waveforms: (a) Modulating (reference) and carrier (triangular) wave for SPWM pulse generation, (b) Modulating waveform used in the generation of SVPWM signals.

5.1.2 Speed and Torque Performance Analysis

The torque and speed response of IPMSM was analyzed under various operating conditions to evaluate the performance of the implemented control strategy.

5.1.2.1 Steady-State Performance

Operating at 188.5 rad/s or 1800 rpm, the system exhibited a stable torque with minimal fluctuations, as illustrated in Figure 5.4 there is a slight fluctuation at the beginning and after 2.65 sec, the electromagnetic torque is constant at 1000 Nm. SVPWM combined with SiC MOSFETs enhances efficiency and provides superior torque regulation at higher speeds.

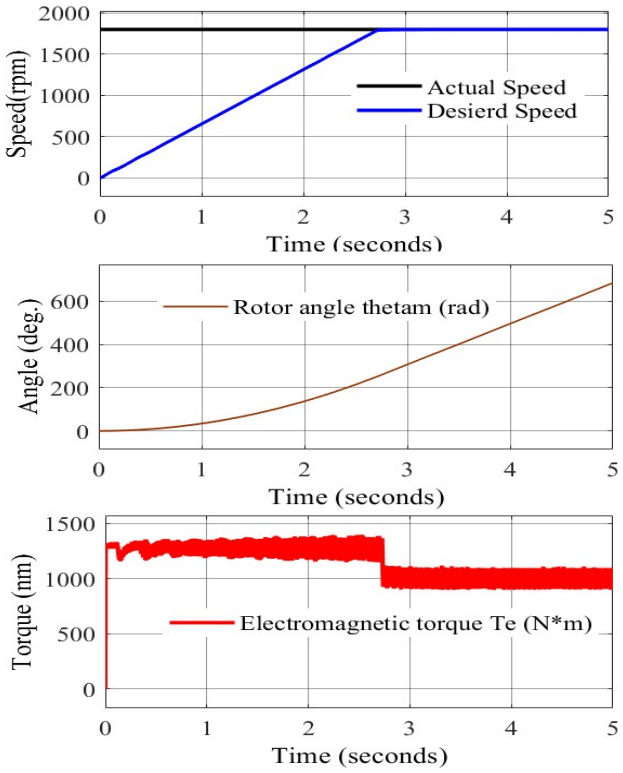

Figure 5.4: Steady-State Torque Response at Constant Reference Speed in rpm.

5.1.2.2 Transient Performance

A simulation result for a speed change from zero rpm to the rated speed (1800 rpm) and then in reverse condition. Finally, the speed is brought back to zero rpm at rated load is shown in figure 5.5. It can be understood that the PI controller has good speed-tracking performance and also it shows the changes in electromagnetic torque and how well the motor maintains its target speed.

5.2 Semiconductor Loss Analysis

The total power loss in the IPMSM inverter system consists of conduction and switching losses, and these were calculated separately for Si-IGBT and SiC-MOSFET based inverters. The loss evaluation was carried out under two modulation strategies, namely SPWM and SVPWM. This comparative method provides valuable insights into the trade offs between control strategy, device type, and overall system efficiency.

5.2.1 Losses in SPWM

Conduction and switching losses of three-phase inverters with SiC MOSFETs, IGBTs, and FWDs were analyzed under SPWM strategy in steady-state and transient conditions using MATLAB/Simulink and PLECS. The MATLAB model's results were validated against IPOSIM, Semisel V6, and ABB DriveSize simulation tools.

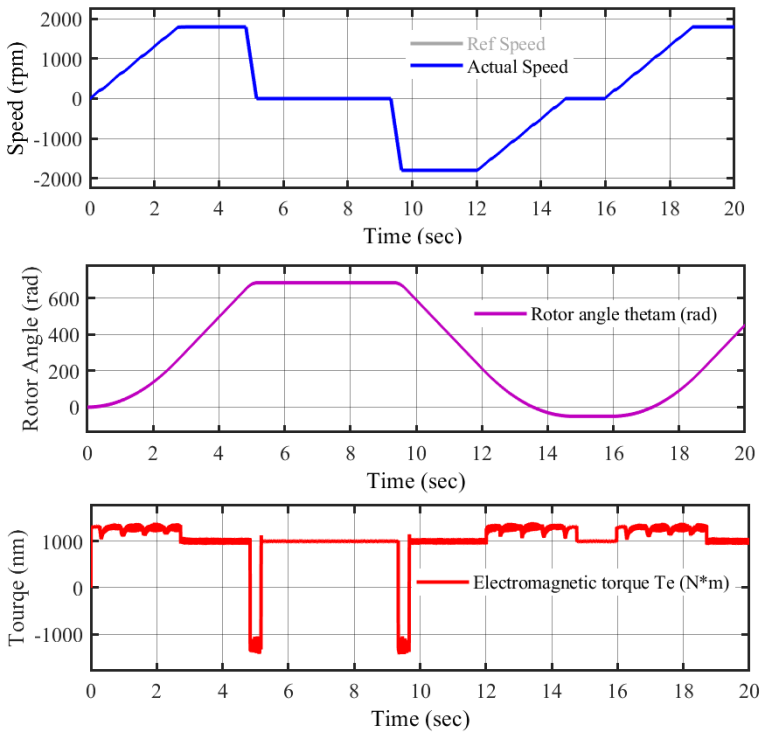

Figure 5.5: Torque (Nm) and speed tracking performance (rpm) under load variation.

5.2.1.1 Losses From Infineon Module

The power losses of the IGBT and diode for the Infineon module under rated operating conditions are summarized in Table 5.3 and illustrated figure 5.6. It can be seen that the results from the PLECS and MATLAB models are comparable to those obtained from the Infineon simulator , this shows that the developed loss model accurately captures the inverter losses under rated conditions .

During transient operation, as shown in Figure 5.7, power losses fluctuate considerably as the reference speed changes from 0 rpm to ±1800 rpm and back to 0 rpm. These fluctuations are driven by rapid variations in load, current magnitude, and switching activity throughout acceleration, deceleration, and regenerative braking phases. As a result, both the conduction and switching losses of the IGBT and diode vary dynamically during these conditions.

Table 5.3: Power Losses of IGBT and Diode for FZ600R12KE4 Module.

Loss Type	**MATLAB**	**IPOSIM**	**PLECS**
IGBT Conduction Loss [W]	708.3	712.6	701.238
IGBT Switching Loss [W]	629.6	625.663	630.8
Diode Conduction Loss [W]	15.96	15.20	14.8054
Diode Switching Loss [W]	218.6	218.67	227.98

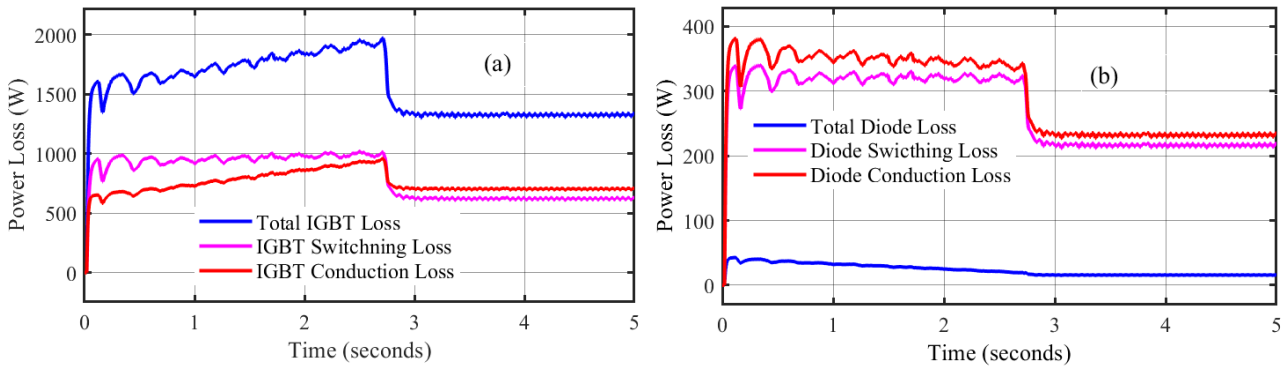

Figure 5.6: Conduction and switching loss analysis of the Infineon module under rated operating condition (a) IGBT Conduction and switching loss (b) Diode conduction and switching loss.

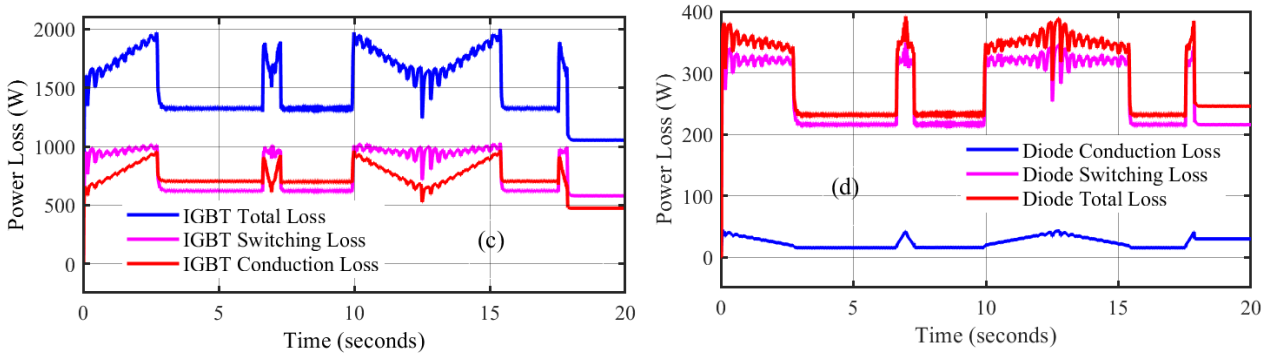

Figure 5.7: Power loss variation during transient speed changes (c) IGBT Conduction and switching loss (d) Diode conduction and switching loss..

5.2.1.2 Losses From Semikron Module

The power losses of the IGBT and diode for the Semikron module under rated operating conditions are presented in Table 5.4 and 5.8. The results obtained from the PLECS and MATLAB models for the Semikron module are comparable to those from the Semikron simulation tool ,confirming that the developed loss model accurately captures the inverter losses and thermal performance under rated conditions. Indicates that the developed loss model effectively captures the inverter losses for the Semikron module.

Table 5.4: Power losses of IGBT and diode for Semikron module.

Loss Type	**MATLAB**	**Semikron Tool**	**PLECS**
IGBT Conduction Loss [W]	657.60	659.45	660.483
IGBT Switching Loss [W]	879.7	883.7	880.3
Diode Conduction Loss [W]	262.20	37.2054	43.4
Diode Switching Loss [W]	175.50	167.17	178.80

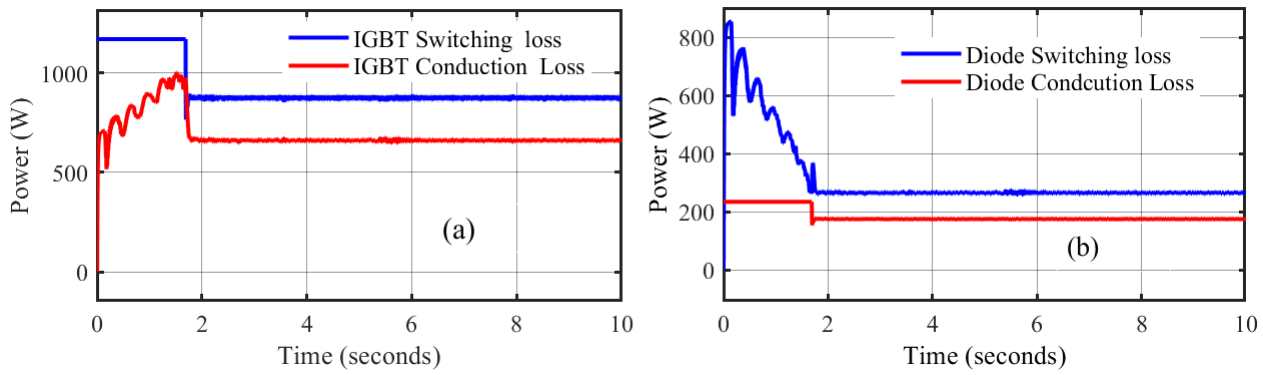

Figure 5.8: Conduction and switching loss analysis of the Semikron module under rated operating condition (1800 rpm) using SPWM: (a) IGBT Conduction and switching loss (b) Diode conduction and switching loss.

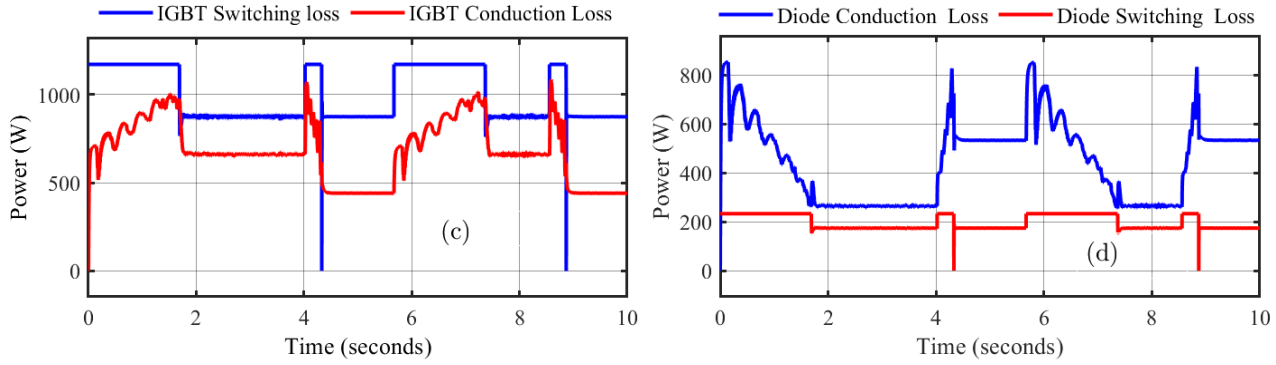

Figure 5.9: Transient conduction and switching loss analysis of the Semikron module under SPWM control: (c) IGBT conduction and switching losses; (d) Diode conduction and switching losses.

5.2.1.3 Losses From ABB Module

Table 5.5 presents the calculation of the power loss for the ABB module (1700 V, 800 A), including the conduction and switching losses. The result obtained from the PLECS and MATLAB models for the ABB module closely match those from the ABB simulation tool under rated operating conditions as shown figure 5.10. This shows that the developed loss model reliably captures the inverter losses of the ABB module,while Figure 5.11 demonstrates the transient condition clearly showing how the losses change as the reference speed gradually changes during acceleration, deceleration, and regenerative braking conditions.

5.2.1.4 Comparative Analysis of Inverter Losses Using SPWM

Table 5.6 shows, the conduction, the switching, and the total losses of the Infineon, Semikron, and ABB inverter modules were calculated using the proposed model. In comparison to the other modules, the ABB module indicates the lowest total losses, greater efficiency, and reduced thermal stress. These results shows the accuracy of the proposed loss model and suggest that the ABB inverter is the best suitable option for applications requiring optimized power loss and thermal management, provided that its voltage and current ratings are comparable to the other modules.

Table 5.5: Power Losses of IGBT and Diode for ABB-IGBT1700V800A .

Loss Type	MATLAB	ABB Tool	PLECS
IGBT Conduction Loss [W]	120.2	215.45	123.94
IGBT Switching Loss [W]	470.3	470.3383	468.938
Diode Conduction Loss [W]	29.22	34.2054	27.5
Diode Switching Loss [W]	230.9	232.67	234.67

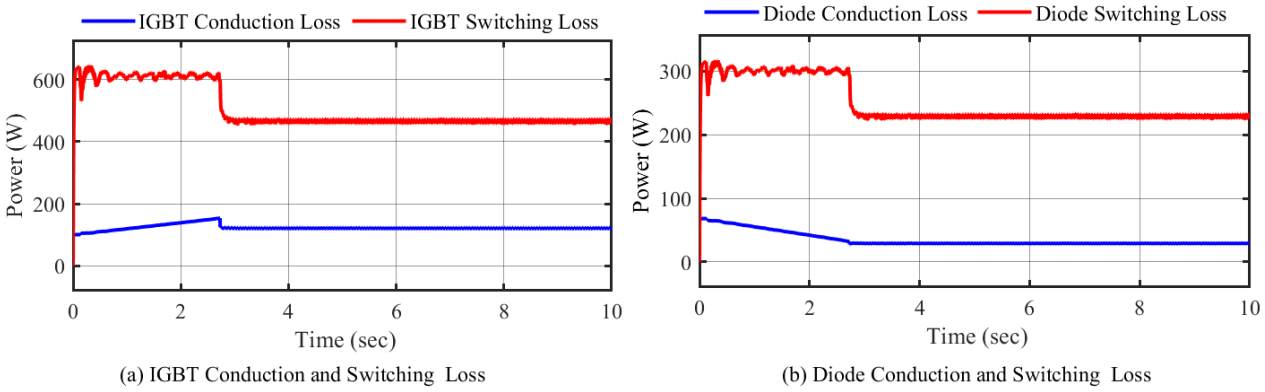

Figure 5.10: Conduction and switching loss analysis of ABB Module (a) IGBT Conduction and switching loss. (b) Diode conduction and switching loss.

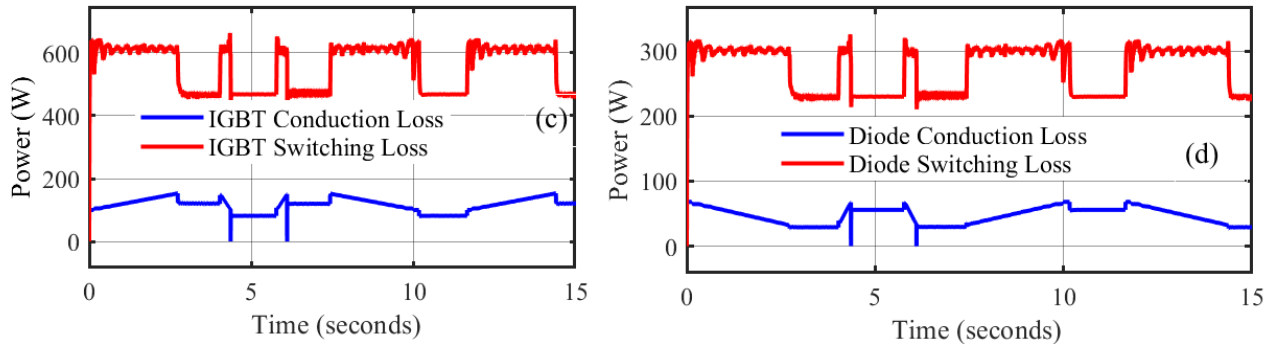

Figure 5.11: Conduction and switching loss analysis of the ABB module under transient conditions: (a) IGBT conduction and switching loss, (b) Diode conduction and switching loss.

Table 5.6: Comparison of Conduction ,Switching and total losses for the three inverter types.

Inverter Type	Conduction Loss	Switching Loss	Total Loss
Infineon	721.12W	722.98W	1981.06W
Semikron	919.06W	923.50W	1981.06W
ABB	149.42W	701.2W	850.62W

5.2.2 Losses in SVPWM

The power losses of Infineon, Semikron, and ABB inverter modules under the SVPWM strategy are analyzed, focusing on the losses of both the IGBT and diode. The detailed loss data for each module is provided in Tables 5.7, 5.8, and 5.9, respectively.

5.2.2.1 Losses From Infenion-Module

The power loss values, calculated using analytical equations as mentioned chapter 4, are summarized in Table 5.7 and figure 5.10. Figure 5.12 indicates the power losses for the IGBT and diode in terms of conduction and switching losses, with values derived using MATLAB / SIMULINK, a formula based approach, and PLECS. The results indicate that the PLECS and MATLAB models are approximately equivalent to the IOPSIM showing the accuracy of the introduced models.

Table 5.7: Power losses of IGBT and diode for Infenion module.

Loss Type	**MATLAB**	**IPOSIM**	**PLECS**
IGBT Conduction Loss [W]	84.43	78.45	83.483
IGBT Switching Loss [W]	124.83	122.8383	126.3383
Diode Conduction Loss [W]	7.2054	7.2054	7.2054
Diode Switching Loss [W]	45.67	38.67	52.67

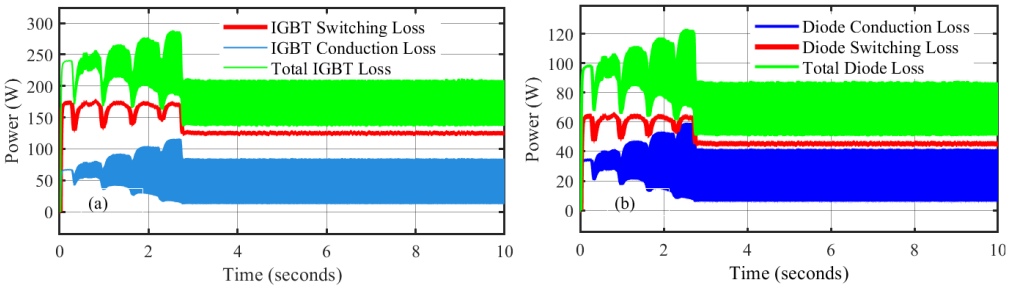

Figure 5.12: Conduction and switching losses of the Infineon module: (a) IGBT conduction and switching loss; (b) diode conduction and switching loss.

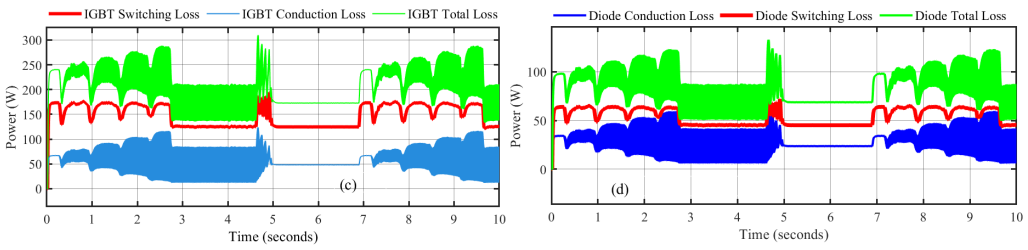

Figure 5.13: Conduction and switching loss analysis of the Infineon module under transient conditions: (a) IGBT conduction and switching loss, (b) Diode conduction and switching loss.

5.2.2.2 Losses From Semikron-Module

The power losses of the IGBT and diode for the Semikron module are presented in Table 5.8 and Figure 5.21.The analysis shows that switching losses, especially from the diode, make up a significant portion of the total power loss in the Semikron module. While conduction losses remain moderate, the higher switching losses suggest that thermal performance and efficiency could be affected in high-speed or high-frequency applications. This highlights the importance of evaluating switching behavior when selecting power modules for demanding conditions.

Table 5.8: Power losses of IGBT and diode for Semikron module per leg.

Loss Type	**MATLAB**	**Semikron Tool**	**PLECS**
IGBT Conduction Loss [W]	52.6	52.45	48.94
IGBT Switching Loss [W]	57.72	56.383	58.001
Diode Conduction Loss [W]	5.441	5.2054	4.503
Diode Switching Loss [W]	28.069	26.67	24.67

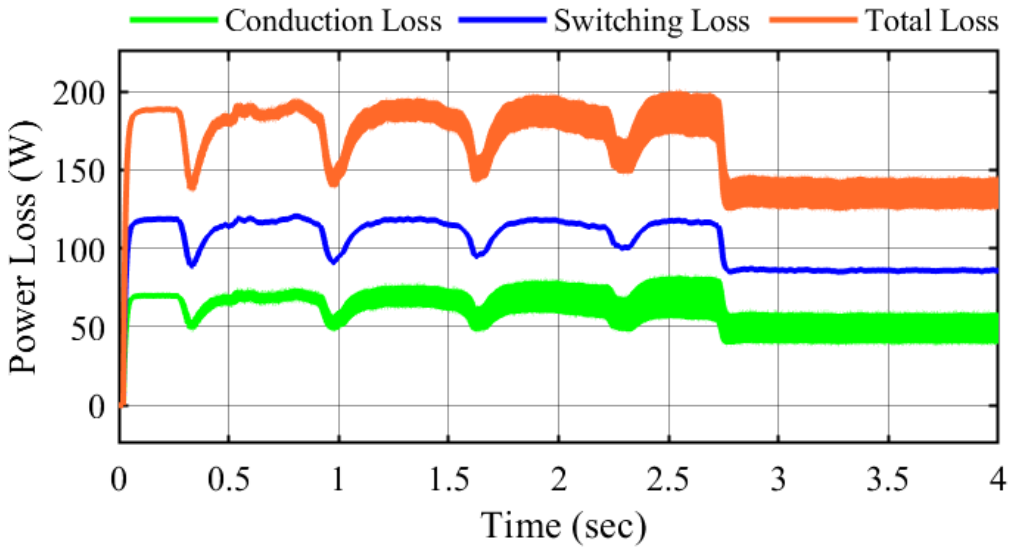

Figure 5.14: IGBT power loss in SVPWM based Semikron module.

5.2.2.3 Losses From ABB Module

The power losses of the ABB three-phase inverter module were analyzed by evaluating both conduction and switching losses of the IGBT and diode under SVPWM strategy. Table 5.9 and Figure 5.16 shows the results of the power loss for the ABB module, the losses for both the IGBT and the diode under SVPWM operation. The MATLAB model effectively captures dynamic switching behavior and current ripple effects, making it well-suited for transient analysis in transient-load conditions. The proposed SVPWM-based MATLAB model delivers accurate estimations for IGBT and diode losses, highlighting its capability to predict total power losses reliably. Overall, the MATLAB-based loss model proves to be a robust and accurate tool for inverter loss modeling and thermal analysis.

Table 5.9: Power losses of IGBT and diode for ABB module per leg.

Loss Type	MATLAB	ABB Tool	PLECS
IGBT Conduction Loss [W]	35.65	115.45	113.94
IGBT Switching Loss [W]	2.192	4.2054	3.65
Diode Conduction Loss [W]	64.53	64.2054	63.65
Diode Switching Loss [W]	166.4	162.67	174.67

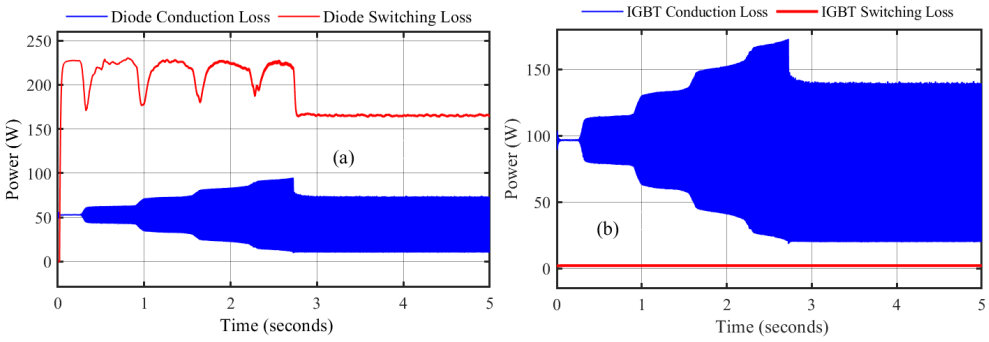

Figure 5.15: Power losses of the SVPWM-based ABB inverter module under rated conditions: (a) IGBT conduction and switching losses; (b) Diode conduction and switching losses.

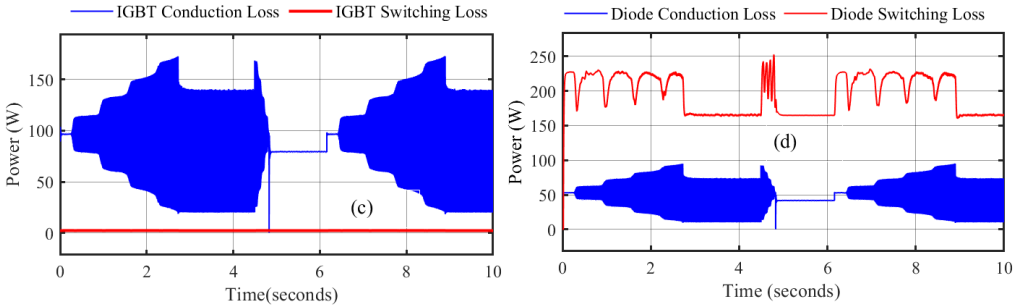

Figure 5.16: Transient power loss of the SVPWM-based ABB inverter module under transient condition : (a) IGBT conduction and switching loss (b) Diode conduction and switching loss

5.2.2.4 Comparative Analysis of IGBT-Based Inverter Losses in SVPWM

Semikron offers the lowest losses (143.83 W), ensuring high efficiency and minimal heat. Infenion provides a balance with moderate losses (262.1354W), while ABB are suitable for high-power applications, they have the highest losses (268.77 W), which require advanced cooling system . Figure 5.17 illustrates comparison of losses for different inverter types.

5.2.3 Overall Loss Comparison of all devices between SVPWM and SPWM

The analysis shows that SVPWM outperforms SPWM in reducing inverter losses across all tested modules. For the ABB module, conduction losses drop from 149.4 W (SPWM) to 100.2 W (SVPWM), a 32.9% reduction. Switching losses decrease from 701.13 W to 168.55 W

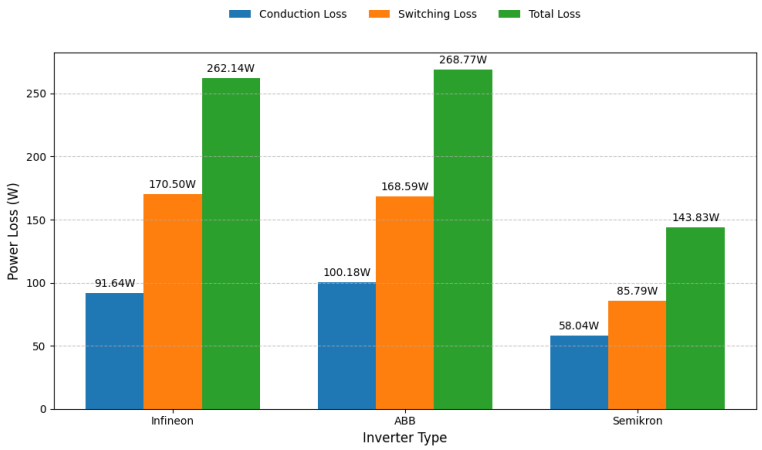

Figure 5.17: Comparison of losses for different inverter types.

(75.96% reduction), and total losses fall from 850.6 W to 268.7 W, an overall reduction of 68.4%. Therefore, SVPWM is the best choice for efficient and reliable inverter operation.

Figure 5.18 shows that SVPWM results in consistently lower overall power losses across all tested inverter modules. In contrast, Figure 5.19 shows a transient drop in SPWM losses around 2.8 s, likely due to load or control response, though the overall performance remains inferior.

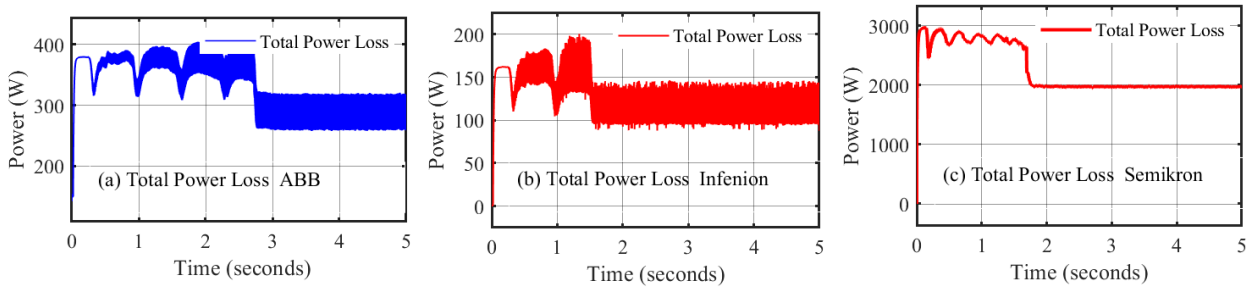

Figure 5.18: Comparison of total loss under SVPWM for (a) ABB, (b) Infineon, and (c) Semikron inverter modules.

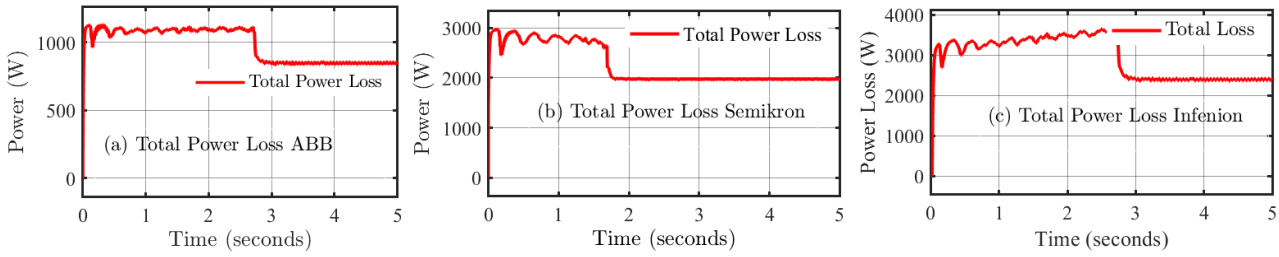

Figure 5.19: Comparison of power loss over time for three different inverter modules under SPWM with the same operating conditions: (a) ABB , (b) Semikron , and (c) Infineon inverter modules.

5.2.4 Three-Phase SiC-MOSFET Loss Analysis

In this Section, three-phase inverter conduction and switching losses with SiC MOSFETs operating under SPWM and SVPWM schemes are investigated. Further more,the performance comparison of Wolfspeed and Infineon SiC MOSFET modules is given .

5.2.4.1 Loss in SPWM

The conduction and switching losses of a three-phase inverter employing SiC MOSFETs under SPWM schemes are analyzed. A comparative evaluation is conducted for two SiC MOSFET modules (i.e Infineon and Wolfspeed). Simulation results for the SPWM strategy are summarized in Tables 5.10 and 5.11, detailing conduction and switching losses for both the MOSFET and its body diode.

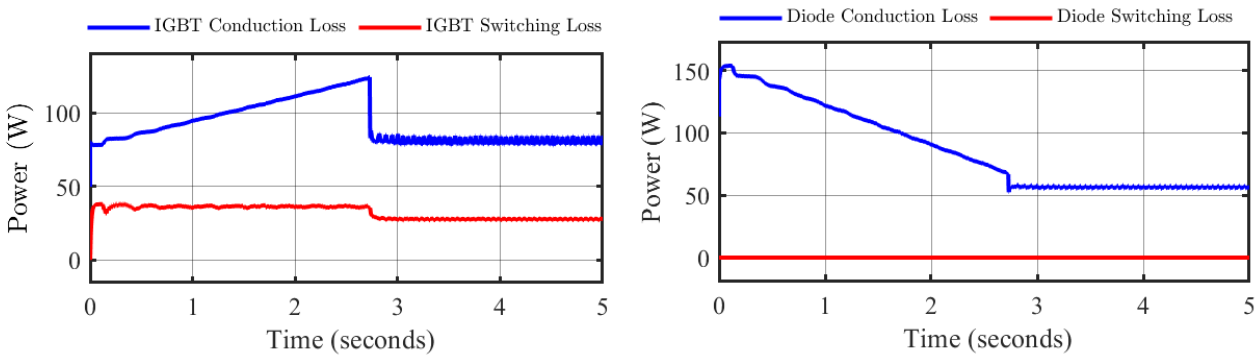

Figure 5.20: Losses of SiC-MOSFET and diode for Wolfspeed module.

Table 5.10: Power losses of SiC-MOSFET and Diode for Infineon IMW120R090M1H module.

Loss Type	**MATLAB**	**IPOSIM**	**PLECS**
SiC-MOSFET Conduction Loss [W]	83.48	21.45	83.483
SiC-MOSFET Switching Loss [W]	0.3383	0.383	0.5383
Diode Conduction Loss [W]	7.2054	7.54	7.0054
Diode Switching Loss [W]	42.67	38.67	32.67

Table 5.11: Power losses of SiC-MOSFET and Diode for Wolfspeed module.

Loss Type	**MATLAB**	**Formula**	**PLECS**
SiC-MOSFET Conduction Loss [W]	121.3	125.45	143.94
SiC-MOSFET Switching Loss [W]	98.6	92.3383	93.938
Diode Conduction Loss [W]	22.714	24.2054	22.5
Diode Switching Loss [W]	15.9	42.67	14.67

5.2.4.2 Losses in SVPWM

The simulation findings are shown in Tables 5.12 and 5.13.The MATLAB and PLECS simulator. The SiC MOSFET achieves 98.22% efficiency with lower conduction and switching losses, while the Si IGBT has 91.76% efficiency and higher losses, as shown Table 5.15 and Figure 5.22. These results highlight the superior performance of SiC technology in reducing power losses compared to traditional Si-IGBT devices.

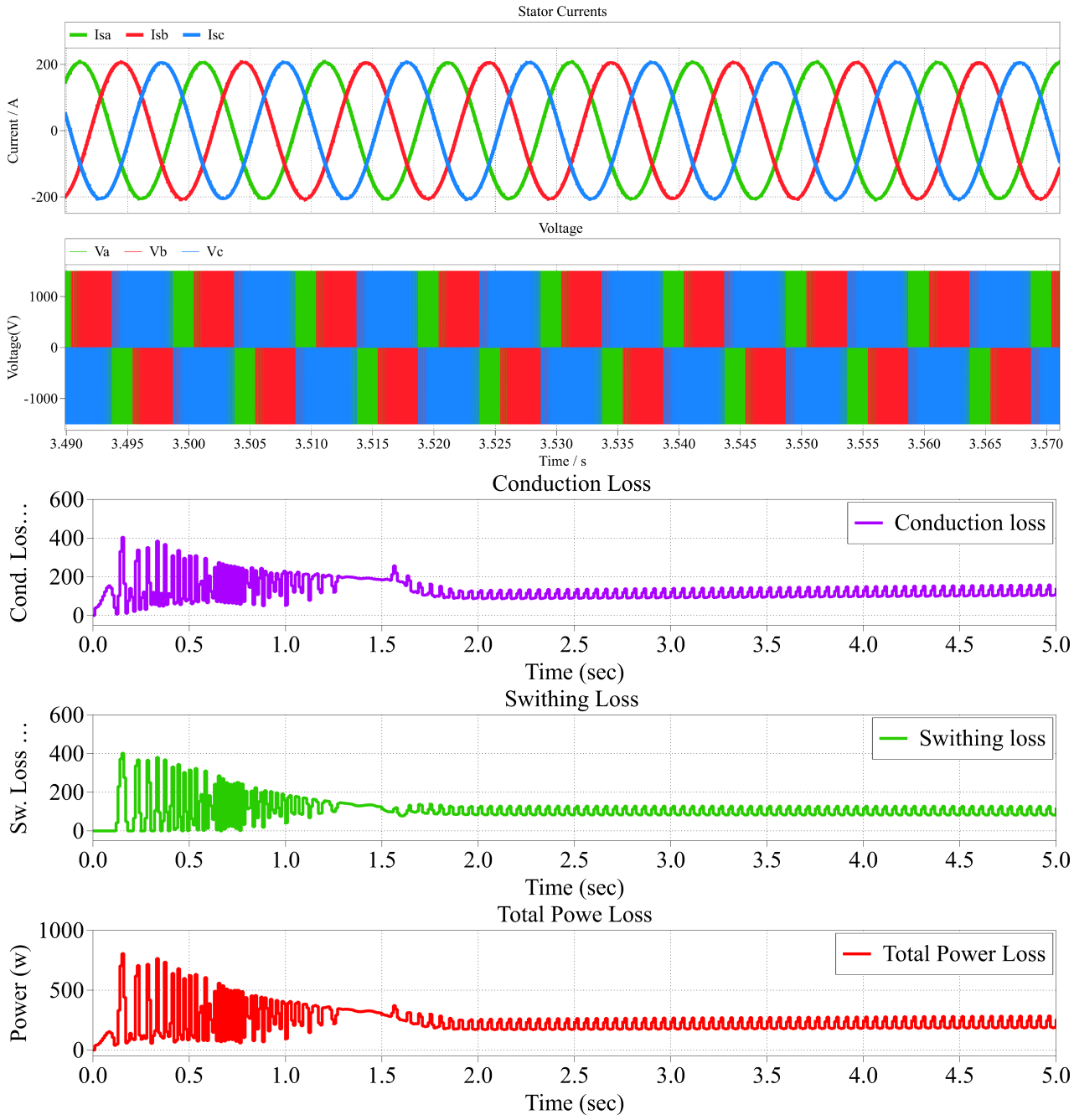

Figure 5.21: Losses of SiC-MOSFET and Diode for Infineon module.

Table 5.12: Power losses of SiC-MOSFET and Diode for Infineon IMW120R090M1H module.

Loss Type	**MATLAB**	**IPOSIM**	**PLECS**
SiC-MOSFET Conduction Loss [W]	83.48	81.45	83.483
SiC-MOSFET Switching Loss [W]	0.5383	0.5383	0.5383
Diode Conduction Loss [W]	7.2054	7.1054	7.0054
Diode Switching Loss [W]	42.67	42.67	42.67

Table 5.13: Power losses of SiC-MOSFET and Diode for Wolfspeed CAS300M17BM2 module.

Loss Type	**MATLAB**	**Wolfspeed**	**PLECS**
SiC-MOSFET Conduction Loss [W]	54.6	55.45	103.94
SiC-MOSFET Switching Loss [W]	2.183	2.3383	3.938
Diode Conduction Loss [W]	22.714	24.2054	22.5
Diode Switching Loss [W]	165.9	42.67	154.67

Table 5.14: Loss Comparison for Wolfspeed with SPWM vs. SVPWM .

Loss Type	**SPWM [W]**	**SVPWM [W]**
SiC-MOSFET Conduction Loss	121.3	54.6
SiC-MOSFET Switching Loss	98.6	2.183
Diode Conduction Loss	22.714	22.714
Diode Switching Loss	15.9	165.9
Total Loss	**258.514**	**245.397**

5.3 Impact of Modulation Index on Power Losses, Efficiency, and THD

This section explores the influence of the modulation index (MI) on critical inverter performance metrics, including power losses, efficiency, and Total Harmonic Distortion (THD). A comparative analysis of SPWM and SVPWM is conducted to evaluate their respective advantages under varying MI conditions.

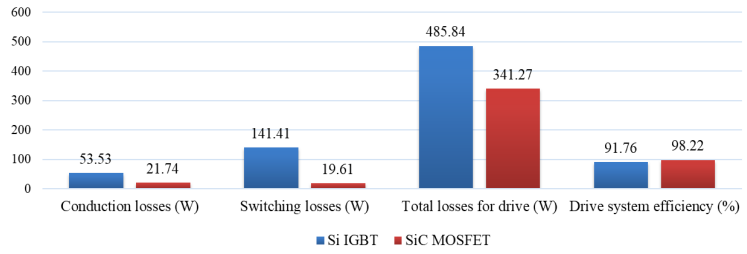

Figure 5.22: Comparison of losses and efficiency between Si-IGBT and SiC-MOSFET.

Figure 5.22 shows the efficiency trend across the modulation index. It can be understood that both SPWM and SVPWM maintain high efficiency. However,the SVPWM consistently shows superior performance. Besides,SVPWM has:

✓ Better DC Bus utilization

✓ Lower Harmonic distortion

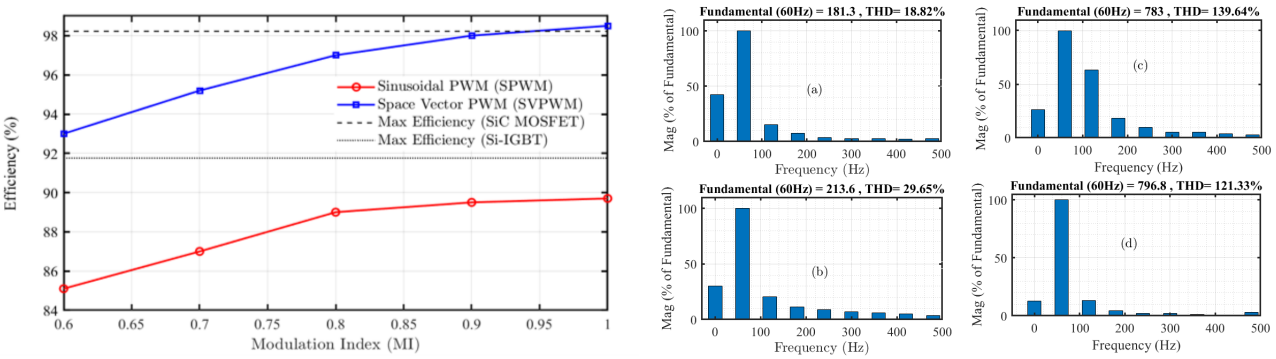

Figure 5.23: Efficiency Vs Modulation Index and THD analysis for SVPWM (a,d) and SPWM (b,c) of Infineon inverter module using FFT analysis under rated conditions.

A further investigation revealed that the performance of three-phase inverters in traction drive systems is greatly impacted by Total Harmonic Distortion (THD).

Figure 5.23 compares the total harmonic distortion (THD) levels of SPWM and SVPWM under rated conditions, based on FFT analysis of current and voltage waveforms obtained using MATLAB. The analysis shows that SVPWM provides improved harmonic performance, with THD values of 18.82% (current) and 121.33% (voltage), compared to 29.65% and 139.64% in SPWM respectively. According to the analysis done with MATLAB/Simulink, the following key effects are observed:

- ✓ Speed Regulation- SVPWM offers better speed control and lower THD compared to SPWM.
- ✓ Efficiency Loss and Power Dissipation- THD increases power losses by introducing additional harmonic currents.

Therefore, SiC MOSFETs demonstrate superior efficiency (98.22%) compared to Si-IGBTs (91.76%) under rated (steady-state) operating conditions, primarily due to reduced total harmonic distortion (THD) and lower thermal stress.

Table 5.15: Comparison of losses and efficiency for SiC-MOSFET and Si-IGBT .

Parameter	**Si IGBT**	**SiC MOSFET**
Conduction losses (W)	53.53	21.74
Switching losses (W)	141.41	19.61
Total losses for drive (W)	485.84	341.27
Drive system efficiency (%)	91.76	98.22

5.3.1 Junction Temperature Analysis in SVPWM and SPWM-Based Inverters.

IGBTs exhibit higher junction temperatures than SiC MOSFETs due to greater conduction and switching losses, lower thermal conductivity, and slower heat dissipation. Figure 5.25 compares the junction temperature waveforms of IGBT-based inverters using SPWM and SVPWM

for Semikron, ABB, and Infineon modules. SPWM results in higher and more fluctuating temperatures. In contrast, Figures 5.25a-c shows that SVPWM significantly reduces peak junction temperatures and ensures more stable thermal behavior across all modules.

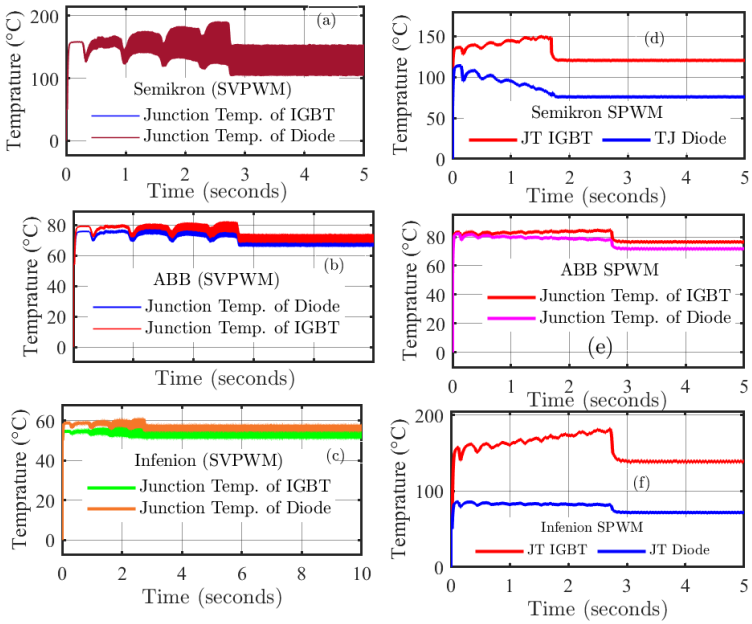

Figure 5.24: Comparison of IGBT junction temperature waveforms in SVPWM and SPWM .

As shown in Figure 5.25, the junction temperature (T_j) of the SiC MOSFETs remains well below their maximum rated limits (150–175 °C), as well as the Si-IGBT reference value (170 °C). Furthermore, the SVPWM strategy yields a significantly lower operating T_j ($\approx$ 75 °C) compared to the SPWM strategy ($\approx$ 120 °C) across both manufacturers.

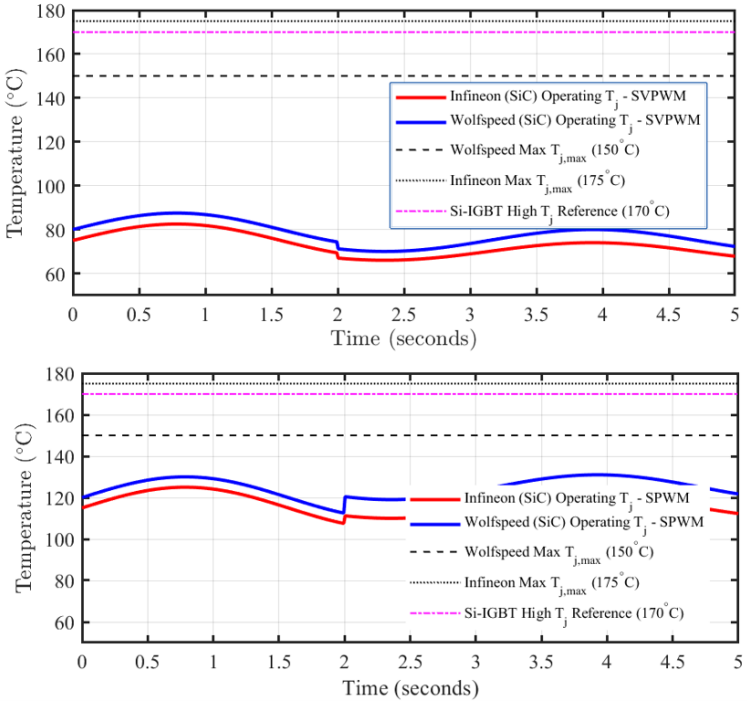

Figure 5.25: Comparison of SiC junction temperature waveforms in SVPWM and SPWM .

Chapter 6

Conclusion and Recommendations

6.1 Conclusion

This thesis conducted a comprehensive investigation into semiconductor losses in three-phase traction inverters, focusing on Si-IGBTs, freewheeling diodes (FWDs), and SiC-MOSFETs. The main objective was to develop a realistic analytical model for estimating conduction and switching losses and to evaluate the performance of different power modules under high-power operating conditions. The study considered a 190 kW inverter with a 1500 V DC-link voltage and a rated speed of 1800 rpm, analyzing both Sinusoidal PWM (SPWM) and Space Vector PWM (SVPWM) strategies.

A versatile analytical model was developed that combines a piecewise-linear approximation for switching losses with a third-order harmonic approximation for conduction losses. Unlike device-specific commercial tools, the proposed model guides a wide range of semiconductor devices, enabling consistent and comparative loss evaluation. Validation was carried out using MATLAB/Simulink, PLECS, and comparison with commercial tools as Semikron's SemiSel-V5, ABB SEMIS Simulation Tool, and Infineon's CIPM. The model closely matches commercial tools in accuracy. Deviations were minimal: for example, Infineon modules, conduction and switching losses differed by less than 0.5%, while for Semikron modules, switching losses differed by less than 0.5% and conduction losses by 32.03%.

The study highlighted the superior performance of SiC-MOSFETs over Si-IGBTs. SiC-based inverters using Infineon and Wolfspeed modules achieved higher efficiency and lower losses compared to Si-IGBT modules from Infineon, ABB, and Semikron. Thermal modeling confirmed that SiC-MOSFET modules maintain lower maximum junction temperatures than Si-IGBT modules, indicating improved thermal performance and reliability across operating points.

The analysis of PWM strategies demonstrated that SVPWM outperforms SPWM, providing better voltage utilization, lower total harmonic distortion, and enhanced inverter performance. Additionally, the study showed that turn-on gate resistances significantly affect switching losses, emphasizing the importance of optimized gate control. Comparative evaluation of different modules revealed performance variations due to manufacturer-specific characteristics, highlighting the importance of considering both electrical and thermal properties when selecting power devices.

A key limitation of this research is that validation was only through simulations and com-

mercial tools, requiring experimental testing for broader real-world conditions.

In conclusion, this research developed and validated a flexible, accurate, and broadly applicable analytical model for semiconductor loss estimation in traction inverters. The model provides a robust framework for comparing different semiconductor devices and modulation strategies. The results confirm that SiC-MOSFETs, combined with SVPWM, are the preferred solution for high-power traction applications, offering higher efficiency, lower losses, and improved thermal performance. This work contributes to the field by enabling systematic, multi-faceted evaluation of inverter design choices, supporting the development of efficient, thermally robust, and sustainable electric traction systems.

6.2 Recommendations and Future Work

The comprehensive investigation conducted in this thesis, which successfully developed and validated a robust analytical loss model and confirmed the superior efficiency of SiC-MOSFETs (98.22%) and the enhanced harmonic performance of SVPWM, establishes several high-priority directions for subsequent research and development in electric traction drives.

6.2.1 Experimental Validation of Core Models and Devices

Future work must prioritize closing the gap between simulation and practice by focusing on the following experimental validation steps:

1. **Precision Loss Model Validation:** Conduct **rigorous experimental tests** on a prototype SiC traction inverter. This is mandated to empirically validate the developed analytical loss model, specifically verifying the simulated 0.5% loss deviation observed against commercial tools under dynamic thermal and current load cycles representative of railway operation.

2. **GaN Feasibility Study for Traction:** Perform a targeted comparative analysis of GaN devices against SiC technology for 1500V/MW traction applications. This research must focus on quantifying the achievable power density increase and total system efficiency gain derived from GaN's high-frequency switching capability.

6.2.2 Implementation of Intelligent and Adaptive Control Strategies

Building upon the verified performance of the SiC/SVPWM platform, the research must advance toward intelligent, self-optimizing control systems:

1. **Adaptive Machine Learning Control:** Development and validation of a Machine Learning (ML)-based adaptive controller is required. The controller must utilize real-time input from the unified loss model to autonomously adjust the modulation index and switching frequency, ensuring the inverter perpetually operates at its peak efficiency point despite fluctuations in load or DC-link voltage.

2. **Digital Twin and Predictive Diagnostics:** The confirmed accuracy of the analytical model must be leveraged to establish a high-fidelity digital twin of the traction drive. This system will enable real-time semiconductor degradation tracking and facilitate the implementation of Predictive Maintenance (PdM) protocols, significantly enhancing system reliability.

References

[1] Wesam Taha. Design and Control of a 100 kW SiC-Based Six-Phase Traction Inverter for Electric Vehicle Applications. PhD thesis, 2023.

[2] Noah Odion and Honest Jimu. Comparative analysis of silicon carbide (sic) mosfets and silicon igbts in electric vehicles.

[3] Bai Baodong and Chen Dezhi. Inverter igbt loss analysis and calculation. In 2013 IEEE International Conference on Industrial Technology (ICIT), pages 563–569. IEEE, 2013.

[4] Josias W Makhubele and Kingsley A Ogudo. Analysis on basics of modulation techniques for ac drive on efficiency improvements. 2020 IEEE PES/IAS PowerAfrica, pages 1–5, 2020.

[5] K. Nagasai and T. Jyothsna. Harmonic analysis and application of pwm techniques for three-phase inverter. International Research Journal of Engineering and Technology (IRJET), 3, 2016.

[6] MK Giridharan. Pmsm field oriented control using svpwm for control moment gyroscope (cmg).

[7] A. Acquaviva and T. Thiringer. Energy efficiency of a sic mosfet propulsion inverter accounting for the mosfet's reverse conduction and the blanking time. In 2017 19th European Conference on Power Electronics and Applications (EPE'17 ECCE Europe), pages P–1. IEEE, 2017.

[8] V. Benda. Power semiconductors—state of art and future trends. In AIP Conference Proceedings, volume 1337, pages 16–24. AIP, 2011.

[9] K. Wolski, M. Zdanowski, and J. Rabkowski. High-frequency sic-based inverters with input stages based on quasi-z-source and boost topologies—experimental comparison. IEEE Transactions on Power Electronics, 34:9471–9478, 2019.

[10] Takayuki Miyajima, Hiroshi Fujimoto, and Masami Fujitsuna. A precise model-based design of voltage phase controller for ipmsm. IEEE Transactions on Power Electronics, 28(12):5655–5664, 2013.

[11] Mihai Cheles and H Sammoud. Sensorless field oriented control (foc) of an ac induction motor (acim). Microchip Technology Inc, pages 1–34, 2008.

[12] R. Künzi. Thermal design of power electronic circuits. Technical report, CERN.

[13] Ahcene Bouzida, Radia Abdelli, and M'hamed Ouadah. Calculation of igbt power losses and junction temperature in inverter drive. In 2016 8th International Conference on Modelling, Identification and Control (ICMIC), pages 768–773. IEEE, 2016.

[14] Keliang Zhou and Danwei Wang. Relationship between space-vector modulation and three-phase carrier-based pwm: a comprehensive analysis [three-phase inverters]. IEEE transactions on industrial electronics, 49(1):186–196, 2002.

[15] Yuan Zhu, Mingkang Xiao, Xiezu Su, Gang Yang, Ke Lu, and Zhihong Wu. Modeling of conduction and switching losses for igbt and fwd based on svpwm in automobile electric drives. Applied Sciences, 10(13):4539, 2020.

[16] Abebe Teklu Woldegiorgis, Xinglai Ge, Huiming Wang, and Yun Zuo. An active flux estimation in the estimated reference frame for sensorless control of ipmsm. IEEE Transactions on Power Electronics, 37(8):9047–9060, 2022.

[17] Parvathy Thampi Mooloor Sahridayan and Raghavendra Gopal. Modeling and analysis of field-oriented control based permanent magnet synchronous motor drive system using fuzzy logic controller with speed response improvement. International Journal of Electrical and Computer Engineering (IJECE), 12(6):6010–6021, 2022.

[18] Daniel M Springmann, TM Jahns, and RD Lorenz. Inverter gate drive and phase leg development for 175° c operation. In 2008 IEEE Power Electronics Specialists Conference, pages 2152–2158. IEEE, 2008.

[19] A. Elasser, T. P. Chow, et al. Silicon carbide benefits and advantages for power electronics circuits and systems. Proceedings of the IEEE, 90(6):969–986, 2002.

[20] M. Vujacic, O. Dordevic, and G. Grandi. Evaluation of dc-link voltage switching ripple in multiphase pwm voltage source inverters. IEEE Transactions on Power Electronics, 35:3478–3490, 2020.

[21] UnitedSiC. Unitedsic simulator documentation. Accessed January 2025.

[22] Infineon Technologies. Cipos design guide and simulation tools. Accessed January 2025.

[23] Bonimira Doykova. Motor-drive system efficiency internal calculation tool and product information database audit based on iec 61800-9-2 standard. 2019.

[24] Amir Babaki, Mohammad Sadegh Golsorkhi, Thomas Ebel, Nicklas Christensen, Stefan Behrendt, and Jesco Beyer. Model design for evaluating oscillating voltage characteristic in hybrid-switch t-type converter considering parasitics. In 2024 IEEE Transportation Electrification Conference and Expo (ITEC), pages 1–6. IEEE, 2024.

[25] Semikron. Semisel-v5 simulation tool documentation. Accessed January 2025.

[26] Doğan YILDIRIM. All sic traction converter for light rail transportation systems: Design methodology and development of a 500-900 vdc, 165 kva prototype. 2021.

[27] B Jayant Baliga. Fundamentals of power semiconductor devices. Springer Science & Business Media, 2010.

[28] Franz Christoph Zach. Losses in pwm inverters using igbts. ETH Zurich & Vienna University of Technology, 2025. Ensure to add journal details if available.

[29] Ke Li and Yi Wang. Maximum torque per ampere (mtpa) control for ipmsm drives based on a variable-equivalent-parameter mtpa control law. IEEE Transactions on Power Electronics, 34(7):7092–7102, 2018.

[30] Johann Wolfgang Kolar. Modelling, simulation and investigation of losses and ripple in traction inverters. 2021. Include the journal name and other relevant details if available.

[31] M. Meyer and J. Bocker. Optimum control for interior permanent magnet synchronous motors (ipmsm) in constant torque and flux weakening range. In 2006 12th International Power Electronics and Motion Control Conference, pages 282–286. IEEE, 2006.

[32] B. Wang, J. Cai, X. Du, and L. Zhou. Review of power semiconductor device reliability for power converters. CPSS Transactions on Power Electronics and Applications, 2(1):33–41, 2017.

[33] L. H. Opsahl. Design and testing of voltage source inverter and motor control system for electric vehicle. Master's thesis, Norwegian University of Science and Technology, 2015. Online; accessed June 2025.

[34] Mohamed Z Youssef, Konrad Woronowicz, Kunwar Aditya, Najath Abdul Azeez, and Sheldon S Williamson. Design and development of an efficient multilevel dc/ac traction inverter for railway transportation electrification. IEEE Transactions on power Electronics, 31(4):3036–3042, 2015.

[35] Luciano FS Alves, Ruan CM Gomes, Pierre Lefranc, Raoni De A Pegado, Pierre-Olivier Jeannin, Benedito A Luciano, and Filipe V Rocha. Sic power devices in power electronics: An overview. In 2017 Brazilian Power Electronics Conference (COBEP), pages 1–8. IEEE, 2017.

[36] Ming Liu, Anthony Coppola, Muhammad Alvi, and Mohammad Anwar. Comprehensive review and state of development of double-sided cooled package technology for automotive power modules. IEEE Open Journal of Power Electronics, 3:271–289, 2022.

[37] M. Nawaz and K. Ilves. Replacing si to sic: Opportunities and challenges. In 2016 46th European Solid-State Device Research Conference (ESSDERC), pages 472–475. IEEE, 2016.

[38] N. Oswald, P. Anthony, N. McNeill, and B. H. Stark. An experimental investigation of the tradeoff between switching losses and emi generation with hard-switched all-si, si-sic, and all-sic device combinations. IEEE Transactions on Power Electronics, 29:2393–2407, 2014.

[39] Jose Jacob. High-speed control issues and advanced self-commissioning techniques for Permanent Magnet Synchronous Motors. PhD thesis, Free University of Bozen-Bolzano.

[40] Jacek Rabkowski and Tadeusz Płatek. Comparison of the power losses in 1700v si igbt and sic mosfet modules including reverse conduction. In 2015 17th European Conference on Power Electronics and Applications (EPE'15 ECCE-Europe), pages 1–10. IEEE, 2015.

[41] Lucas Barroso Spejo, Innocent Akor, Munaf Rahimo, and Renato Amaral Minamisawa. Life-cycle energy demand comparison of medium voltage silicon igbt and silicon carbide mosfet power semiconductor modules in railway traction applications. Power Electronic Devices and Components, 6:100050, 2023.

[42] Junhyuk Lee and Jung-Wook Park. Selection of pwm methods for common-mode voltage and dc-link capacitor current reduction of three-phase vsi. IEEE Transactions on Industry Applications, 59(1):1064–1076, 2022.

[43] S-K Han, J-Y Lee, G-W Moon, and M-J Youn. Igbt-based cost-effective energy-recovery circuit for plasma display panel. IEEE Transactions on Industrial Electronics, 53(5):1546–1554, 2006.

[44] K. Koseki, Y. Yonezawa, T. Mizushima, S. Matsunaga, Y. Iizuka, and H. Yamaguchi. Dynamic behavior of a medium-voltage n-channel sic-igbt with ultrafast switching performance of 300 kv/µs. IEEE Transactions on Industry Applications, 54:3558–3565, 2018.

[45] Yongchang Zhang, Hao Jiang, and Haitao Yang. Model predictive control of pmsm drives based on general discrete space vector modulation. IEEE Transactions on Energy Conversion, 36(2):1300–1307, 2020.

[46] Shalini Vashishtha and KR Rekha. A survey: Space vector pwm (svpwm) in 3φ voltage source inverter (vsi). International Journal of Electrical and Computer Engineering (IJECE), 8(1):11–18, 2018.

[47] Amit Kumar Gupta and Ashwin M Khambadkone. A space vector pwm scheme for multilevel inverters based on two-level space vector pwm. IEEE Transactions on industrial electronics, 53(5):1631–1639, 2006.

[48] Bai Baodong and Chen Dezhi. Inverter igbt loss analysis and calculation. In 2013 IEEE International Conference on Industrial Technology (ICIT), pages 563–569. IEEE, 2013.

[49] Anis Shahida Niza Mokhtar, BBI Reaz, M Maruffuzaman, and Mohammad Alauddin Mohammad Ali. Inverse park transformation using cordic and phase-locked loop. Rev. Roum. Sci. Techn.–Electrotechn. et Energ, 57(4):422–431, 2012.

[50] VS Veena, Sadasivan Achari, MH Ravichandran, and RP Praveen. Vector control of three phase pmsm drive using power transformations for future spacecraft application. In 2014 International Conference on Circuits, Power and Computing Technologies [ICCPCT-2014], pages 313–319. IEEE, 2014.

[51] D. Han, S. Li, Y. Wu, W. Choi, and B. Sarlioglu. Comparative analysis on conducted cm emi emission of motor drives: Wbg versus si devices. IEEE Transactions on Power Electronics, 64:8353–8363, 2017.

[52] M. Meyer, T. Grote, and J. Bocker. Direct torque control for interior permanent magnet synchronous motors with respect to optimal efficiency. In 2007 European Conference on Power Electronics and Applications, pages 1–9. IEEE, 2007.

[53] Diego Bellan. Clarke transformation solution of asymmetrical transients in three-phase circuits. Energies, 13(19):5231, 2020.

[54] P Ramesh, M Umavathi, C Bharatiraja, G Ramanathan, and Sivaprasad Athikkal. Development of a pmsm motor field-oriented control algorithm for electrical vehicles. Materials Today: Proceedings, 65:176–187, 2022.

[55] Ting-ting Liu, Yu Tan, Gang Wu, and Shu-mao Wang. Simulation of pmsm vector control system based on matlab/simulink. In 2009 international conference on measuring technology and mechatronics automation, volume 2, pages 343–346. IEEE, 2009.

[56] Mohammed Hassan Ahmed, Mingyu Wang, Muhammad Arshad Shehzad Hassan, and Irfan Ullah. Power loss model and efficiency analysis of three-phase inverter based on sic mosfets for pv applications. IEEE Access, 7:75768–75781, 2019.

[57] Wengliang Liu and Pengfei Xu. Design of pmsm speed control system based on simulink model. In IOP Conference Series: Materials Science and Engineering, volume 569, page 042004. IOP Publishing, 2019.

[58] Shaowei Ren, Yifan Wang, Jichao Ma, Haibin Xie, Haowen Jiang, and Xueqing Wang. Position sensorless control for pmsm drives without dc-link voltage sensor. In 2024 IEEE 10th International Power Electronics and Motion Control Conference (IPEMC2024-ECCE Asia), pages 2326–2331. IEEE, 2024.

[59] F. Yang, L. Wang, H. Kong, M. Zhu, X. Liu, X. Lu, M. Qin, T. Zhang, Y. Gan, and L. Jia. Compact-interleaved packaging method of power module with dynamic characterization of 4h-sic mosfet and development of power electronic converter at extremely high junction temperature. IEEE Transactions on Power Electronics, 38:417–434, 2023.

[60] S. Yin, K. J. Tseng, R. Simanjorang, and P. Tu. Experimental comparison of high-speed gate driver design for 1.2-kv/120-a si igbt and sic mosfet modules. IET Power Electronics, 10(9):979–986, 2017.

[61] Waqar Khan. Torque maximizing and flux weakening control of synchronous machines. 2016.

[62] Isao Takahashi and Youichi Ohmori. High-performance direct torque control of an induction motor. IEEE transactions on industry applications, 25(2):257–264, 1989.

[63] Jae-Hyun Kim, Dong-Min Kim, Young-Hoon Jung, and Myung-Seop Lim. Design of ultra-high-speed motor for fcev air compressor considering mechanical properties of rotor materials. IEEE Transactions on Energy Conversion, 36(4):2850–2860, 2021.

[64] Mesut Uğur, Hakan Saraç, and Ozan Keysan. Comparison of inverter topologies suited for integrated modular motor drive applications. In 2018 IEEE 18th International Power Electronics and Motion Control Conference (PEMC), pages 524–530. IEEE, 2018.

[65] B. Ozpineci and L. M. Tolbert. Characterization of sic schottky diodes at different temperatures. IEEE Power Electronics Letters, 1(2):54–57, 2003.

[66] Michael H Bierhoff and Friedrich W Fuchs. Semiconductor losses in voltage source and current source igbt converters based on analytical derivation. In 2004 IEEE 35th Annual Power Electronics Specialists Conference (IEEE Cat. No. 04CH37551), volume 4, pages 2836–2842. IEEE, 2004.

[67] Ken Berringer, Jeff Marvin, and Philippe Perruchoud. Semiconductor power losses in ac inverters. In IAS'95. Conference Record of the 1995 IEEE Industry Applications Conference Thirtieth IAS Annual Meeting, volume 1, pages 882–888. IEEE, 1995.

[68] Faisal Amin, E Bin Sulaiman, Wahyu Mulyo Utomo, Hassan Ali Soomro, Mahyuzie Jenal, and Rajesh Kumar. Modelling and simulation of field oriented control based permanent magnet synchronous motor drive system. Indonesian Journal of Electrical Engineering and Computer Science, 6(2):387–395, 2017.

[69] Chunyan Lai, Guodong Feng, K Lakshmi Varaha Iyer, Kaushik Mukherjee, and Narayan C Kar. Genetic algorithm-based current optimization for torque ripple reduction of interior pmsms. IEEE Transactions on Industry Applications, 53(5):4493–4503, 2017.

[70] Chen Jie and Guo Yanling. Research on control strategy of the electric power steering system for all-terrain vehicles based on model predictive current control. Mathematical Problems in Engineering, 2021(1):6642042, 2021.

[71] Ke Li and Yi Wang. Maximum torque per ampere (mtpa) control for ipmsm drives based on a variable-equivalent-parameter mtpa control law. IEEE Transactions on Power Electronics, 34(7):7092–7102, 2018.

[72] Sungmin Kim, Young-Doo Yoon, Seung-Ki Sul, and Kozo Ide. Maximum torque per ampere (mtpa) control of an ipm machine based on signal injection considering inductance saturation. IEEE Transactions on Power Electronics, 28(1):488–497, 2012.

[73] Ke Li and Yi Wang. Maximum torque per ampere (mtpa) control for ipmsm drives using signal injection and an mtpa control law. IEEE Transactions on Industrial Informatics, 15(10):5588–5598, 2019.

[74] Kahyun Lee and Jung-Ik Ha. Dynamic decoupling control method for pmsm drive with cross-coupling inductances. In 2017 IEEE Applied Power Electronics Conference and Exposition (APEC), pages 563–569. IEEE, 2017.

[75] Zhiping Chen, Liqiang Yuan, Zhengming Zhao, and Xiaoying Sun. Power losses in two- and three-level three phase photovoltaic inverters equipped with igbts. In 2012 15th International Conference on Electrical Machines and Systems (ICEMS), pages 1–6. IEEE, 2012.

[76] York C Gerstenmaier, Walter Kiffe, and Gerhard Wachutka. Combination of thermal subsystems modeled by rapid circuit transformation. In 2007 13th International Workshop on Thermal Investigation of ICs and Systems (THERMINIC), pages 115–120. IEEE, 2007.

[77] Qianming Xu, Fujun Ma, Zhixing He, Yandong Chen, Josep M Guerrero, An Luo, Yan Li, and Yufei Yue. Analysis and comparison of modular railway power conditioner for high-speed railway traction system. IEEE Transactions on Power Electronics, 32(8):6031–6048, 2016.

[78] X. Ding, M. Du, T. Zhou, H. Guo, C. Zhang, and F. Chen. Comprehensive comparison between sic-mosfets and si-igbts based electric vehicle traction systems under low speed and light load. Energy Procedia, 88:991–997, 2016.

[79] B Jayant Baliga. Trends in power semiconductor devices. IEEE Transactions on electron Devices, 43(10):1717–1731, 1996.

[80] Frede Blaabjerg, Ulrich Jaeger, and Stig Munk-Nielsen. Power losses in pwm-vsi inverter using npt or pt igbt devices. IEEE Transactions on Power Electronics, 10(3):358–365, May 1995.

[81] Arjun Sujeeth, Angelo Di Cataldo, Luigi Danilo Tornello, Mario Pulvirenti, Luciano Salvo, Angelo Giuseppe Sciacca, Giacomo Scelba, and Mario Cacciato. Power loss modelling and performance comparison of three-level gan-based inverters used for electric traction. Energies, 17(3):595, 2024.

[82] Xibo Yuan, Ian Laird, and Sam Walder. Opportunities, challenges, and potential solutions in the application of fast-switching sic power devices and converters. IEEE Transactions on Power Electronics, 36(4):3925–3945, 2020.

[83] P Chow Reddy and P Surya Narayana Reddy. Simplified digital waves and sinusoidal pulse width modulation for single phase inverter. Editorial Board, 8(5):77, 2019.

[84] Ken Berringer, Jeff Marvin, and Philippe Perruchoud. Semiconductor power losses in ac inverters. In IAS'95. Conference Record of the 1995 IEEE Industry Applications Conference Thirtieth IAS Annual Meeting, volume 1, pages 882–888. IEEE, 1995.

[85] Sheng Lin, Xiaotong Fang, Fei Lin, Zhen Yang, Xiaoyu Wang, and Zheyu Zhang. Lifetime prediction of igbt modules based on mission profiles in traction inverter application. In 2019 IEEE Vehicle Power and Propulsion Conference (VPPC), pages 1–6. IEEE, 2019.

[86] Jiaxi Hu, Wenye Liu, and Jinfeng Yang. Application of power electronic devices in rail transportation traction system. In 2015 IEEE 27th International Symposium on Power Semiconductor Devices & IC's (ISPSD), pages 7–12. IEEE, 2015.

[87] Thilo Bringezu and Jürgen Biela. Optimal design of integrated motor drives-comparison of topologies (2l/3l/modular), pwm variants, and switch technologies (si/sic/gan). In 2022 24th European Conference on Power Electronics and Applications (EPE'22 ECCE Europe), pages P–1. IEEE, 2022.

[88] Mohammed Hassan Ahmed, Mingyu Wang, Muhammad Arshad Shehzad Hassan, and Irfan Ullah. Power loss model and efficiency analysis of three-phase inverter based on sic mosfets for pv applications. IEEE Access, 7:75768–75781, 2019.

[89] Zhiwei Chen, Tingna Shi, Zhichen Lin, Zhiqiang Wang, and Xin Gu. Analysis and control of current harmonic in ipmsm field-oriented control system. IEEE Transactions on Power Electronics, 37(8):9571–9585, 2022.

[90] C. Mademlis and V. G. Agelidis. On considering magnetic saturation with maximum torque to current control in interior permanent magnet synchronous motor drives. IEEE Transactions on Energy Conversion, 16(3):246–252, 2001.

[91] Uwe Drofenik and Johann W Kolar. A general scheme for calculating switching-and conduction-losses of power semiconductors in numerical circuit simulations of power electronic systems. In Proc. IPEC, volume 5, pages 4–8. Citeseer, 2005.

[92] Alberto Berrueta, Idoia San Martin, Andoni Hernández, Alfredo Ursúa, and Pablo Sanchis. Electro-thermal modelling of a supercapacitor and experimental validation. Journal of Power Sources, 259:154–165, 2014.

[93] François Boige, Frédéric Richardeau, Stéphane Lefebvre, and Marc Cousineau. Sic power mosfet in short-circuit operation: Electro-thermal macro-modelling combining physical and numerical approaches with circuit-type implementation. Mathematics and Computers in Simulation, 158:375–386, 2019.

[94] Youmin Yu, Tien-Yu Tom Lee, and Victor Adrian Chiriac. Compact thermal resistor-capacitor-network approach to predicting transient junction temperatures of a power amplifier module. IEEE Transactions on Components, Packaging and Manufacturing Technology, 2(7):1172–1181, 2012.

[95] Gerhard K Wachutka. Rigorous thermodynamic treatment of heat generation and conduction in semiconductor device modeling. IEEE transactions on computer-aided design of integrated circuits and systems, 9(11):1141–1149, 1990.

[96] CC Lee and AL Palisoc. Thermal analysis of semiconductor devices. In Electrical Engineering Applications, pages 12–33. Springer, 1990.

[97] Cheng Qian, Amir Mirza Gheitaghy, Jiajie Fan, Hongyu Tang, Bo Sun, Huaiyu Ye, and Guoqi Zhang. Thermal management on igbt power electronic devices and modules. Ieee Access, 6:12868–12884, 2018.

[98] Yinquan Yu, Chenglong Liang, Dequan Zeng, Yiming Hu, and Jinwen Yang. Multi-objective optimization of ipmsm for electric vehicles based on the combinatorial surrogate model and the hierarchical design method. International Journal of Electrical Power & Energy Systems, 162:110245, 2024.

[99] Ibrahim M Abdelaziz, Yehia Sayed Mohamed, EG Shehata, and Ahmed A Zaki Diab. Comprehensive analysis of ipmsm drives with foc under different operating modes. Discover Applied Sciences, 7(4):1–38, 2025.

[100] J Carstensen, E Foca, S Keipert, H Föll, M Leisner, and A Cojocaru. New modes of fft impedance spectroscopy applied to semiconductor pore etching and materials characterization. physica status solidi (a), 205(11):2485–2503, 2008.

SKM400GB12T4

SEMITRANS®3

Fast IGBT4 Modules

SKM400GB12T4

Features

- $V_{CE(sat)}$ with positive temperature coefficient
- High short circuit capability, self limiting to 6 x Icnom
- Fast & soft inverse CAL diodes
- Large clearance (10 mm) and creepage distances (20 mm)
- Isolated copper baseplate using DBC Technology (Direct Copper Bonding)

Typical Applications

- AC inverter drives
- UPS
- Electronic welders at fsw up to 20 kHz

Remarks

- Case temperature limited to T_c = 125°C max, recomm. T_{op} = -40 ... +150°C, product rel. results valid for T_j = 150°

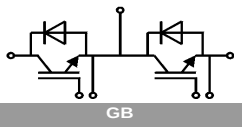

GB

Absolute Maximum Ratings				
Symbol	**Conditions**		**Values**	**Unit**
IGBT				
V_{CES}			1200	V
I_C	T_j = 175 °C	T_c = 25 °C	618	A
		T_c = 80 °C	475	A
I_{Cnom}			400	A
I_{CRM}	I_{CRM} = 3xI_{Cnom}		1200	A
V_{GES}			-20 ... 20	V
t_{psc}	V_{CC} = 800 V $V_{GE} \leq$ 15 V $V_{CES} \leq$ 1200 V	T_j = 150 °C	10	µs
T_j			-40 ... 175	°C
Inverse diode				
I_F	T_j = 175 °C	T_c = 25 °C	440	A
		T_c = 80 °C	329	A
I_{Fnom}			400	A
I_{FRM}	I_{FRM} = 3xI_{Fnom}		1200	A
I_{FSM}	t_p = 10 ms, sin 180°, T_j = 25 °C		1980	A
T_j			-40 ... 175	°C
Module				
$I_{t(RMS)}$			500	A
T_{stg}			-40 ... 125	°C
V_{isol}	AC sinus 50Hz, t = 1 min		4000	V

Characteristics						
Symbol	**Conditions**		**min.**	**typ.**	**max.**	**Unit**
IGBT						
$V_{CE(sat)}$	I_C = 400 A V_{GE} = 15 V chiplevel	T_j = 25 °C		1.8	2.05	V
		T_j = 150 °C		2.2	2.4	V
V_{CE0}		T_j = 25 °C		0.8	0.9	V
		T_j = 150 °C		0.7	0.8	V
r_{CE}	V_{GE} = 15 V	T_j = 25 °C		2.5	2.9	mΩ
		T_j = 150 °C		3.8	4.0	mΩ
$V_{GE(th)}$	V_{GE}=V_{CE}, I_C = 15.2 mA		5	5.8	6.5	V
I_{CES}	V_{GE} = 0 V	T_j = 25 °C		0.1	0.3	mA
	V_{CE} = 1200 V	T_j = 150 °C				mA
C_{ies}	V_{CE} = 25 V V_{GE} = 0 V	f = 1 MHz		24.6		nF
C_{oes}		f = 1 MHz		1.62		nF
C_{res}		f = 1 MHz		1.38		nF
Q_G	V_{GE} = - 8 V...+ 15 V			2260		nC
R_{Gint}	T_j = 25 °C			1.9		Ω
$t_{d(on)}$	V_{CC} = 600 V	T_j = 150 °C		220		ns
t_r	I_C = 400 A	T_j = 150 °C		47		ns
E_{on}	V_{GE} = ±15 V $R_{G\ on}$ = 1 Ω	T_j = 150 °C		33		mJ
$t_{d(off)}$	$R_{G\ off}$ = 1 Ω	T_j = 150 °C		505		ns
t_f	di/dt_{on} = 9700 A/µs	T_j = 150 °C		78		ns
E_{off}	di/dt_{off} = 4300 A/µs	T_j = 150 °C		42		mJ
$R_{th(j-c)}$	per IGBT				0.072	K/W

SKM400GB12T4

SEMITRANS®3

Fast IGBT4 Modules

SKM400GB12T4

Features

- $V_{CE(sat)}$ with positive temperature coefficient
- High short circuit capability, self limiting to 6 x Icnom
- Fast & soft inverse CAL diodes
- Large clearance (10 mm) and creepage distances (20 mm)
- Isolated copper baseplate using DBC Technology (Direct Copper Bonding)

Typical Applications

- AC inverter drives
- UPS
- Electronic welders at fsw up to 20 kHz

Remarks

- Case temperature limited to T_c = 125°C max, recomm. T_{op} = -40 ... +150°C, product rel. results valid for T_j = 150°

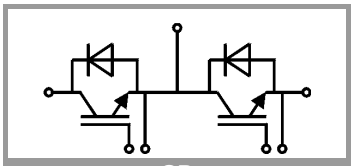

GB

Characteristics						
Symbol	**Conditions**		**min.**	**typ.**	**max.**	**Unit**
Inverse diode						
$V_F = V_{EC}$	I_F = 400 A V_{GE} = 0 V chip	T_j = 25 °C		2.2	2.52	V
		T_j = 150 °C		2.15	2.47	V
V_{F0}		T_j = 25 °C		1.3	1.5	V
		T_j = 150 °C		0.9	1.1	V
r_F		T_j = 25 °C		2.3	2.5	mΩ
		T_j = 150 °C		3.1	3.4	mΩ
I_{RRM}	I_F = 400 A di/dt$_{off}$ = 8800 A/µs V_{GE} = ±15 V V_{CC} = 600 V	T_j = 150 °C		450		A
Q_{rr}		T_j = 150 °C		68		µC
E_{rr}		T_j = 150 °C		30.5		mJ
$R_{th(j-c)}$	per diode				0.14	K/W
Module						
L_{CE}				15	20	nH
$R_{CC'+EE'}$	terminal-chip	T_C = 25 °C		0.25		mΩ
		T_C = 125 °C		0.5		mΩ
$R_{th(c-s)}$	per module			0.02	0.038	K/W
M_s	to heat sink M6		3		5	Nm
M_t		to terminals M6	2.5		5	Nm
						Nm
w					325	g

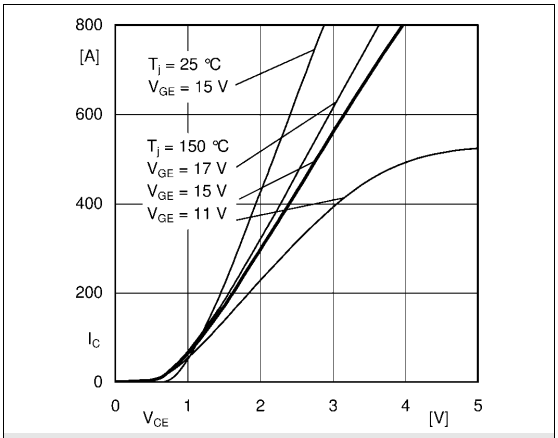

Fig. 1: Typ. output characteristic, inclusive $R_{CC'+EE'}$

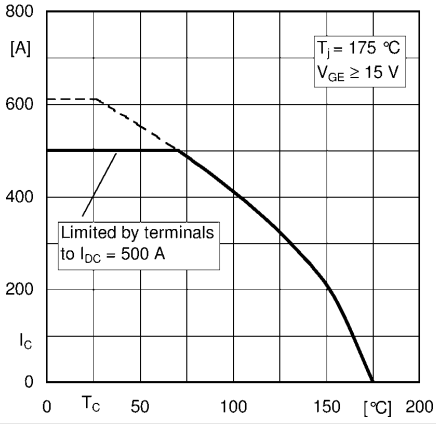

Fig. 2: Rated current vs. temperature $I_C = f(T_C)$

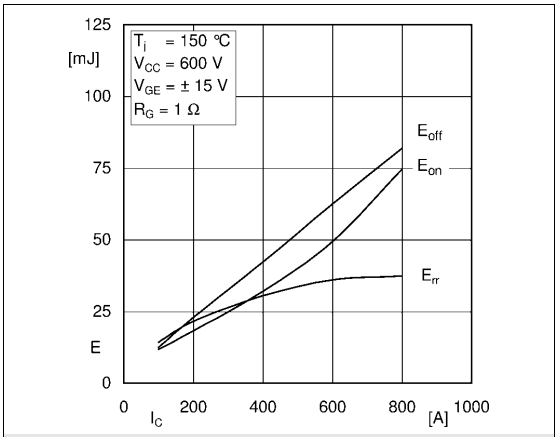

Fig. 3: Typ. turn-on /-off energy = f (I_C)

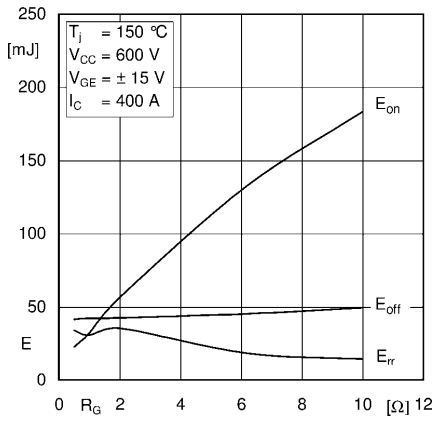

Fig. 4: Typ. turn-on /-off energy = f (R_G)

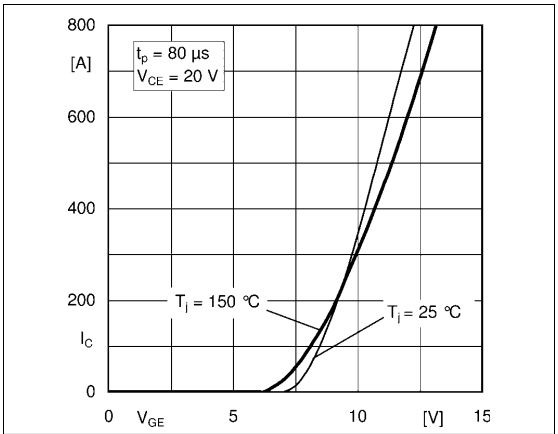

Fig. 5: Typ. transfer characteristic

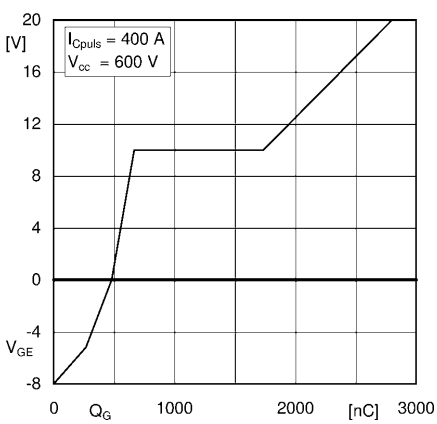

Fig. 6: Typ. gate charge characteristic

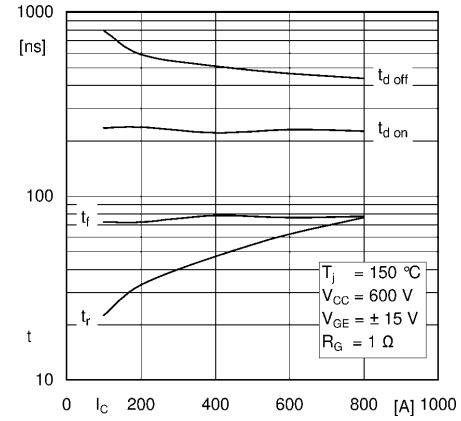

Fig. 7: Typ. switching times vs. I_C

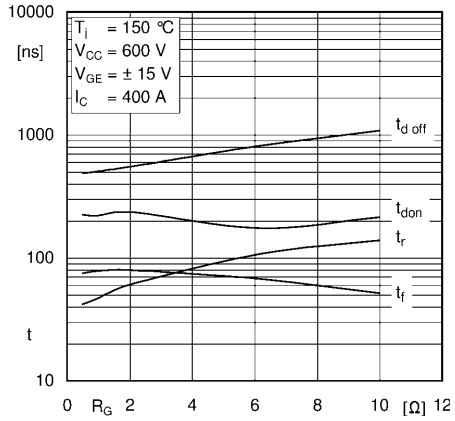

Fig. 8: Typ. switching times vs. gate resistor R_G

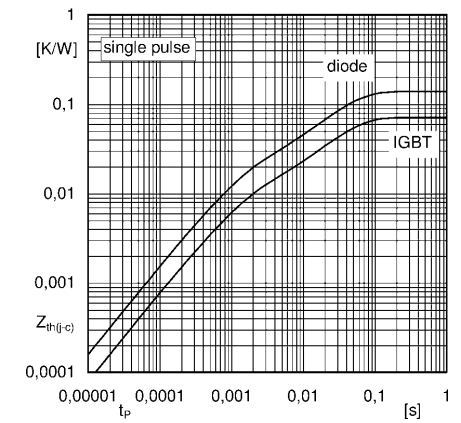

Fig. 9: Transient thermal impedance

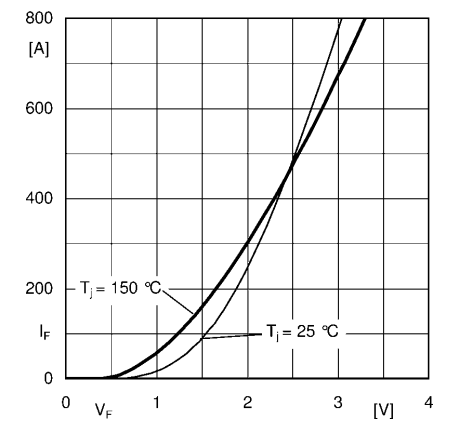

Fig. 10: CAL diode forward characteristic

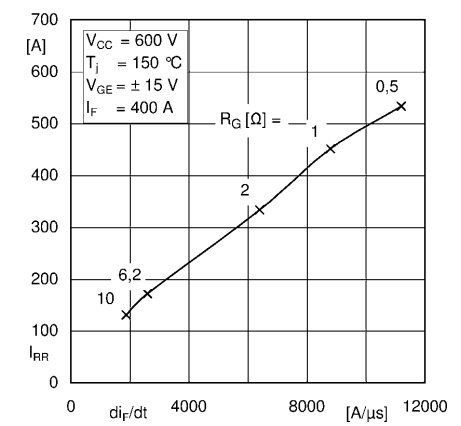

Fig. 11: CAL diode peak reverse recovery current

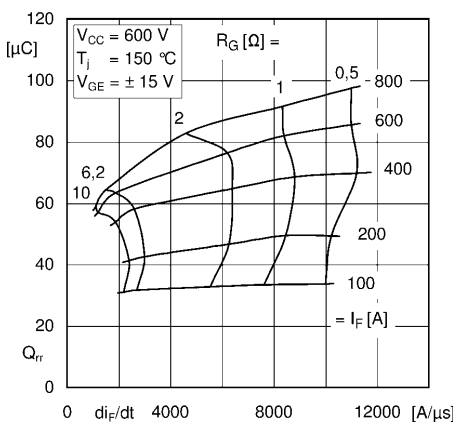

Fig. 12: Typ. CAL diode peak reverse recovery charge

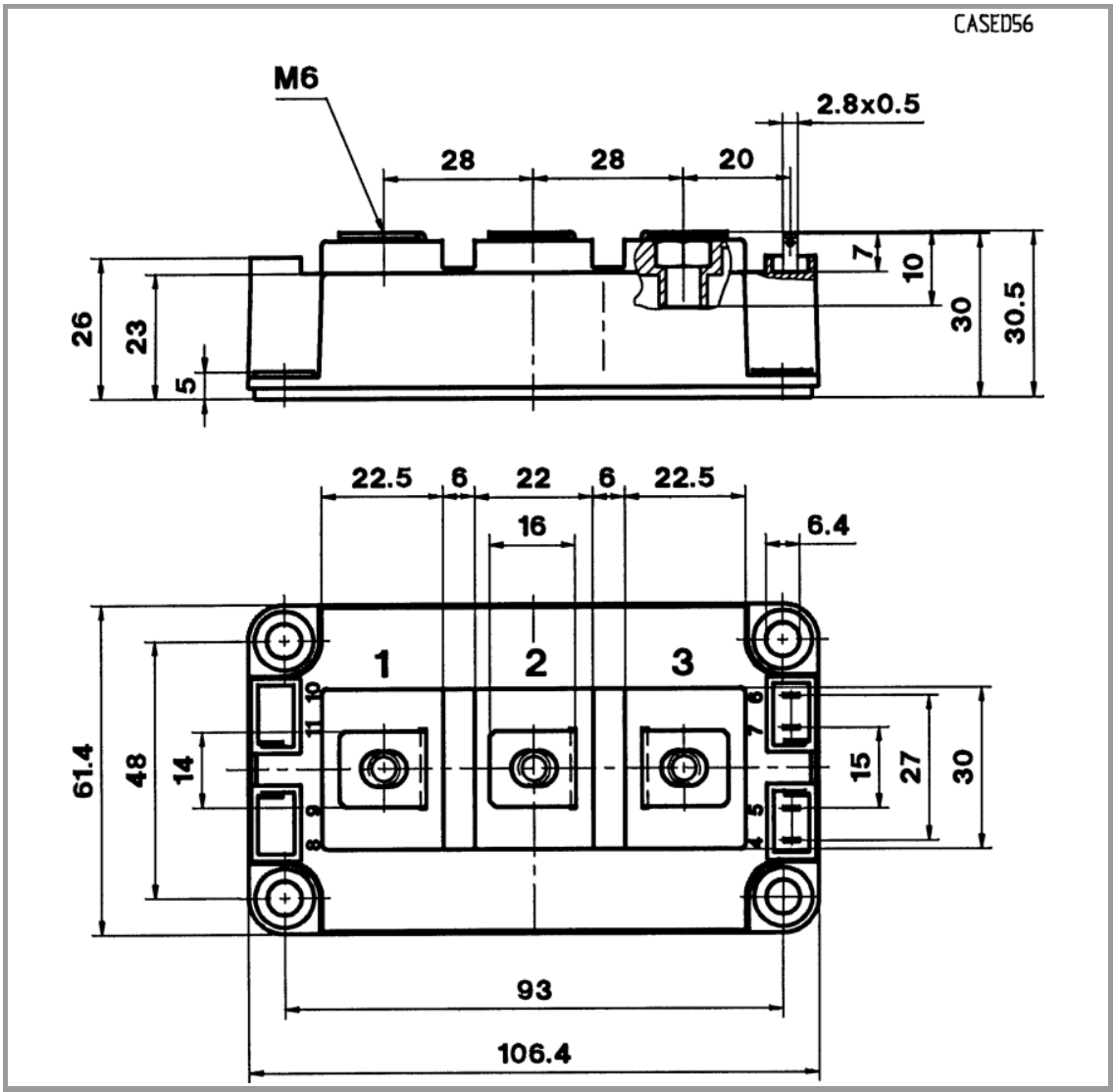

Semitrans 3

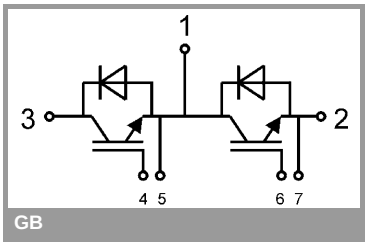

GB

This is an electrostatic discharge sensitive device (ESDS), international standard IEC 60747-1, Chapter IX.

This technical information specifies semiconductor devices but promises no characteristics. No warranty or guarantee expressed or implied is made regarding delivery, performance or suitability.

Technische Information / Technical Information

IGBT-Module
IGBT-modules

FZ600R12KE4

62mm C-Serien Modul mit Trench/Feldstopp IGBT4 und Emitter Controlled 4 Diode
62mm C-Series module with Trench/Fieldstop IGBT4 and Emitter Controlled 4 diode

Vorläufige Daten / Preliminary Data

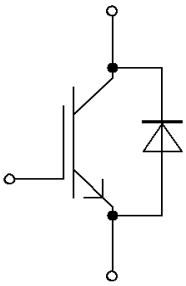

V_{CES} = 1200V
$I_{C\ nom}$ = 600A / I_{CRM} = 1200A

Typische Anwendungen
- Hochleistungsumrichter
- Motorantriebe
- USV-Systeme
- Windgeneratoren

Typical Applications
- High Power Converters
- Motor Drives
- UPS Systems
- Wind Turbines

Elektrische Eigenschaften
- Erweiterte Sperrschichttemperatur $T_{vj\ op}$
- Niedrige Schaltverluste
- Sehr große Robustheit
- V_{CEsat} mit positivem Temperaturkoeffizienten
- Niedriges V_{CEsat}

Electrical Features
- Extended Operation Temperature $T_{vj\ op}$
- Low Switching Losses
- Unbeatable Robustness
- V_{CEsat} with positive Temperature Coefficient
- Low V_{CEsat}

Mechanische Eigenschaften
- 4 kV AC 1min Isolationsfestigkeit
- Gehäuse mit CTI > 400
- Große Luft- und Kriechstrecken
- Isolierte Bodenplatte
- Standardgehäuse

Mechanical Features
- 4 kV AC 1min Insulation
- Package with CTI > 400
- High Creepage and Clearance Distances
- Isolated Base Plate
- Standard Housing

Module Label Code

Barcode Code 128

DMX - Code

Content of the Code	Digit
Module Serial Number	1 - 5
Module Material Number	6 - 11
Production Order Number	12 - 19
Datecode (Production Year)	20 - 21
Datecode (Production Week)	22 - 23

prepared by: MK	date of publication: 2013-11-04	
approved by: WR	revision: 2.1	UL approved (E83335)

Vorläufige Daten
Preliminary Data

IGBT,Wechselrichter / IGBT,Inverter

Höchstzulässige Werte / Maximum Rated Values

Kollektor-Emitter-Sperrspannung Collector-emitter voltage	T_{vj} = 25°C	V_{CES}	1200		V
Kollektor-Dauergleichstrom Continuous DC collector current	T_C = 100°C, $T_{vj\,max}$ = 175°C	$I_{C\,nom}$	600		A
Periodischer Kollektor-Spitzenstrom Repetitive peak collector current	t_P = 1 ms	I_{CRM}	1200		A
Gesamt-Verlustleistung Total power dissipation	T_C = 25°C, $T_{vj\,max}$ = 175°C	P_{tot}	3000		W
Gate-Emitter-Spitzenspannung Gate-emitter peak voltage		V_{GES}	+/-20		V

Charakteristische Werte / Characteristic Values

			min.	typ.	max.	
Kollektor-Emitter-Sättigungsspannung Collector-emitter saturation voltage	I_C = 600 A, V_{GE} = 15 V T_{vj} = 25°C I_C = 600 A, V_{GE} = 15 V T_{vj} = 125°C I_C = 600 A, V_{GE} = 15 V T_{vj} = 150°C	$V_{CE\,sat}$		1,75 2,00 2,05	2,10	V V V
Gate-Schwellenspannung Gate threshold voltage	I_C = 23,0 mA, V_{CE} = V_{GE}, T_{vj} = 25°C	V_{GEth}	5,2	5,8	6,4	V
Gateladung Gate charge	V_{GE} = -15 V ... +15 V	Q_G		5,60		µC
Interner Gatewiderstand Internal gate resistor	T_{vj} = 25°C	R_{Gint}		1,3		Ω
Eingangskapazität Input capacitance	f = 1 MHz, T_{vj} = 25°C, V_{CE} = 25 V, V_{GE} = 0 V	C_{ies}		42,0		nF
Rückwirkungskapazität Reverse transfer capacitance	f = 1 MHz, T_{vj} = 25°C, V_{CE} = 25 V, V_{GE} = 0 V	C_{res}		1,70		nF
Kollektor-Emitter-Reststrom Collector-emitter cut-off current	V_{CE} = 1200 V, V_{GE} = 0 V, T_{vj} = 25°C	I_{CES}			5,0	mA
Gate-Emitter-Reststrom Gate-emitter leakage current	V_{CE} = 0 V, V_{GE} = 20 V, T_{vj} = 25°C	I_{GES}			400	nA
Einschaltverzögerungszeit, induktive Last Turn-on delay time, inductive load	I_C = 600 A, V_{CE} = 600 V T_{vj} = 25°C V_{GE} = ±15 V T_{vj} = 125°C R_{Gon} = 1,2 Ω T_{vj} = 150°C	$t_{d\,on}$		0,24 0,25 0,26		µs µs µs
Anstiegszeit, induktive Last Rise time, inductive load	I_C = 600 A, V_{CE} = 600 V T_{vj} = 25°C V_{GE} = ±15 V T_{vj} = 125°C R_{Gon} = 1,2 Ω T_{vj} = 150°C	t_r		0,09 0,10 0,11		µs µs µs
Abschaltverzögerungszeit, induktive Last Turn-off delay time, inductive load	I_C = 600 A, V_{CE} = 600 V T_{vj} = 25°C V_{GE} = ±15 V T_{vj} = 125°C R_{Goff} = 1,2 Ω T_{vj} = 150°C	$t_{d\,off}$		0,61 0,64 0,66		µs µs µs
Fallzeit, induktive Last Fall time, inductive load	I_C = 600 A, V_{CE} = 600 V T_{vj} = 25°C V_{GE} = ±15 V T_{vj} = 125°C R_{Goff} = 1,2 Ω T_{vj} = 150°C	t_f		0,10 0,14 0,15		µs µs µs
Einschaltverlustenergie pro Puls Turn-on energy loss per pulse	I_C = 600 A, V_{CE} = 600 V, L_S = 60 nH T_{vj} = 25°C V_{GE} = ±15 V, di/dt = 5500 A/µs (T_{vj} = 150°C) T_{vj} = 125°C R_{Gon} = 1,2 Ω T_{vj} = 150°C	E_{on}		35,0 50,0 55,0		mJ mJ mJ
Abschaltverlustenergie pro Puls Turn-off energy loss per pulse	I_C = 600 A, V_{CE} = 600 V, L_S = 60 nH T_{vj} = 25°C V_{GE} = ±15 V, du/dt = 3500 V/µs (T_{vj} = 150°C) T_{vj} = 125°C R_{Goff} = 1,2 Ω T_{vj} = 150°C	E_{off}		50,0 75,0 80,0		mJ mJ mJ
Kurzschlußverhalten SC data	V_{GE} ≤ 15 V, V_{CC} = 800 V V_{CEmax} = V_{CES} -L_{sCE} ·di/dt t_P ≤ 10 µs, T_{vj} = 150°C	I_{SC}		2400		A
Wärmewiderstand, Chip bis Gehäuse Thermal resistance, junction to case	pro IGBT / per IGBT	R_{thJC}			0,05	K/W
Wärmewiderstand, Gehäuse bis Kühlkörper Thermal resistance, case to heatsink	pro IGBT / per IGBT λ_{Paste} = 1 W/(m·K) / λ_{grease} = 1 W/(m·K)	R_{thCH}		0,017		K/W
Temperatur im Schaltbetrieb Temperature under switching conditions		$T_{vj\,op}$	-40		150	°C

prepared by: MK	date of publication: 2013-11-04
approved by: WR	revision: 2.1

Vorläufige Daten
Preliminary Data

Diode, Wechselrichter / Diode, Inverter

Höchstzulässige Werte / Maximum Rated Values

Periodische Spitzensperrspannung Repetitive peak reverse voltage	T_{vj} = 25°C	V_{RRM}	1200		V
Dauergleichstrom Continuous DC forward current		I_F	600		A
Periodischer Spitzenstrom Repetitive peak forward current	t_P = 1 ms	I_{FRM}	1200		A
Grenzlastintegral I²t - value	V_R = 0 V, t_P = 10 ms, T_{vj} = 125°C V_R = 0 V, t_P = 10 ms, T_{vj} = 150°C	I²t	51000 49000		A²s A²s

Charakteristische Werte / Characteristic Values

			min.	typ.	max.	
Durchlassspannung Forward voltage	I_F = 600 A, V_{GE} = 0 V I_F = 600 A, V_{GE} = 0 V I_F = 600 A, V_{GE} = 0 V	T_{vj} = 25°C T_{vj} = 125°C T_{vj} = 150°C	V_F	1,80 1,75 1,70	2,35	V V V
Rückstromspitze Peak reverse recovery current	I_F = 600 A, - di_F/dt = 5500 A/µs (T_{vj}=150°C) V_R = 600 V V_{GE} = -15 V	T_{vj} = 25°C T_{vj} = 125°C T_{vj} = 150°C	I_{RM}	440 560 590		A A A
Sperrverzögerungsladung Recovered charge	I_F = 600 A, - di_F/dt = 5500 A/µs (T_{vj}=150°C) V_R = 600 V V_{GE} = -15 V	T_{vj} = 25°C T_{vj} = 125°C T_{vj} = 150°C	Q_r	55,0 100 115		µC µC µC
Abschaltenergie pro Puls Reverse recovery energy	I_F = 600 A, - di_F/dt = 5500 A/µs (T_{vj}=150°C) V_R = 600 V V_{GE} = -15 V	T_{vj} = 25°C T_{vj} = 125°C T_{vj} = 150°C	E_{rec}	27,0 52,0 60,0		mJ mJ mJ
Wärmewiderstand, Chip bis Gehäuse Thermal resistance, junction to case	pro Diode / per diode		R_{thJC}		0,07	K/W
Wärmewiderstand, Gehäuse bis Kühlkörper Thermal resistance, case to heatsink	pro Diode / per diode λ_{Paste} = 1 W/(m·K) / λ_{grease} = 1 W/(m·K)		R_{thCH}	0,024		K/W
Temperatur im Schaltbetrieb Temperature under switching conditions			$T_{vj\,op}$	-40	150	°C

prepared by: MK	date of publication: 2013-11-04
approved by: WR	revision: 2.1

Vorläufige Daten
Preliminary Data

Modul / Module

Isolations-Prüfspannung Isolation test voltage	RMS, f = 50 Hz, t = 1 min.	V_{ISOL}		4,0		kV
Material Modulgrundplatte Material of module baseplate				Cu		
Innere Isolation Internal isolation	Basisisolierung (Schutzklasse 1, EN61140) basic insulation (class 1, IEC 61140)			Al_2O_3		
Kriechstrecke Creepage distance	Kontakt - Kühlkörper / terminal to heatsink Kontakt - Kontakt / terminal to terminal			25,0 19,0		mm
Luftstrecke Clearance	Kontakt - Kühlkörper / terminal to heatsink Kontakt - Kontakt / terminal to terminal			25,0 10,0		mm
Vergleichszahl der Kriechwegbildung Comperative tracking index		CTI		> 400		
			min.	typ.	max.	
Wärmewiderstand, Gehäuse bis Kühlkörper Thermal resistance, case to heatsink	pro Modul / per module λ_{Paste} = 1 W/(m·K) / λ_{grease} = 1 W/(m·K)	R_{thCH}		0,01		K/W
Modulstreuinduktivität Stray inductance module		L_{sCE}		16		nH
Modulleitungswiderstand, Anschlüsse - Chip Module lead resistance, terminals - chip	T_C = 25°C, pro Schalter / per switch	$R_{CC'+EE'}$		0,50		mΩ
Lagertemperatur Storage temperature		T_{stg}	-40		125	°C
Anzugsdrehmoment f. Modulmontage Mounting torque for modul mounting	Schraube M6 - Montage gem. gültiger Applikationsschrift Screw M6 - Mounting according to valid application note	M	3,00	-	6,00	Nm
Anzugsdrehmoment f. elektr. Anschlüsse Terminal connection torque	Schraube M4 - Montage gem. gültiger Applikationsschrift Screw M4 - Mounting according to valid application note Schraube M6 - Montage gem. gültiger Applikationsschrift Screw M6 - Mounting according to valid application note	M	1,1 2,5	- -	2,0 5,0	Nm Nm
Gewicht Weight		G		340		g

Vorläufige Daten
Preliminary Data

Ausgangskennlinie IGBT,Wechselrichter (typisch)
output characteristic IGBT,Inverter (typical)
$I_C = f(V_{CE})$
V_{GE} = 15 V

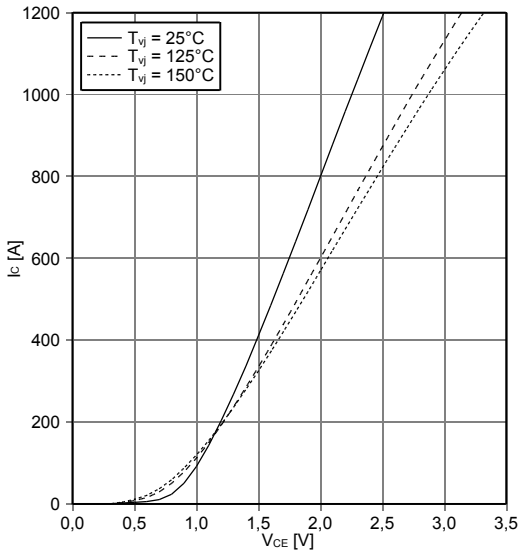

Ausgangskennlinienfeld IGBT,Wechselrichter (typisch)
output characteristic IGBT,Inverter (typical)
$I_C = f(V_{CE})$
T_{vj} = 150°C

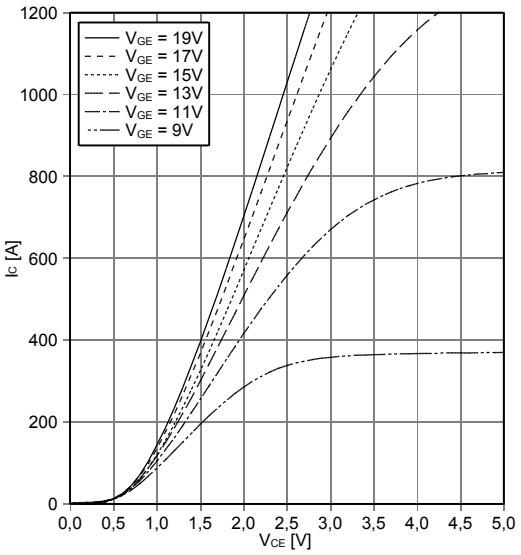

Übertragungscharakteristik IGBT,Wechselrichter (typisch)
transfer characteristic IGBT,Inverter (typical)
$I_C = f(V_{GE})$
V_{CE} = 20 V

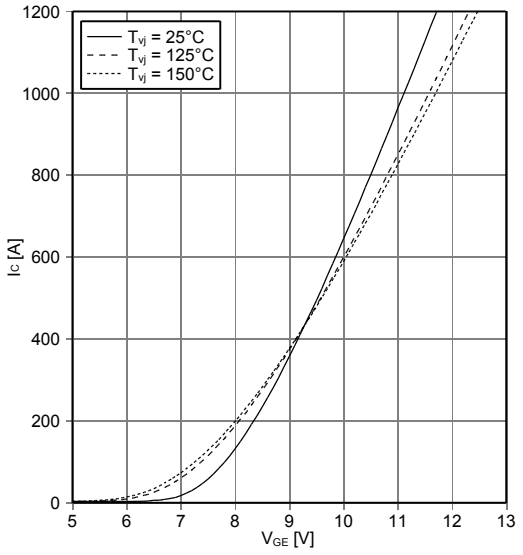

Schaltverluste IGBT,Wechselrichter (typisch)
switching losses IGBT,Inverter (typical)
$E_{on} = f(I_C)$, $E_{off} = f(I_C)$
V_{GE} = ±15 V, R_{Gon} = 1.2 Ω, R_{Goff} = 1.2 Ω, V_{CE} = 600 V

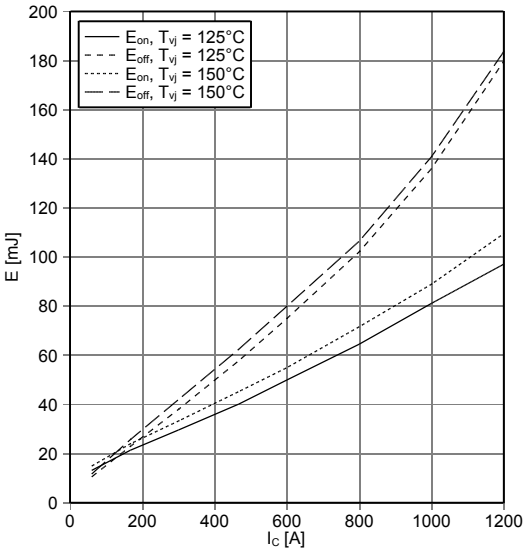

prepared by: MK	date of publication: 2013-11-04
approved by: WR	revision: 2.1

Vorläufige Daten
Preliminary Data

Schaltverluste IGBT,Wechselrichter (typisch)
switching losses IGBT,Inverter (typical)
$E_{on} = f(R_G)$, $E_{off} = f(R_G)$
V_{GE} = ±15 V, I_C = 600 A, V_{CE} = 600 V

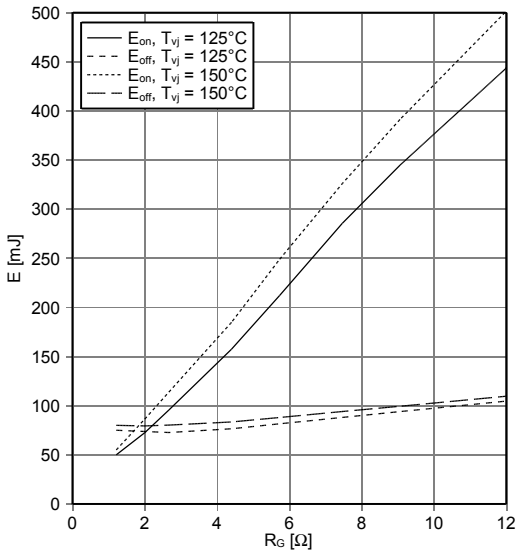

Transienter Wärmewiderstand IGBT,Wechselrichter
transient thermal impedance IGBT,Inverter
$Z_{thJC} = f(t)$

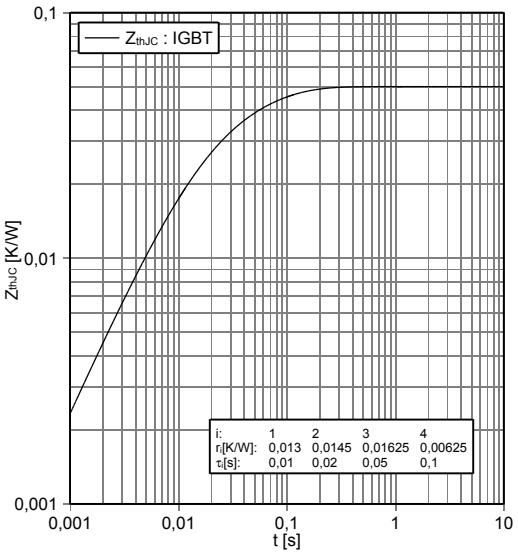

Sicherer Rückwärts-Arbeitsbereich IGBT,Wechselrichter (RBSOA)
reverse bias safe operating area IGBT,Inverter (RBSOA)
$I_C = f(V_{CE})$
V_{GE} = ±15 V, R_{Goff} = 1.2 Ω, T_{vj} = 150°C

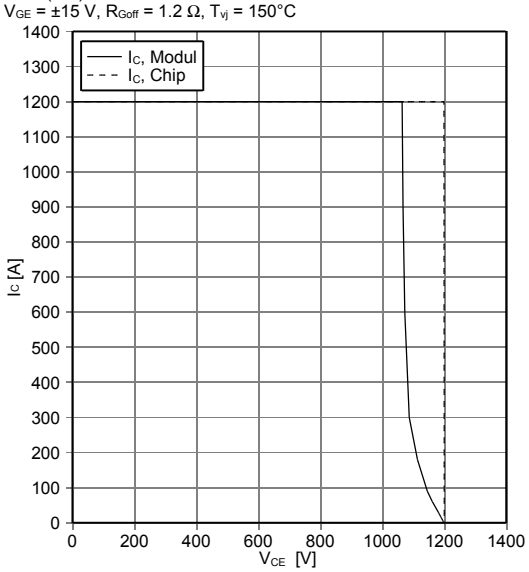

Durchlasskennlinie der Diode, Wechselrichter (typisch)
forward characteristic of Diode, Inverter (typical)
$I_F = f(V_F)$

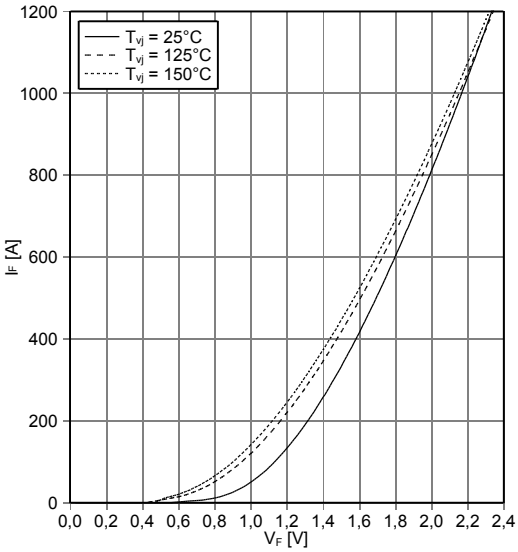

prepared by: MK	date of publication: 2013-11-04
approved by: WR	revision: 2.1

Vorläufige Daten
Preliminary Data

Schaltverluste Diode, Wechselrichter (typisch)
switching losses Diode, Inverter (typical)
$E_{rec} = f(I_F)$
$R_{Gon} = 1.2\ \Omega$, $V_{CE} = 600$ V

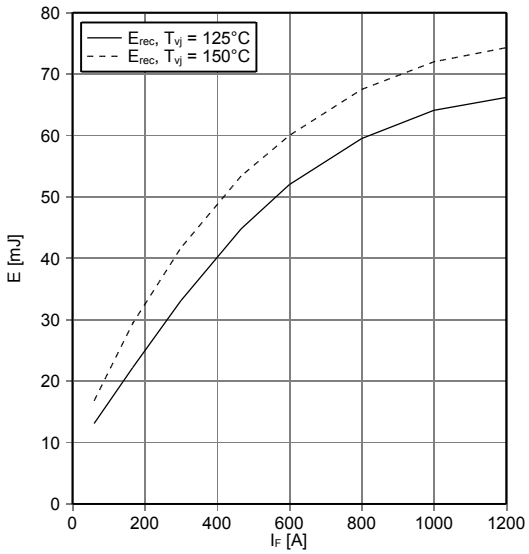

Schaltverluste Diode, Wechselrichter (typisch)
switching losses Diode, Inverter (typical)
$E_{rec} = f(R_G)$
$I_F = 600$ A, $V_{CE} = 600$ V

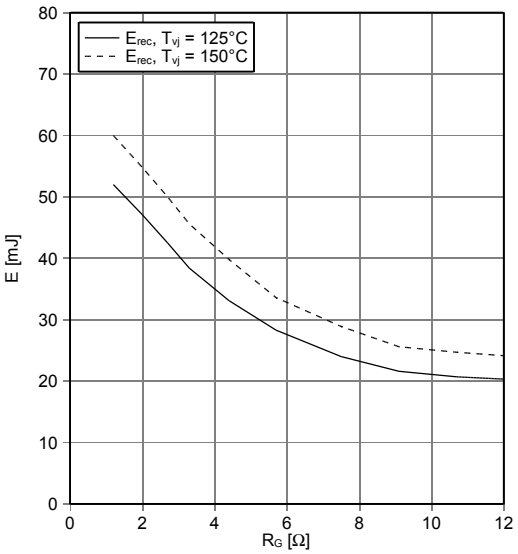

Transienter Wärmewiderstand Diode, Wechselrichter
transient thermal impedance Diode, Inverter
$Z_{thJC} = f(t)$

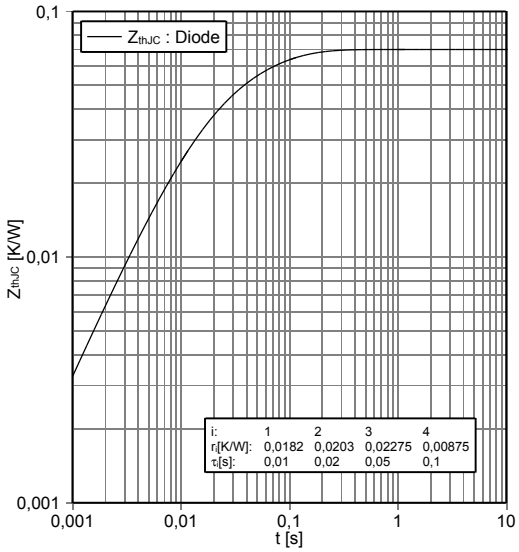

prepared by: MK	date of publication: 2013-11-04
approved by: WR	revision: 2.1

Vorläufige Daten
Preliminary Data

Schaltplan / circuit_diagram_headline

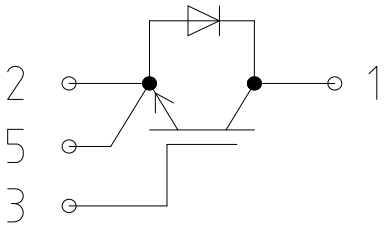

Gehäuseabmessungen / package outlines

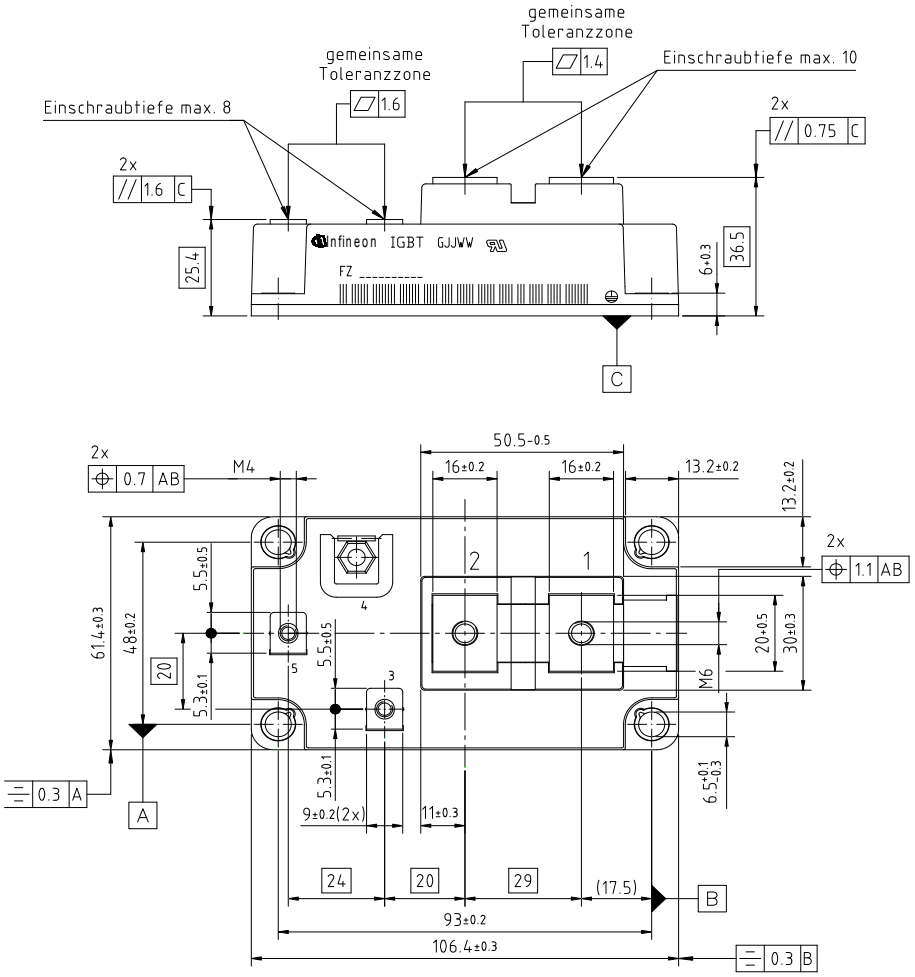

prepared by: MK	date of publication: 2013-11-04
approved by: WR	revision: 2.1

Vorläufige Daten
Preliminary Data

Nutzungsbedingungen

Die in diesem Produktdatenblatt enthaltenen Daten sind ausschließlich für technisch geschultes Fachpersonal bestimmt. Die Beurteilung der Eignung dieses Produktes für Ihre Anwendung sowie die Beurteilung der Vollständigkeit der bereitgestellten Produktdaten für diese Anwendung obliegt Ihnen bzw. Ihren technischen Abteilungen.

In diesem Produktdatenblatt werden diejenigen Merkmale beschrieben, für die wir eine liefervertragliche Gewährleistung übernehmen. Eine solche Gewährleistung richtet sich ausschließlich nach Maßgabe der im jeweiligen Liefervertrag enthaltenen Bestimmungen. Garantien jeglicher Art werden für das Produkt und dessen Eigenschaften keinesfalls übernommen. Die Angaben in den gültigen Anwendungs- und Montagehinweisen des Moduls sind zu beachten.

Sollten Sie von uns Produktinformationen benötigen, die über den Inhalt dieses Produktdatenblatts hinausgehen und insbesondere eine spezifische Verwendung und den Einsatz dieses Produktes betreffen, setzen Sie sich bitte mit dem für Sie zuständigen Vertriebsbüro in Verbindung (siehe www.infineon.com, Vertrieb&Kontakt). Für Interessenten halten wir Application Notes bereit.

Aufgrund der technischen Anforderungen könnte unser Produkt gesundheitsgefährdende Substanzen enthalten. Bei Rückfragen zu den in diesem Produkt jeweils enthaltenen Substanzen setzen Sie sich bitte ebenfalls mit dem für Sie zuständigen Vertriebsbüro in Verbindung.

Sollten Sie beabsichtigen, das Produkt in Anwendungen der Luftfahrt, in gesundheits- oder lebensgefährdenden oder lebenserhaltenden Anwendungsbereichen einzusetzen, bitten wir um Mitteilung. Wir weisen darauf hin, dass wir für diese Fälle
- die gemeinsame Durchführung eines Risiko- und Qualitätsassessments;
- den Abschluss von speziellen Qualitätssicherungsvereinbarungen;
- die gemeinsame Einführung von Maßnahmen zu einer laufenden Produktbeobachtung dringend empfehlen und gegebenenfalls die Belieferung von der Umsetzung solcher Maßnahmen abhängig machen.

Soweit erforderlich, bitten wir Sie, entsprechende Hinweise an Ihre Kunden zu geben.

Inhaltliche Änderungen dieses Produktdatenblatts bleiben vorbehalten.

Terms & Conditions of usage

The data contained in this product data sheet is exclusively intended for technically trained staff. You and your technical departments will have to evaluate the suitability of the product for the intended application and the completeness of the product data with respect to such application.

This product data sheet is describing the characteristics of this product for which a warranty is granted. Any such warranty is granted exclusively pursuant the terms and conditions of the supply agreement. There will be no guarantee of any kind for the product and its characteristics. The information in the valid application- and assembly notes of the module must be considered.

Should you require product information in excess of the data given in this product data sheet or which concerns the specific application of our product, please contact the sales office, which is responsible for you (see www.infineon.com). For those that are specifically interested we may provide application notes.

Due to technical requirements our product may contain dangerous substances. For information on the types in question please contact the sales office, which is responsible for you.

Should you intend to use the Product in aviation applications, in health or live endangering or life support applications, please notify. Please note, that for any such applications we urgently recommend
- to perform joint Risk and Quality Assessments;
- the conclusion of Quality Agreements;
- to establish joint measures of an ongoing product survey, and that we may make delivery depended on the realization of any such measures.

If and to the extent necessary, please forward equivalent notices to your customers.

Changes of this product data sheet are reserved.

prepared by: MK	date of publication: 2013-11-04
approved by: WR	revision: 2.1

V_{CE} = 1700 V
I_C = 800 A

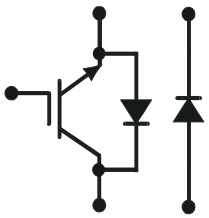

ABB HiPak™

IGBT Module

5SNE 0800M170100

Doc. No. 5SYA1590-00 Oct 06

- **Low-loss, rugged SPT chip-set**
- **Smooth switching SPT chip-set for good EMC**
- **Industry standard package**
- **High power density**
- **AlSiC base-plate for high power cycling capability**
- **AlN substrate for low thermal resistance**

Maximum rated values [1]

Parameter	Symbol	Conditions	min	max	Unit
Collector-emitter voltage	V_{CES}	V_{GE} = 0 V, $T_{vj} \geq$ 25 °C		1700	V
DC collector current	I_C	T_c = 80 °C		800	A
Peak collector current	I_{CM}	t_p = 1 ms, T_c = 80 °C		1600	A
Gate-emitter voltage	V_{GES}		-20	20	V
Total power dissipation	P_{tot}	T_c = 25 °C, per switch (IGBT)		4800	W
DC forward current	I_F			800	A
Peak forward current	I_{FRM}			1600	A
Surge current	I_{FSM}	V_R = 0 V, T_{vj} = 125 °C, t_p = 10 ms, half-sinewave		6600	A
IGBT short circuit SOA	t_{psc}	V_{CC} = 1200 V, $V_{CEM\,CHIP} \leq$ 1700 V $V_{GE} \leq$ 15 V, $T_{vj} \leq$ 125 °C		10	µs
Isolation voltage	V_{isol}	1 min, f = 50 Hz		4000	V
Junction temperature	T_{vj}			150	°C
Junction operating temperature	$T_{vj(op)}$		-40	125	°C
Case temperature	T_c		-40	125	°C
Storage temperature	T_{stg}		-40	125	°C
Mounting torques [2]	M_s	Base-heatsink, M6 screws	4	6	Nm
	M_{t1}	Main terminals, M8 screws	8	10	
	M_{t2}	Auxiliary terminals, M4 screws	2	3	

[1] Maximum rated values indicate limits beyond which damage to the device may occur per IEC 60747
[2] For detailed mounting instructions refer to ABB document no. 5SYA 2039 - 01

IGBT characteristic values [3]

Parameter	Symbol	Conditions		min	typ	max	Unit
Collector (-emitter) breakdown voltage	$V_{(BR)CES}$	V_{GE} = 0 V, I_C = 10 mA, T_{vj} = 25 °C		1700			V
Collector-emitter [4] saturation voltage	$V_{CE\ sat}$	I_C = 800 A, V_{GE} = 15 V	T_{vj} = 25 °C	2.0	2.3	2.6	V
			T_{vj} = 125 °C	2.3	2.6	2.9	V
Collector cut-off current	I_{CES}	V_{CE} = 1700 V, V_{GE} = 0 V	T_{vj} = 25 °C			4	mA
			T_{vj} = 125 °C			40	mA
Gate leakage current	I_{GES}	V_{CE} = 0 V, V_{GE} = ±20 V, T_{vj} = 125 °C		-500		500	nA
Gate-emitter threshold voltage	$V_{GE(TO)}$	I_C = 80 mA, V_{CE} = V_{GE}, T_{vj} = 25 °C		4.5		6.5	V
Gate charge	Q_{ge}	I_C = 800 A, V_{CE} = 900 V, V_{GE} = -15 V .. 15 V			7.3		µC
Input capacitance	C_{ies}	V_{CE} = 25 V, V_{GE} = 0 V, f = 1 MHz, T_{vj} = 25 °C			76		nF
Output capacitance	C_{oes}				7.3		
Reverse transfer capacitance	C_{res}				3.2		
Turn-on delay time	$t_{d(on)}$	V_{CC} = 900 V, I_C = 800 A, R_G = 1.2 Ω, V_{GE} = ±15 V, L_σ = 80 nH, inductive load	T_{vj} = 25 °C		485		ns
			T_{vj} = 125 °C		485		
Rise time	t_r		T_{vj} = 25 °C		165		ns
			T_{vj} = 125 °C		170		
Turn-off delay time	$t_{d(off)}$	V_{CC} = 900 V, I_C = 800 A, R_G = 1.8 Ω, V_{GE} = ±15 V, L_σ = 80 nH, inductive load	T_{vj} = 25 °C		790		ns
			T_{vj} = 125 °C		875		
Fall time	t_f		T_{vj} = 25 °C		160		ns
			T_{vj} = 125 °C		185		
Turn-on switching energy	E_{on}	V_{CC} = 900 V, I_C = 800 A, V_{GE} = ±15 V, R_G = 1.2 Ω, L_σ = 80 nH, inductive load	T_{vj} = 25 °C		160		mJ
			T_{vj} = 125 °C		250		
Turn-off switching energy	E_{off}	V_{CC} = 900 V, I_C = 800 A, V_{GE} = ±15 V, R_G = 1.8 Ω, L_σ = 80 nH, inductive load	T_{vj} = 25 °C		220		mJ
			T_{vj} = 125 °C		300		
Short circuit current	I_{SC}	t_{psc} ≤ 10 µs, V_{GE} = 15 V, T_{vj} = 125 °C, V_{CC} = 1200 V, $V_{CEM\ CHIP}$ ≤ 1700 V			3600		A
Module stray inductance	$L_{\sigma\ CE}$	Leg 1			24		nH
Resistance, terminal-chip	$R_{CC'+EE'}$	Leg 1	T_C = 25 °C		0.18		mΩ
			T_C = 125 °C		0.255		

[3] Characteristic values according to IEC 60747 – 9
[4] Collector-emitter saturation voltage is given at chip level

IGBT characteristic values [3]

Parameter	Symbol	Conditions		min	typ	max	Unit
Collector (-emitter) breakdown voltage	$V_{(BR)CES}$	V_{GE} = 0 V, I_C = 10 mA, T_{vj} = 25 °C		1700			V
Collector-emitter [4] saturation voltage	$V_{CE\ sat}$	I_C = 800 A, V_{GE} = 15 V	T_{vj} = 25 °C	2.0	2.3	2.6	V
			T_{vj} = 125 °C	2.3	2.6	2.9	V
Collector cut-off current	I_{CES}	V_{CE} = 1700 V, V_{GE} = 0 V	T_{vj} = 25 °C			4	mA
			T_{vj} = 125 °C			40	mA
Gate leakage current	I_{GES}	V_{CE} = 0 V, V_{GE} = ±20 V, T_{vj} = 125 °C		-500		500	nA
Gate-emitter threshold voltage	$V_{GE(TO)}$	I_C = 80 mA, V_{CE} = V_{GE}, T_{vj} = 25 °C		4.5		6.5	V
Gate charge	Q_{ge}	I_C = 800 A, V_{CE} = 900 V, V_{GE} = -15 V .. 15 V			7.3		µC
Input capacitance	C_{ies}	V_{CE} = 25 V, V_{GE} = 0 V, f = 1 MHz, T_{vj} = 25 °C			76		nF
Output capacitance	C_{oes}				7.3		
Reverse transfer capacitance	C_{res}				3.2		
Turn-on delay time	$t_{d(on)}$	V_{CC} = 900 V, I_C = 800 A, R_G = 1.2 Ω, V_{GE} = ±15 V, L_σ = 80 nH, inductive load	T_{vj} = 25 °C		485		ns
			T_{vj} = 125 °C		485		
Rise time	t_r		T_{vj} = 25 °C		165		ns
			T_{vj} = 125 °C		170		
Turn-off delay time	$t_{d(off)}$	V_{CC} = 900 V, I_C = 800 A, R_G = 1.8 Ω, V_{GE} = ±15 V, L_σ = 80 nH, inductive load	T_{vj} = 25 °C		790		ns
			T_{vj} = 125 °C		875		
Fall time	t_f		T_{vj} = 25 °C		160		ns
			T_{vj} = 125 °C		185		
Turn-on switching energy	E_{on}	V_{CC} = 900 V, I_C = 800 A, V_{GE} = ±15 V, R_G = 1.2 Ω, L_σ = 80 nH, inductive load	T_{vj} = 25 °C		160		mJ
			T_{vj} = 125 °C		250		
Turn-off switching energy	E_{off}	V_{CC} = 900 V, I_C = 800 A, V_{GE} = ±15 V, R_G = 1.8 Ω, L_σ = 80 nH, inductive load	T_{vj} = 25 °C		220		mJ
			T_{vj} = 125 °C		300		
Short circuit current	I_{SC}	t_{psc} ≤ 10 µs, V_{GE} = 15 V, T_{vj} = 125 °C, V_{CC} = 1200 V, $V_{CEM\ CHIP}$ ≤ 1700 V			3600		A
Module stray inductance	$L_{\sigma\ CE}$	Leg 1			24		nH
Resistance, terminal-chip	$R_{CC'+EE'}$	Leg 1	T_C = 25 °C		0.18		mΩ
			T_C = 125 °C		0.255		

[3] Characteristic values according to IEC 60747 – 9
[4] Collector-emitter saturation voltage is given at chip level

Diode characteristic values [5]

Parameter	Symbol	Conditions		min	typ	max	Unit
Forward voltage [6]	V_F	I_F = 800 A	T_{vj} = 25 °C		1.65	2.0	V
			T_{vj} = 125 °C		1.7	2.0	
Reverse recovery current	I_{rr}	V_{CC} = 900 V, I_F = 800 A, V_{GE} = ±15 V, R_G = 1.2 Ω L_σ = 80 nH inductive load	T_{vj} = 25 °C		560		A
			T_{vj} = 125 °C		730		
Recovered charge	Q_{rr}		T_{vj} = 25 °C		210		µC
			T_{vj} = 125 °C		385		
Reverse recovery time	t_{rr}		T_{vj} = 25 °C		690		ns
			T_{vj} = 125 °C		975		
Reverse recovery energy	E_{rec}		T_{vj} = 25 °C		150		mJ
			T_{vj} = 125 °C		270		
Module stray inductance	$L_{\sigma AE}$	Leg 2			24		nH
Resistance, terminal-chip	$R_{AA'+CC'}$	Leg 2	T_C = 25 °C		0.18		mΩ
			T_C = 125 °C		0.255		

[5] Characteristic values according to IEC 60747 – 2
[6] Forward voltage is given at chip level

Thermal properties [7]

Parameter	Symbol	Conditions	min	typ	max	Unit
IGBT thermal resistance junction to case	$R_{th(j-c)IGBT}$	per switch			0.021	K/W
Diode thermal resistance junction to case	$R_{th(j-c)DIODE}$				0.036	K/W
IGBT thermal resistance case to heatsink [2]	$R_{th(c-s)IGBT}$	IGBT per switch, λ grease = 1W/m x K		0.024		K/W
Diode thermal resistance case to heatsink [7]	$R_{th(c-s)DIODE}$	Diode per switch, λ grease = 1W/m x K		0.048		K/W

[2] For detailed mounting instructions refer to ABB document no. 5SYA 2039 - 01

Mechanical properties [7]

Parameter	Symbol	Conditions		min	typ	max	Unit
Dimensions	L x W x H	Typical , see outline drawing			130 x 140 x 38		mm
Clearance distance in air	d_a	according to IEC 60664-1 and EN 50124-1	Term. to base:	10			mm
			Term. to term:	10			
Surface creepage distance	d_s	according to IEC 60664-1 and EN 50124-1	Term. to base:	15			mm
			Term. to term:	15			
Mass	m				900		g

[7] Thermal and mechanical properties according to IEC 60747 – 15

Electrical configuration

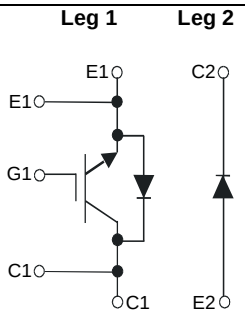

Outline drawing [2)]

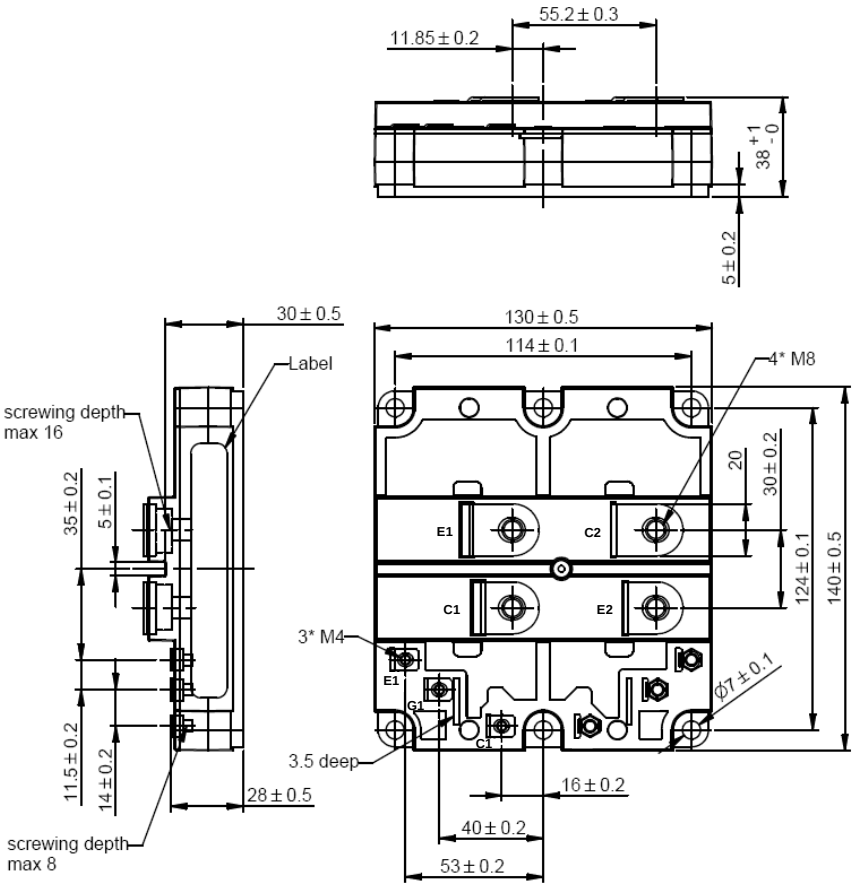

Note: all dimensions are shown in mm

[2)] For detailed mounting instructions refer to ABB document no. 5SYA 2039 - 01

This is an electrostatic sensitive device, please observe the international standard IEC 60747-1, chap. IX.
This product has been designed and qualified for industrial level.

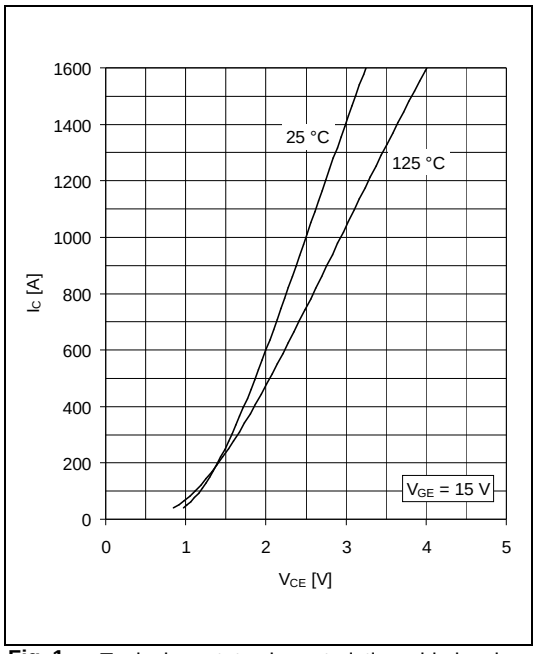

Fig. 1 Typical on-state characteristics, chip level

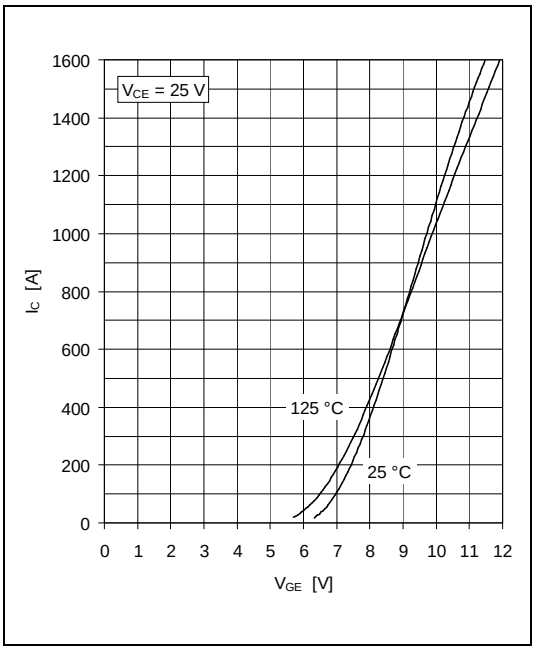

Fig. 2 Typical transfer characteristics, chip level

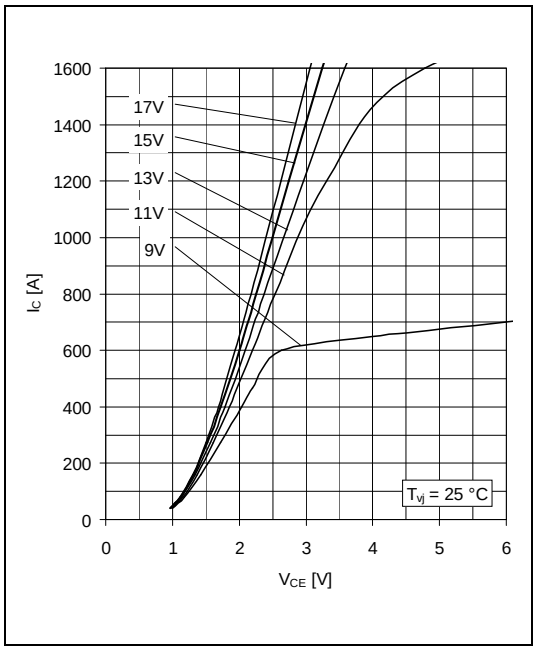

Fig. 3 Typical output characteristics, chip level

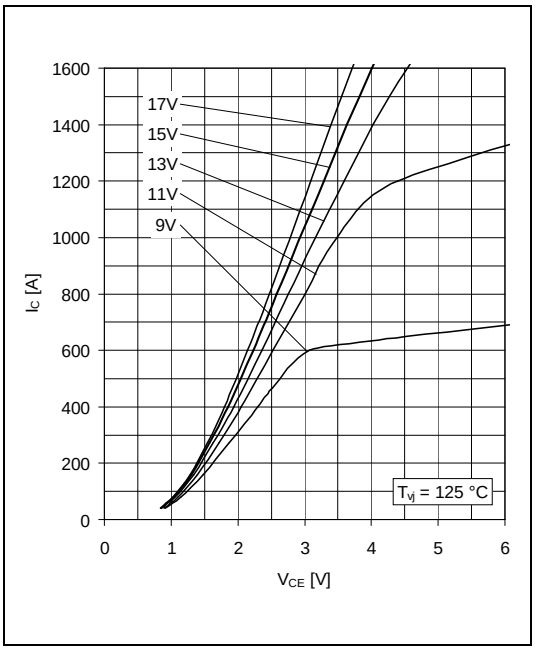

Fig. 4 Typical output characteristics, chip level

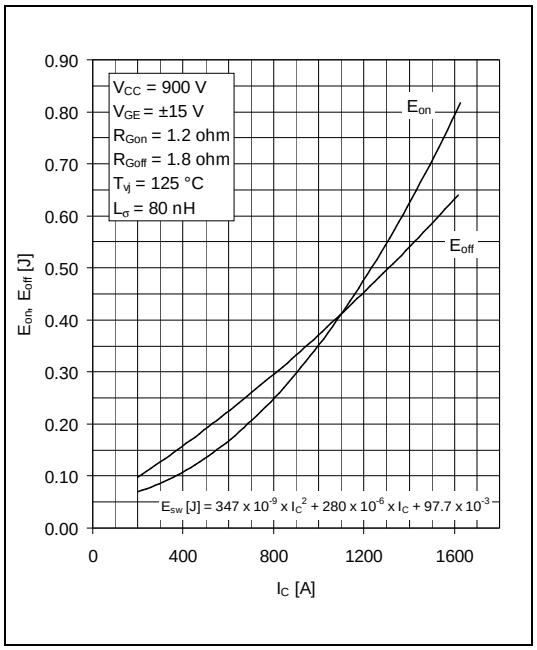

Fig. 5 Typical switching energies per pulse vs collector current

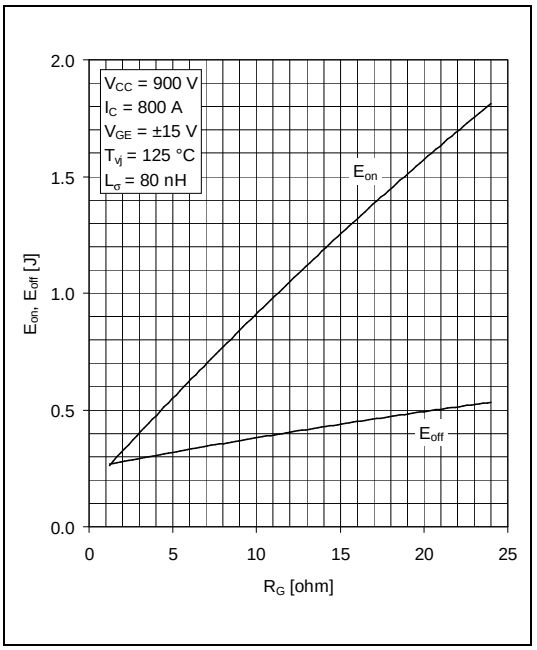

Fig. 6 Typical switching energies per pulse vs gate resistor

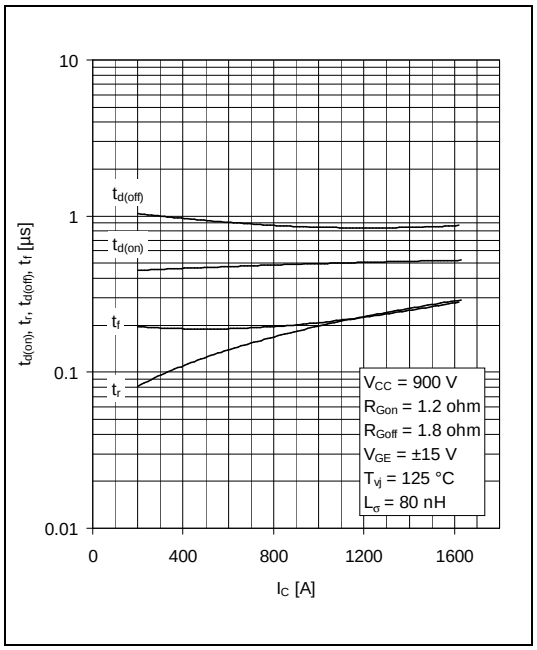

Fig. 7 Typical switching times vs collector current

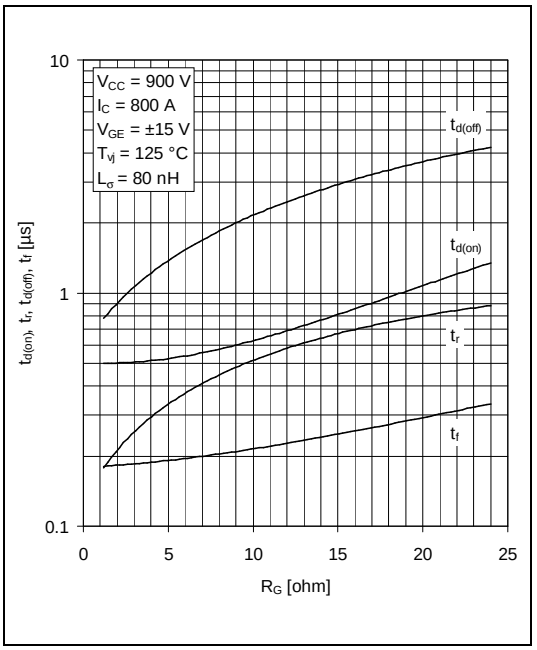

Fig. 8 Typical switching times vs gate resistor

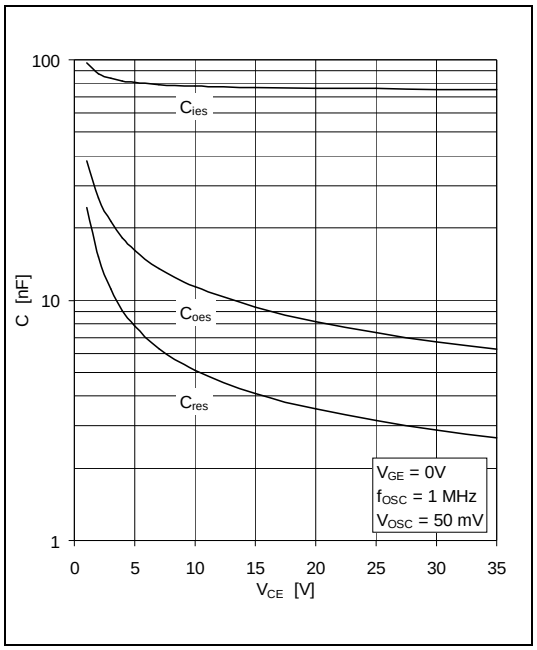

Fig. 9 Typical capacitances vs collector-emitter voltage

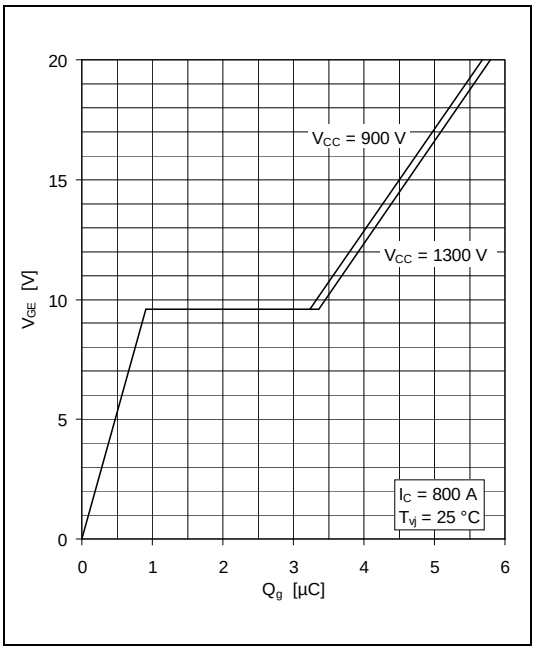

Fig. 10 Typical gate charge characteristics

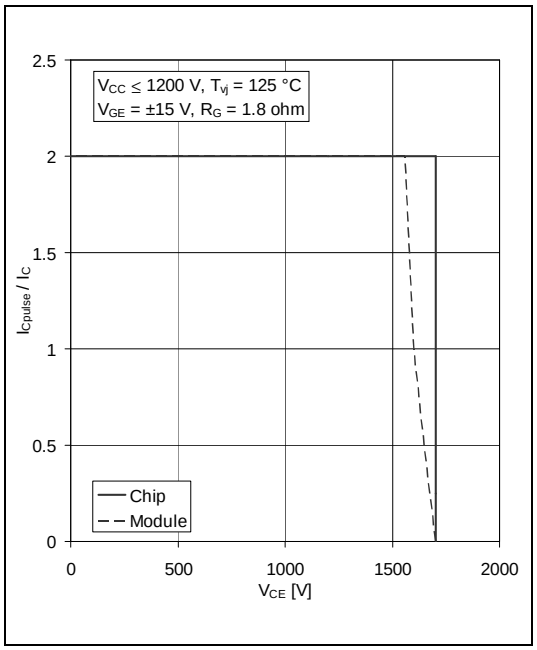

Fig. 11 Turn-off safe operating area (RBSOA)

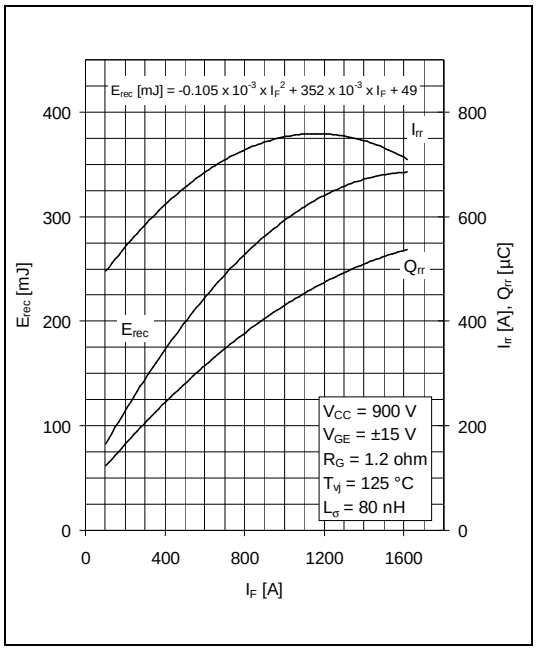

Fig. 12 Typical reverse recovery characteristics vs forward current

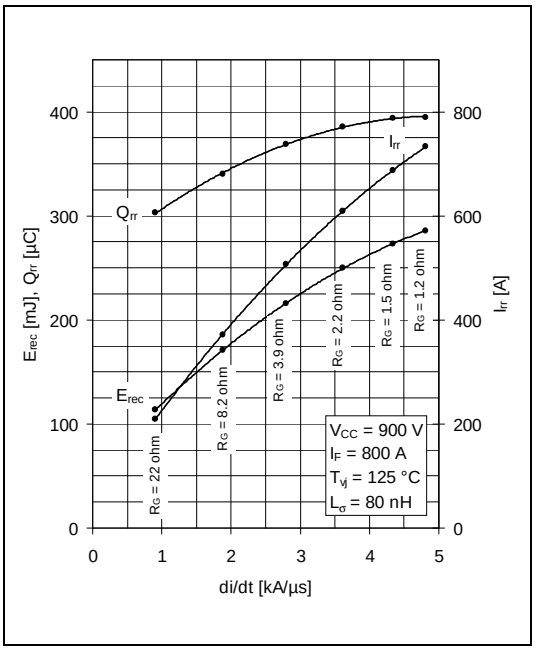

Fig. 13 Typical reverse recovery characteristics vs di/dt

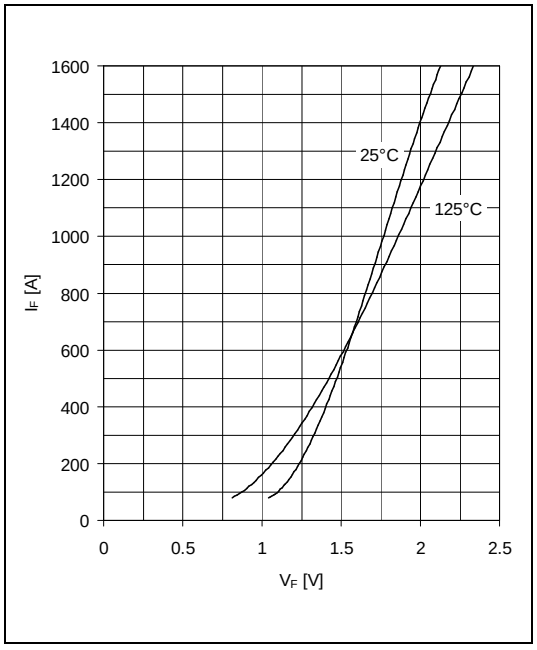

Fig. 14 Typical diode forward characteristics, chip level

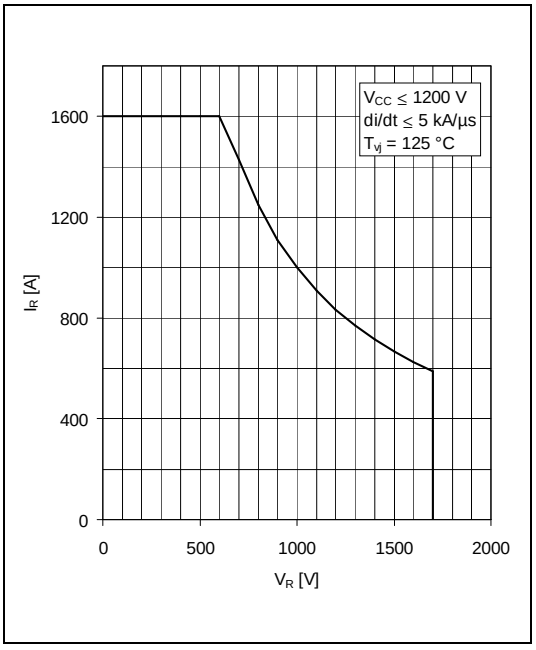

Fig. 15 Safe operating area diode (SOA)

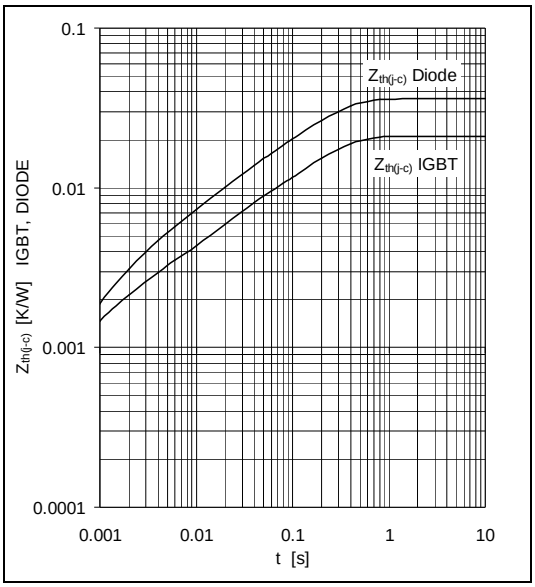

Fig. 16 Thermal impedance vs time

Analytical function for transient thermal impedance:

$$Z_{th\,(j\text{-}c)}(t) = \sum_{i=1}^{n} R_i\,(1 - e^{-t/t_i})$$

	i	1	2	3	4	
IGBT	R_i(K/kW)	15.2	3.6	1.49	0.74	
	τ_i(ms)	202	20.3	2.01	0.52	
DIODE	R_i(K/kW)	25.3	5.78	2.6	2.52	
	τ_i(ms)	210	29.6	7.01	1.49	

For detailed information refer to:

- 5SYA 2042-02 Failure rates of HiPak modules due to cosmic rays
- 5SYA 2043-01 Load – cycle capability of HiPaks
- 5SZK 9120-00 Specification of environmental class for HiPak (available upon request)

ABB Switzerland Ltd
Semiconductors
Fabrikstrasse 3
CH-5600 Lenzburg, Switzerland

Telephone +41 (0)58 586 1419
Fax +41 (0)58 586 1306
Email abbsem@ch.abb.com
Internet www.abb.com/semiconductors

Doc. No. 5SYA1590-00 Oct 06